Computing Models of Supernova Remnant Spectra in Galaxy M101 to Analyze Stellar Evolution

Mark DeMorra-Senior Research
Advisor: Dr. Joseph Howard

Table of Contents

Mark DeMorra
Advisor: Dr. Joe Howard
PHYS 499
5/13/08

COMPUTING MODELS OF SUPERNOVA REMNANT SPECTRA IN GALAXY M101 TO ANALYZE STELLAR EVOLUTION

ABSTRACT:

This research was undertaken to determine the physical and chemical characteristics of selected supernova remnants (SNR's) in the M101 galaxy and to investigate the physical constituents of these potential stellar structures. By the project's end, four supernova remnants in M101 were analyzed and modeled, with their chemical and physical components derived from the equations built into the CLOUDY computational program. The differences between the derived computational readings, from CLOUDY, and the actual observed line spectra measurements obtained from other researchers, for each model, were insignificant enough that it is felt it can be said, with much confidence, that the models derived are accurate interpretations of the true physical nature of these four supernova remnants. From these resultant computational models, the type of supernova remnant was determined from certain characteristics, including temperature, ionization parameter, filling factor, hydrogen density, and certain specific elemental abundances. The research was performed in the Spring 2008 semester at Salisbury University, and was overseen by Dr. Joseph Howard.

INTRODUCTION:

M101 is known more specifically as the Messier 101 galaxy, and is a spiral galaxy about 27 million light-years from Earth, located in the Ursa Major constellation, also known as the "Great Bear" constellation. It was discovered by Pierre Mechain in March of 1781, seen between the left hand of Bootes and the Great Bear's tail, and was subsequently included as one of the last entries in Charles Messier's catalogue of astronomical objects, hence its cataloged name (Messier 101). However, it was not originally considered an important discovery, as most Astrophysicists, at the time, were engrossed in the study of comets and their effects on galaxies and the universe, as a whole. Thus, it was quite some time before M101 was given the attention by researchers that it should have had from the beginning.

M101 has a diameter of approximately 170,000 light years, making it about twice the size of the Milky Way Galaxy. Recent work by Astrophysicists has narrowed down the estimated mass of M101 to between 100 and 1000 billion solar masses, up from previous estimates of about 16 billion. Because of this great mass, and the fact that it is a face-on galaxy, M101 is an ideal spiral galaxy for scientists to study not only extragalactic structure, but also exactly how galaxies and stars evolve. Thus, there has been much research and observational work published on M101 in the past fifty years.

Research in recent years, from the Chandra X-Ray Observatory in particular, indicates that it is highly probable that supernova remnants exist in M101, but general acceptance in the scientific community has yet to occur. However, new evidence of temperatures between one million and four million degrees Celsius, in the galaxy, could suggest the existence of a new class of midrange massive black holes and other instances of late stellar phenomenon, findings considered to be highly important in current studies of stellar evolution (Pinwheel Galaxy).

Stars in the late stages of stellar evolution can be studied thoroughly in a galaxy with the characteristics of M101. When a star exhausts its fuel supply via nuclear fusion, potentially after billions of years of doing such, its remnants can take on one of three forms: white dwarfs for smaller stars, neutron stars when a larger star's core collapses, or black holes for the most massive stellar objects. White dwarfs are the most common instance of late stellar phenomenon, a phenomenon that is the fate of approximately 90% to 95% of the universe's stars. Late in such a star's life, it becomes a super-massive, overly large, and very luminous red giant. The core, at this point, is made up mostly of Carbon, having been fused originally from Hydrogen and other less massive elements earlier in the star's life. However, Carbon, in most stars, can not be fused together to create more massive elements, due to an insufficient amount of heat and pressure created from electron degeneracy and gravitational forces. In effect, the Helium-burning outer shells of these stars will contract and pulsate until the outermost layers are ejected from their connection with the core, creating a supernova surrounded by what are called supernova remnants. The supernova that results, formerly the star's core, is the incredibly hot, very dense remnant now called a white dwarf. Particles are so tightly packed in a white dwarf their motions are severely restricted, creating a material called a degenerate electron gas. Here, electrons have a relatively uniform distribution around their nuclei, fixed in such a way they resemble a crystal lattice

However, white dwarfs only emerge in stars with a mass, at their time of death, of less than 1.4 solar masses, called the Chandrasekhar Limit. If a star has a dying mass of between 1.4 and 3 solar masses, it becomes a neutron star. Here, a similar path is followed, at first, to that of stars that eventually become white dwarfs, except that the stars, late in their life, actually reach a point where they can fuse Carbon to form more massive elements, unlike their white dwarf counterparts, before becoming supernovas that have radii greater than the Chandrasekhar Limit. When Carbon fusion occurs, the pressure due to electron degeneracy starts to be overcome by gravitational collapse, causing protons and electrons to forcefully combine together to form neutrons, in the star's core. The result is a quantum mechanical object that behaves like a highly dense gas of neutrons, with an incredibly small radius, sometimes only a few kilometers in length, and an incredibly large mass, up to three solar masses. This is the neutron star, composed entirely of neutrons, which can have a surface gravity approximately one trillion times that of earth and a density so great that one teaspoon of the crust could weigh up to five billion tons.

When a supernova, and thus a dying star, however, has a mass of greater than three solar masses, the Tolman-Oppenheimer-Volkoff Limit, an incredible physical phenomenon takes place. Here, gravitational pressure becomes so strong, compared to that of electron degeneracy, in the dying star's core, that it will cause the star to continually collapse until it reaches the Schwarzschild radius. Defined as $R_{schwarz}$=3M, where M is in solar masses, a star of mass M that becomes collapsed to a radius $R_{schwarz}$ will have its volume continually and rapidly decrease, and thus have its density continually and rapidly increase, until it reaches a point called a singularity, where the basic laws of Physics break down and an object is created that has both an infinite density and a volume of zero. Scientists call this object a black hole, named such due to the fact it cannot be directly detected by normal visual means, as the gravitational pull of a black hole is so strong that not even light can escape, the only object known that can do such. A black hole is an example of a physical vacuum, which uses the force of gravity to attract stars, other black holes, and sometimes even entire galaxies to its location. A black hole also creates a bend in space-time, making it impossible for one to witness an object passing through its event horizon, likened to a black hole's edge, and thus actually entering the black hole, itself (Zeilik).

The computer program CLOUDY, used in this research, was needed to model and analyze previously observed spectra of stellar phenomenon by scientists. The model program, CLOUDY, was created by Professor G.J. Farland of the University of Kentucky, Lexington to model stellar phenomenon and produce theoretical spectra based on a set of input physical and chemical parameters. Using information obtained about the region of M101 being studied, including its temperature, ionization parameter, radius, filling factor, hydrogen density, and various elemental abundances, CLOUDY performed a number of mathematical and physical calculations to obtain characteristic light intensity graphs that resulted from over 30 inputs the program allowed to be modified. Each model was then compared to the researched observational data until both closely matched each other, thus leading to the conclusion that the CLOUDY input parameters resembled the physical and chemical reality of the respective supernova remnant.

METHODS:

To investigate black holes and other late stellar phenomenon in a region of M101, it was first required that particular information be acquired about supernova remnants in the galaxy. This was performed online, where information about "supernova spectra" and "photo ionization models" were most desired. Other information, such as elements and their abundances in these same regions of M101, along with the region's temperature, density, and other physical characteristics, were also searched for. In particular, raw data of measured light intensity spectra graphs compiled from observations, in previous work, were the most important pieces to help in determining if certain area of M101 have objects that are in the late stages of stellar evolution. A report, published in the The Astrophysical Journal Supplemental Series in 1997 by David Matonick and Robert Fesen, entitled Optically Identified Supernova Remnants in the Nearby Spiral Galaxies NGC 5204, NGC 5585, NGC 6946, M81, and M101, was the source for the spectral line graphs used in the experiment. From it, light intensity spectra graphs measurements for eleven supernova remnants in M101 were published. This chart can be seen hereafter:

	SNR No.										
LINE	17	19	21	24	33	38	44	50	71	76	83
Hβ λ4861	100	100	100	100	100	N/A	100	100	100	100	100
[O III] λ4959	28	38	185	103	69	N/A	N/A	26	14	32	35
[O III] λ5007	127	173	532	276	194	N/A	35	188	26	75	177
[N I] λ5200	N/A	N/A	N/A	N/A	N/A	N/A	N/A	N/A	N/A	N/A	N/A
He I λ5876	N/A	N/A	N/A	N/A	N/A	N/A	N/A	N/A	N/A	N/A	N/A
[O I] λ6300	39	52	76	100	N/A	54	21	50	32	52	30
[O I] λ6364	N/A	33	21	49	N/A	N/A	7	N/A	9	20	11
[N II] λ6548	61	60	57	99	72	N/A	41	117	46	26	74
Hα λ6563	300	300	300	300	300	300	300	300	300	300	300
[N II] λ6583	163	192	186	208	215	N/A	N/A	358	127	78	180
[S II] λ6716	162	175	163	167	124	119	93	102	131	113	153
[S II] λ6731	110	116	107	151	89	88	65	139	96	72	74
SNR Parameters:											
sec z	1.23	1.15	1.15	1.33	1.54	1.25	1.18	1.12	1.18	1.28	1.09
E_{B-V}	0.45	0.55	0.59	0.60	0.56	0.00	0.51	0.35	0.35	0.04	0.42
$I(H\alpha)^b$	6.8 E-15	2.1 E-14	1.9 E-14	7.2 E-15	8.0 E-15	3.3 E-15	2.5 E-14	2.5 E-15	2.0 E-14	6.3 E-15	2.8 E-14

After initial estimates were made, the input models were then compared to the observational data, and the various physical parameters adjusted thereafter, until models were produced that closely matched the physical and chemical reality for each of the four supernova remnants.

The computer program CLOUDY was used to model and analyze this previously observed spectra. Part of the time spent on the project had to be directed towards learning the CLOUDY program and the various functions it can perform, so its abilities could be fully implemented into the project. One of the most important features CLOUDY comes equipped with is the "Optimize Lines" command. By inputting the values for certain specified spectral lines, as found in the chart above in this case, CLOUDY makes estimates of certain physical features, chosen for the program to vary by the user, to acquire a spectral result that matches what the user desires. This can only be done, however, when the elemental abundances are believed to be reasonably close to their actual physical values, as the "Optimize Lines" command does not have the ability to vary elemental abundances, but only the region's temperature, Hydrogen density, filling factor, ionization parameter, luminosity and radius. Once becoming more acquainted with the program, the particular sets of supernova remnant data to be used and modeled on the CLOUDY program had to be decided upon.

In CLOUDY, physical parameters are mathematically adjusted in many ways. When examining a CLOUDY input file, the user would notice the elemental abundances are given in negative numbers. These refer to the power of ten whose result gives the abundance of that individual element in the studied region. For example, for the elemental abundance of Oxygen, if it was listed on the CLOUDY input file as -1.5, the true abundance of Oxygen in the area being studied is $10^{-1.5}$ parts per million. The same idea applies to the Hydrogen density. The ionization parameter is a dimensionless ratio that represents the ratio of ionizing photons, in the studied region, to the total Hydrogen densities. The radius of the region can be measured in either light-years or linear parsecs, while the temperature, labeled "blackbody temperature" is in Kelvin. Luminosity, while important in studies of HII regions but not as much in supernova remnants, is measured in ergs per second while filling factor can be described as the percentage of how smoothly mass is distributed throughout the studied region. A region's filling factor can have a maximum value of one, meaning the mass in the region is distributed highly erratically and mostly clumped together in groups, while values more towards zero imply a model with less gathering of material and a more evenly distributed dissemination of material.

After CLOUDY gave satisfactory results for four studied supernova remnants in M101, the resultant models were originally going to be analyzed in such a way as to predict the possibility of the existence of late stellar phenomenon, along with their physical characteristics. Certain observations, in particular associated with black holes, such as ultraluminous X-rays, gamma ray bursts, spectral line emission, and radio emission, were going to be searched for, and included if they lead to any specific conclusions. The same observations, including radio pulses and X-ray bursts associated with oscillation, were going to be researched and applied, yet again, for neutron stars. However, during the modeling stages, a lack of progress halfway through the timeline led to an investigation of why the models were not giving the desired results. Studying the various types of supernova remnants and making comparisons of characteristic trends to those in Matonick's report ended up being a key to having the CLOUDY models match the supernova remnant spectra, and, thus, nullified any necessary extra research needed to determine the type of supernova associated with each model.

RESEARCH:

It was decided, after examining the measurements for each supernova remnant in Matonick and Fesen's report, that SNR 24 would be the first remnant attempted to be modeled. It wasn't long after attempts began that problems arose, however. With a starting temperature of about 50,000 K, an ionization parameter of about -1.8, and a Helium abundance of about 10^-2, the elemental abundances could be modeled in such a way that the O III lines had small margins of error, but the S II and N II lines were severely out of proportion. Also disturbing was the fact that the O I 6300 line, on the CLOUDY model, was only about 1% what it needed to be, compared with the prior obtained line intensities in the chart. The 6300 line is especially critical, though, because it is vital in determining the age of the supernova remnant. Having it come out, on CLOUDY, to be only 1% of its expected value was serious cause for reevaluation.

This is the point where examination of the various types of supernova remnants was undertaken. Supernova remnant spectra, and thus supernova themselves, are broken into four classes: Ia, Ib, Ic, and II. Type I's are distinguished from type II's by the Hydrogen absorption lines the spectrum. Whereas type II supernova remnants have Hydrogen absorption lines in their spectrum, type I's do not. Furthermore, the class of type I supernovas are distinguishable from other spectral features. In particular, type Ib's are unique in that they have strong Helium I lines, while Ia's and Ic's have none. However type Ia's and type Ic's are distinguishable in that Ia's tend to have spectra very blue-shifted, while type Ic's have spectra that are very red-shifted. A table of some of these distinguishing characteristics, along with other generalized information about the spectra of the four supernova remnant types, can be found in the next table:

Characteristic	**Type Ia**	**Type Ib**	**Type Ic**	**Type II**
H absorption lines in spectrum?	No	No	No	Yes
Helium lines?	No	Yes	No	Yes
Peaks	4000-4500 Å	6000 Å 7900 Å	5500 Å 6500 Å 8100 Å 8300 Å	4200 Å 6700 Å
Troughs	3800 Å 6100 Å 8100 Å	4000 Å 5900 Å 6100 Å 8000 Å	6800 Å 7600 Å 8200 Å	4800 Å 6600 Å
Range	3000 Å-9000 Å	4000 Å-8000 Å	3800 Å-8800 Å	4000 Å-9000 Å

With these characteristics in mind, the spectra chart from Matonick's report was examined, and it was theorized the supernova remnants being worked with were type Ia. Characteristic of type Ia supernova remnants are the absence of Helium lines and a blue-shifted spectra graph. Thereafter, in the CLOUDY input files, all of the Helium was taken out of the models, leaving just Hydrogen and trace amounts of the other elements. However, this led to a conclusion that originally went against some of the original intentions of the project. Type Ia supernova remnants are characterized with stellar deaths involved with astrophysical binary systems. These supernova remnants are thought to be created by the collapse of a mass-enveloping white dwarf in a semi-detached binary star system. The result of such an interaction is a super-massive explosion that expels all the mass from the white dwarf system, called Carbon deflagration, leaving behind a massive cloud of dust that disintegrates and disperses throughout the region. As Type Ia supernova remnants were determined to be the most likely candidates for the supernova remnants being studied, no black holes or neutron stars could be hypothesized to result from the models examined in Matonick's report.

Taking the Helium out of the models led to an improved margin of error for O I, but it was still only about one-third of the value it needed to be. After some experimental manipulation, along with usage of CLOUDY's "Optimize Lines" command, it was decided that increasing the temperature substantially might help the results the program produced. After increasing the temperature of the system by a factor of about six, the results, again, substantially improved, and, for the most part, the resultant models from CLOUDY had Oxygen lines that nearly identically matched those in the original spectra chart provided by Matonick and Fesen.

Even though the Oxygen lines matched up well, other important spectral lines, those for Nitrogen II and Sulfur II, were not matching up. It was at this point, however, that the numerical ratios between the S 6716 and S 6731 lines and the N 6548 and N 6584 were observed to match up very well with another supernova remnant in Matonick's report, M101's SNR 33. Dropping the elemental abundance parameters for Oxygen, Sulfur, and Nitrogen, corresponding to the smaller spectral values for the supernova remnant, CLOUDY gave a result that nearly perfectly matched the previously determined spectral lines for SNR 33. A chart of the information on this model is included below:

SNR 33					
SPECTRAL LINE	**λ: WAVELENGTH (nm)**	**OBSERVED SPECTRAL VALUES**	**CLOUDY OBTAINED SPECTRAL VALUES**	**+/-**	**% ERROR**
O III	4959	69	68	-1	1.45%
O III	5007	194	197	+3	1.55%
O I	6300	N/A	N/A	N/A	N/A
N II	6548	72	73	+1	1.39%
N II	6583 (6584)	215	215	0	0%
S II	6716	124	124	0	0%
S II	6731	89	89	0	0%
OVERALL PERCENT ERROR:		.73%			

The input file that describes the physical parameters of SNR 33 can be found in the appendices, along with the input files and physical parameters for all the supernova remnants studied in this project. The Overall Percent Error calculation was derived by summing the percent errors for each spectral line and dividing the result by the number of spectral lines used. Oxygen 6300 was not available for SNR 33, but it was concluded that with the great accuracy the other modeled spectral lines came to have, the result CLOUDY would have provided for an O 6300 spectral line would have been just as accurate.

Using what was learned from this success, other supernova remnants included in Matonick's report were examined to see if the ratios between the Oxygen lines, Nitrogen lines, and Sulfur lines were comparable to that of SNR 33 or SNR 24. SNR 21 in M101 was found to also have very similar elemental ratios to that of SNR 33, and so the elemental abundances were tooled with to fit its particular characteristics. The CLOUDY-obtained results, once again, came within small margins of error with those presented in the original report. The results for SNR 21 follow:

SNR 21					
SPECTRAL LINE	**λ: WAVELENGTH (nm)**	**OBSERVED SPECTRAL VALUES**	**CLOUDY OBTAINED SPECTRAL VALUES**	**+/-**	**% ERROR**
O III	4959	185	185	0	0%
O III	5007	532	534	+2	.38%
O I	6300	76	76	0	0%
N II	6548	57	61	+4	7.02%
N II	6583 (6584)	186	180	-6	3.23%
S II	6716	163	157	-6	3.68%
S II	6731	107	113	+6	5.61%
OVERALL PERCENT ERROR:		2.85%			

Another surprising success, this only backed up the theory that the supernova remnants being studied in the research and in Matonick's report were, for the great majority, type Ia supernova remnants.

It was also noted that the same ratios for the Oxygen, Sulfur, and Nitrogen lines seemed to exist for SNR 76. However, upon manipulating the CLOUDY parameters to values that were predicted to yield the supernova remnant's spectral results, the abundances for S 6731 and N 6583 were much high than what they should have been compared to S 6716 and N 6548, respectively. After adjusting various CLOUDY parameters, attention was turned to one that had, to this point, remained basically unchanged. It was found, after some experimentation, that doubling the ionization parameter for these supernova remnants greatly narrowed the margin between the two ratios for Sulfur and Nitrogen. When this happened, the results for SNR 76 lost most of the error they previously had. The result of this work can be found below:

SNR 76					
SPECTRAL LINE	**λ: WAVELENGTH (nm)**	**OBSERVED SPECTRAL VALUES**	**CLOUDY OBTAINED SPECTRAL VALUES**	**+/-**	**% ERROR**
O III	4959	32	31	-1	3.13%
O III	5007	75	88	+13	17.3%
O I	6300	52	52	0	0%
N II	6548	26	26	0	0%
N II	6583 (6584)	78	78	0	0%
S II	6716	113	103	-10	8.85%
S II	6731	72	72	0	0%
OVERALL PERCENT ERROR:		4.18%			

While at this point, the fact that three supernova remnants were modeled, when it was originally thought only one would be completed, made it seem this research project had become a monumental success, it still was disappointing that the spectra for the originally studied supernova remnant, SNR 24, could not be derived in CLOUDY. As a final attempt to derive SNR 24's spectral lines, also using the other various realizations made during the course of the research up to this point, great manipulation was made to the Hydrogen density readings, which had also gone unchanged up to this point. The value of this parameter was doubled, along with a marked increase in the ionization parameter. Three months after SNR 24 was originally attempted to be modeled, with three other supernova remnants falling into place in the interim, CLOUDY finally produced a spectra with a small enough margin of error that it was concluded the physical parameters for SNR 24 were found. The long-awaited results came out to be:

SNR 24					
SPECTRAL LINE	**λ: WAVELENGTH (nm)**	**OBSERVED SPECTRAL VALUES**	**CLOUDY OBTAINED SPECTRAL VALUES**	**+/-**	**% ERROR**
O III	4959	103	99	-4	3.88%
O III	5007	276	286	+10	3.62%
O I	6300	100	100	0	0%
N II	6548	99	94	-5	5.05%
N II	6583 (6584)	208	277	+69	33.17%
S II	6716	167	167	0	0
S II	6731	151	151	0	0
OVERALL PERCENT ERROR:		6.53%			

CONCLUSIONS:

If more time was allotted to complete this project, there is no doubt that the physical parameters for these four supernova remnants, derived from CLOUDY, would result in even smaller margin of errors that what have already come about. Also, with the incredible focus that was put on the O 6300 spectral line during the course of this project, future research could include the relationship between this particular spectral reading and how it affects the type of supernova remnants being studied.

With the determination, by first observing general trends for supernova remnant types and confirming such through modeling the systems via CLOUDY, that the four supernova remnants studied were all Type Ia, the phenomenon associated with a binary system involving a white dwarf that gains so much mass from its binary partner that it collapses upon itself and disintegrates into a super-massive gaseous system, this leads to the conclusion that the majority of these supernova remnants will not lead to the stellar phenomenon of black holes or neutron stars, as originally hoped. However, the satisfaction of modeling three more supernova remnants than initially expected is enough to make up for this loss. It is the fervent hope that researchers who undertake similar projects in the future, modeling supernova remnants using the CLOUDY program, will be able to make the determination that their particular regions will be conducive towards the evolution of black holes or white dwarfs, two highly sought after and fascinating examples of unique Astrophysical phenomenon.

REFERENCES:

Matonick, David M. and Robert A. Fesen. "Optically Identified Supernova Remnants in the Nearby Spiral Galaxies NGC 5204, NGC 5585, NGC 6946, M81, and M101." September 1997: The Astrophysical Journal Supplemental Series, 112: 49-107.

"Messier 101." 30 Aug. 2007. 10 Dec. 2007. <http://www.seds.org/messier/m/m101. html>.

"Pinwheel Galaxy." 25 Nov. 2007. 5 Dec. 2007. <http://en.wikipedia.org/wiki/Messier_1 01>.

Zeilik, Michael and Stephen A. Gregory. Introductory Astronomy & Astrophysics. 4th ed. Brooks/Cole, 1998. 332-347.

COMPUTING MODELS OF SUPERNOVA REMNANT SPECTRA IN GALAXY M101 TO ANALYZE STELLAR EVOLUTION

Mark DeMorra-Senior Research
Advisor: Dr. Joseph Howard

WHAT IS M101?

- M101-Messier 101 Galaxy
  - Catalog Name
- Discovered by Pierre Mechain in 1781
- Approx. 27 million light years from Earth
- Ursa Major (Great Bear) Constellation
- Spiral Galaxy about 170,000 light years in diameter
  - Twice the size of Milky Way
- Mass between 100 and 1000 billions suns

OTHER INTERESTING INFO

- When originally discovered, not considered important
  - Scientists focusing on comets at the time
  - Messier Catalog a supposed list of "unimportant stellar objects"...
- M101 a face-on galaxy
  - Able to see more detail
  - Easier to study its extragalactic structure
- Studied extensively by Chandra X-Ray Observatory
  - Recent research indicates supernova remnants in M101

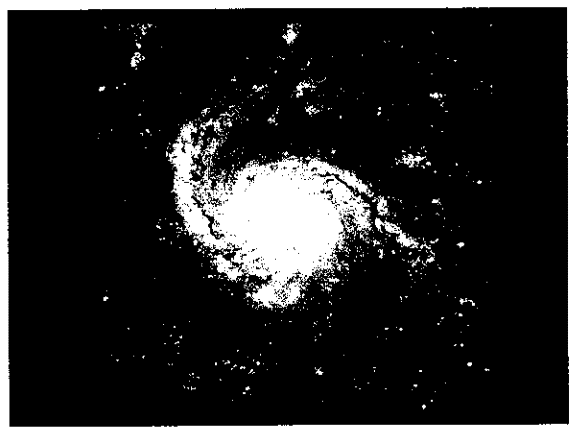

WHAT THE HECK ARE SUPERNOVA REMNANTS?

- Supernova remnants are products (usually gaseous) of objects who have entered last stages of stellar evolution (stellar corpses)
  - White Dwarfs
  - Black Holes
  - Neutron Stars
- Aftereffect of certain stars exhausting fuel supply via nuclear fusion
  - Takes billions of years
- Type of supernova remnant dependent on star's mass upon death (what was formerly star's core)
  - Less than 1.4 Solar masses-White Dwarf
  - Between 1.4 and 3 Solar Masses-Neutron Star
  - Greater than 3 Solar Masses-Black hole

A TREATISE ON... DEATH

- White Dwarfs
  - Last stage for stars with cores of mass at "death" less than Chandrasekhar Limit (1.4 solar masses)
  - Fate of approximately 90% of stars in the universe
  - Core behaves like a quantum mechanical degenerate electron gas
  - Incredibly hot and very dense

MORE DEATH!

- Neutron Stars
  - Incredibly dense objects composed mostly of neutrons
  - Final stage of midsized stars
    - Mass of core at "death" greater than Chandrasekhar Limit (1.4 solar masses) but less than Tolman-Oppenheimer Volkoff Limit (3 solar masses)
  - Heavy liquid core with solid crust
  - Teaspoon amount-weigh 5 billion tons

AND EVEN MORE DEATH!

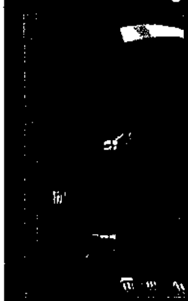

- Black Holes
  - Final stage for stars with cores, at death, greater than the Tolman-Oppenheimer Volkoff Limit (3 solar masses)
  - Occurs when gravity causes collapse below Schwarzschild radius ($R_{schwarz}$~3M)
  - Creates gravitational field so strong not even light can escape from it
  - Cannot witness objects entering black hole as gravity bends space-time

CLOUDY

- Computer program used to model and analyze astrophysical systems
- CLOUDY has built-in equations that are derived from 30+ input values
  - Elemental Abundances (parts per million)
    - Oxygen
    - Sulfur
    - Nitrogen
  - Temperature (K)
  - Ionization Parameter (% of atoms getting ionized)
  - Hydrogen Density (Power of 10)
  - Filling Factor ("clumpiness" percentage)

OPTIMIZE LINES

- Used when elemental abundances are believed to be close to their physical reality
- User chooses physical parameters for program to vary over course of multiple calculation run-throughs
  - CLOUDY can vary all physical attributes except elemental abundances

WHERE TO START?

- Locate supernova remnant spectral graphs/charts
  - Optically Identified Supernova Remnants in the Nearby Spiral Galaxies NGC 5204, NGC 5585, NGC 6946, M81, and M101
    - David Matonick and Robert Fesen
    - Published in The Astrophysical Journal Supplemental Series-September 1997

SPECTRAL CHART

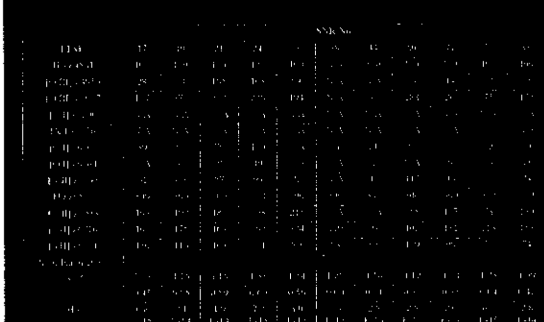

AND… WE'RE OFF

- Decided to start with SNR 24
  - Focused on:
    - O 4959
    - O 5007
    - O 6300
    - N 6548
    - N 6583
    - S 6716
    - S 6731
- Focused on same spectral lines with all SNR's studied (ones most important in galactic "death")

THE ORIGINAL INPUT FILE

```
Title ORIGINAL INPUT
c luminosity 39.2
hden 1.821606
radius 15 linear parsecs
blackbody temp = 51250
filling factor = .1197
ionization parameter = -1.849297
c
abundances he=-20.0 li=-10.260 be=-20.00 b=-10.051
continue c=-3.5229 n=-5.015 o=-4.036 f=-20.00 ne=-4.4200
continue na=-6.5229 mg=-5.5229 al=-6.699 si=-5.3979 p=-6.7959
continue s=-5.55 cl=-7.00 ar=-6.130 k=-7.9586 ca=-7.699
continue sc=-20.00 ti=-9.2366 v=-10.00 cr=-8.00 mn=-7.00
continue fe=-6.0229 co=-6.00 ni=-7.00 cu=-8.8239 zn=-7.699
c
c
c optimize lines
c O  3 5007 intensity=75 error=1.0
c O  3 4959 intensity=32 error=1.0
c O  1 6300 intensity=52 error=1.0
c S II 6731 intensity=72 error=1.0
c S II 6716 intensity=113,error=1.0
c N  2 6584 intensity=78 error=1.0
c N  2 6548 intensity=26 error=1.0
c end of lines
c TOTL 3727 intensity=218 error=2.0
c TOTL 4363 intensity=2.3 error=0.5
c S  3 9069 intensity=25.0 error=1.0
c S  3 9532 intensity=65.0 error=1.0
c Ar 3 7135 intensity=9.2 error=1.0
c Ne 3 3869 intensity=24.6 error=2.0
```

NOT A GOOD START

- Started with:
  - A temperature of about 50000K
  - Ionization parameter of about -1.8
  - Filling factor of .1
  - Hden of about 1.8
- O 4959 and O 5007 got close, but O 6300 was off
  - Bad News-O 6300 vital in determining spectral age
  - Only about 1% of what it should've been (100)

LET'S TRY THIS:

- Examined different types of SNR's

- Theorized SNR 24 was Type Ia due to lack of Helium and the locations of spectra peaks

TYPE Ia SNR's

- Can be determined by lack of Helium lines on spectral graph
- Blue-shifted spectra
- Associated with star deaths involving Astrophysical binary systems
  - White Dwarf accretes (takes in) mass from another nearby stellar object
  - Results in super-massive explosion that disintegrates the system and leaves behind a dense dispersal of dust
    - Called Carbon deflagration

GETTING THERE…

- Removed all the Helium from SNR 24 model
- O6300 lines improved, but still only about 1/3 of what needed to be.
- From past work with CLOUDY, upping the temperature increased Oxygen readouts
  - Temperature upped to about 300,000K (600%) radically improved Oxygen results
  - Sulfur and Nitrogen lines still with large margins of error

RATIOS

- Ratios of S 6716/S 6731 and N 6548/N 6583 looked at
  - N 6548 higher than what needed to be, compared to N 6583
  - S 6731 higher than what needed to be, compared to S 6716
- Could not manage to correct errors through changing elemental abundances alone

A RADICAL MOVE

- Examining the S, O, and N ratios for SNR 33, it seemed they were much more in tune to the ratios CLOUDY was providing for SNR 24, at the time
- Elemental abundances were decreased to match the lower spectral numbers for SNR 33, compared to SNR 24...

SUCCESS!!!!!!!!!

WOOHOO! HALLEJUAH!

SUMMARY OF SNR 33

- Percent error calculated from summing percent errors and dividing by the number of spectral lines examined
- O 6300 not included with this SNR, but with accuracy of other spectral lines, it is felt O 6300 would have turned out just as accurate
- Helped to confirm that theory that SNR 33 and SNR 24 were both Type Ia SNR's

INPUT FILE FOR SNR 33

```
Title SNR33 in M101
c luminosity 38.2
hden 1.871406
radius 15 linear parsecs
blackbody temp = 284443
filling factor = .1
ionization parameter = -2.143257
c
abundances he=-20.0 li=-10.268 be=-20.00 b=-10.051
continue c=-3.5229 n=-4.448 o=-3.066 f=-20.00 ne=-4.6200
continue na=-6.4779 mg=-5.5729 al=-6.495 si=-5.3979 p=-6.7959
continue s=-4.967 cl=-7.00 ar=-6.132 k=-7.9586 ca=-7.693
continue sc=-20.00 ti=-9.2366 v=-10.00 cr=-8.00 mn=-7.00
continue fe=-5.0229 co=-6.00 ni=-7.00 cu=-8.5229 zn=-7.495
c
c
c optimize lines
c O 3 5007 intensity=196 error=1.0
c O 3 4959 intensity=65 error=1.0
c S II 6731 intensity=83 error=0.5
c S II 6716 intensity=134 error=0.5
c N 2 6584 intensity=215 error=0.5
c N 2 6548 intensity=72 error=0.5
c end of lines
c TOTL 3727 intensity=218 error=2.0
c TOTL 4363 intensity=2.3 error=0.5
c S 3 9069 intensity=56.0 error=1.0
c S 3 9532 intensity=68.0 error=1.0
c Ar 3 7135 intensity=9.2 error=1.0
c Ne 3 3869 intensity=24.6 error=3.0
```

ARE OTHER SNR'S IN TUNE?

- Examined other SNR's in Matonick's report to see if they had the same O, N, and S ratios as SNR 33.
  - Would allow, theoretically, only the elemental abundances to be changed to achieve the needed spectral results
- SNR 21 noted as having similar O, N, and S ratios as SNR 33...

LIGHTNING STRIKES TWICE!

- Even more solid proof that the SNR's being worked with were Type Ia's

INPUT FILE FOR SNR 21

```
Title SNR21 in M101
c luminosity 39.2
hden 1.021606
radius 18 linear parsecs
blackbody temp = 184442
filling factor = .1
ionization parameter = -2.843287
c
abundances he=-20.0 li=-10.268 be=-20.00 b=-10.051
continue c=-3.6229 n=-4.815 o=-3.444 f=-20.00 ne=-4.6200
continue na=-6.6229 mg=-5.5229 al=-6.699 si=-5.3979 p=-6.7959
continue s=-5.05 cl=-7.00 ar=-6.130 k=-7.9586 ca=-7.699
continue sc=-20.00 ti=-9.2366 v=-10.00 cr=-8.00 mn=-7.00
continue fe=-5.0229 co=-6.00 ni=-7.00 cu=-8.6239 zn=-7.699
c
c
c optimize lines
c O  3 5007 intensity=832 error=1.0
c O  3 4959 intensity=185 error=1.0
c O  1 6300 intensity=76 error=1.0
c S II 6731 intensity=107 error=0.5
c S II 6716 intensity=168 error=0.5
c N  2 6584 intensity=186 error=0.5
c N  2 6548 intensity=57 error=0.5
c end of lines
c TOTL 3727 intensity=218 error=1.0
c TOTL 4363 intensity=2.3 error=0.5
c S  3 9069 intensity=26.0 error=1.0
c S  3 9532 intensity=65.0 error=1.0
c Ar 3 7136 intensity=9.2 error=1.0
c Ne 3 3869 intensity=24.6 error=2.0
```

GO FOR THREE IN A ROW?

- SNR 76 was noted to have similar O, N, and S ratios as SNR 21 and SNR 33
- Felt assured the SNR's being dealt with in M101 were Type Ia's, thus Helium was no longer to be a factor in CLOUDY calculations
- O 6300 was smaller, compared to O 4959 and O 5007, implying a lower temperature as well...

NO DICE

- CLOUDY returned models, after adjusting temperature and elemental abundances, with accurate enough Oxygen spectral readings all around.
- However, Nitrogen and Sulfur ratios severely off, similar to that for SNR 24.
- Attention turned to adjusting a previously untouched physical constituent: ionization parameter
  - Running some practice models led to idea that ion. param. needed to be increased for SNR 76...

WHAM BAM SLAM!

INPUT FILE FOR SNR 76

```
Title SNR76 in M101
c luminosity 39.2
hden 1.021606
radius 18 linear parsecs
blackbody temp = 204440
filling factor = .1
ionization parameter = -3.35287
c
abundances he=-20.0 li=-10.268 be=-20.00 b=-10.051
continue c=-3.6229 n=-5.015 o=-4.035 f=-20.00 ne=-4.6200
continue na=-6.6229 mg=-5.5229 al=-6.699 si=-5.3979 p=-6.7959
continue s=-5.55 cl=-7.00 ar=-6.130 k=-7.9586 ca=-7.699
continue sc=-20.00 ti=-9.2366 v=-10.00 cr=-8.00 mn=-7.00
continue fe=-5.0229 co=-6.00 ni=-7.00 cu=-8.6239 zn=-7.699
c
c
c optimize lines
c O  3 5007 intensity=75 error=1.0
c O  3 4959 intensity=32 error=1.0
c O  1 6300 intensity=52 error=1.0
c S II 6731 intensity=72 error=1.0
c S II 6716 intensity=113 error=1.0
c N  2 6584 intensity=75 error=1.0
c N  2 6548 intensity=24 error=1.0
c end of lines
c TOTL 3727 intensity=218 error=2.0
c TOTL 4363 intensity=2.3 error=0.5
c S  3 9069 intensity=26.0 error=1.0
c S  3 9532 intensity=65.0 error=1.0
c Ar 3 7136 intensity=9.2 error=1.0
c Ne 3 3869 intensity=24.6 error=2.0
```

AT THIS POINT

- While satisfied in that three SNR's were modeled in about a four month time frame, still some disappointment in that SNR 24 could not be modeled by CLOUDY
  - Applied knowledge attained from modeling other remnants, but results still did not improve enough
- Last ditch effort- Alter another previously untouched physical parameter: Hydrogen density
  - Doubling Hden altered abundances, making this SNR about 98% Hydrogen...

FOUR FOR FOUR, FOUR MONTHS LATER

GRAND SLAM!

INPUT FILE FOR SNR 24

```
Title SNR24 in M101
c luminosity 35.2
hden 3.941606
radius 15 linear parsecs
blackbody temp = 304442
filling factor = .1
ionization parameter = -3.923287
c
abundances he=-20.0 li=-10.268 be=-20.00 b=-10.051
continue c=-3.5229 n=-4.451 o=-3.685 f=-20.00 ne=-4.6209
continue na=-6.5229 mg=-5.5229 al=-6.699 si=-5.3979 p=-6.7959
continue s=-4.828 cl=-7.00 ar=-6.130 k=-7.9586 ca=-7.699
continue sc=-20.00 ti=-9.2366 v=-10.00 cr= 6.00 mn=-7.00
continue fe=-5.0229 co=-6.00 ni=-7.00 cu=-8.5239 zn=-7.699
c
c
c optimize lines
c O  3 5007 intensity=276 error=2.0
c O  3 4959 intensity=103 error=2.0
c O  1 6300 intensity=100 error=2.0
c S II 6731 intensity=151 error=1.0
c S II 6716 intensity=167 error=1.0
c N  2 6584 intensity=208 error=1.0
c N  2 6548 intensity=99 error=1.0
c end of lines
c TOTL 3727 intensity=218 error=2.0
c TOTL 4363 intensity=2.3 error=0.5
c S  3 9069 intensity=25.0 error=1.0
c S  3 9532 intensity=65.0 error=1.0
c Ar 3 7135 intensity=9.2 error=1.0
c Ne 3 3869 intensity=24.6 error=2.0
```

WHERE IS THIS STUFF?

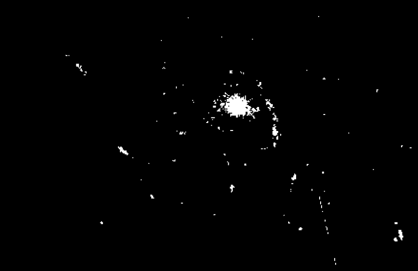

SNR 21

CONCLUSIONS

- Monumental Success
  - 3 more SNR's modeled than originally intended
  - Each model within accepted 10% error range
  - 3 of 4 models within rare 5% error range!
  - Determined type and final stellar evolution stage of SNR's (disintegration via Carbon deflagration)
- Elemental abundances (S, N, O) between four SNR's similar in magnitudes
  - Main differences between SNR's occurred in temperature, ionization parameter, and Hden
  - Implies similar chemical makeup throughout M101?

FUTURE RESEARCH?

- Do O 6300 (factor in age of SNR) spectral readings have a correlation with type of SNR being studied?
  - Factor in type of supernova (black hole, neutron star) that will be produced?
- Do other physical parameters featured in CLOUDY exhibit similar correlations?
- Via similar research means as undertaken here, is there spectral evidence of existence of black holes or neutron stars in M101?

ABSTRACT:

This research was undertaken to determine the physical and chemical characteristics of selected supernova remnants (SNR's) in the M101 galaxy and to investigate the physical constituents of these potential stellar structures. By the project's end, four supernova remnants in M101 were analyzed and modeled, with their chemical and physical components derived from the equations built into the CLOUDY computational program. The differences between the derived computational readings, from CLOUDY, and the actual observed line spectra measurements obtained from other researchers, for each model, were insignificant enough that it is felt it can be said, with much confidence, that the models derived are accurate interpretations of the true physical nature of these four supernova remnants. From these resultant computational models, the type of supernova remnant was determined from certain characteristics, including temperature, ionization parameter, filling factor, hydrogen density, and certain specific elemental abundances. The research was performed in the Spring 2008 semester at Salisbury University, and was overseen by Dr. Joseph Howard.

- Dr. Joe-The expert on BIRTH...
- Dr. Welsh-UNIX code
- Hubble Space Telescope for all the pretty pictures
- Dr. Ferland-CLOUDY is great!
- Students and Staff of Physics and Honors Departments for their support

Salisbury University

COMPUTING MODELS OF SUPERNOVA REMNANT SPECTRA IN GALAXY M101 TO ANALYZE STELLAR EVOLUTION

Author: Mark DeMorra Advisor: Dr. Joseph Howard

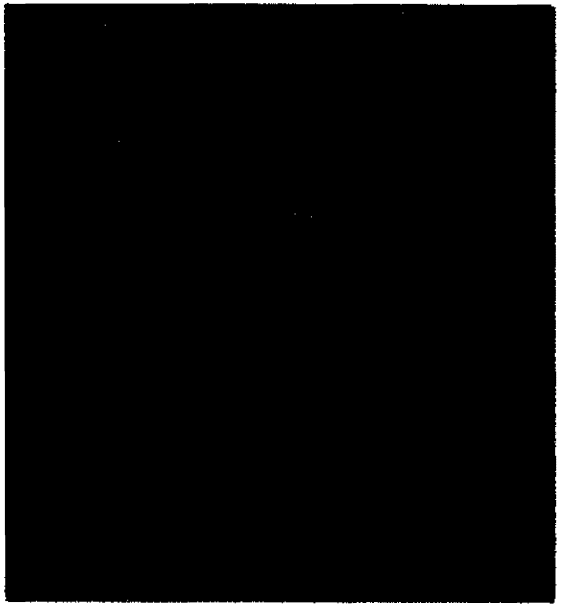

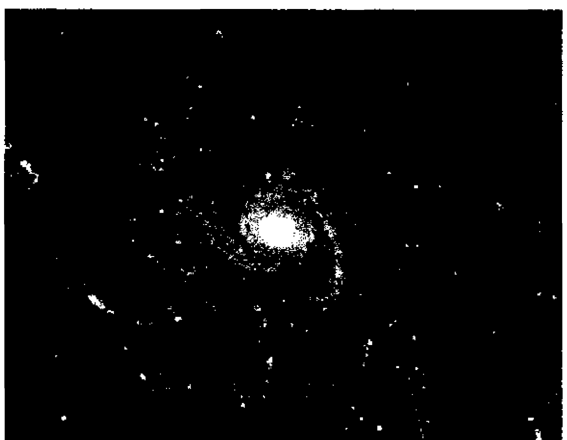

SNR 21

SPECTRAL LINE	λ: WAVELENGTH (nm)	OBSERVED SPECTRAL VALUES	CLOUDY OBTAINED SPECTRAL VALUES	+/-	% ERROR
O III	4959	185	185	0	0%
O III	5007	532	534	+2	.38%
O I	6300	76	76	0	0%
N II	6548	57	61	+4	7.02%
N II	6583 (6584)	186	180	-6	3.23%
S II	6716	163	157	-6	3.68%
S II	6731	107	113	+6	5.61%
OVERALL PERCENT ERROR:			2.85%		

SNR 24

SPECTRAL LINE	λ: WAVELENGTH (nm)	OBSERVED SPECTRAL VALUES	CLOUDY OBTAINED SPECTRAL VALUES	+/-	% ERROR
O III	4959	103	99	-4	3.88%
O III	5007	276	286	+10	3.62%
O I	6300	100	100	0	0%
N II	6548	99	94	-5	5.05%
N II	6583 (6584)	208	277	+69	33.17%
S II	6716	167	167	0	0
S II	6731	151	151	0	0
OVERALL PERCENT ERROR:			6.53%		

SNR 33

SPECTRAL LINE	λ: WAVELENGTH (nm)	OBSERVED SPECTRAL VALUES	CLOUDY OBTAINED SPECTRAL VALUES	+/-	% ERROR
O III	4959	69	68	-1	1.45%
O III	5007	194	197	+3	1.55%
O I	6300	N/A	N/A	N/A	N/A
N II	6548	72	73	+1	1.39%
N II	6583 (6584)	215	215	0	0%
S II	6716	124	124	0	0%
S II	6731	89	89	0	0%
OVERALL PERCENT ERROR:			.73%		

SNR 76

SPECTRAL LINE	λ: WAVELENGTH (nm)	OBSERVED SPECTRAL VALUES	CLOUDY OBTAINED SPECTRAL VALUES	+/-	% ERROR
O III	4959	32	31	-1	3.13%
O III	5007	75	88	+13	17.3%
O I	6300	52	52	0	0%
N II	6548	26	26	0	0%
N II	6583 (6584)	78	78	0	0%
S II	6716	113	103	-10	8.85%
S II	6731	72	72	0	0%
OVERALL PERCENT ERROR:			4.18%		

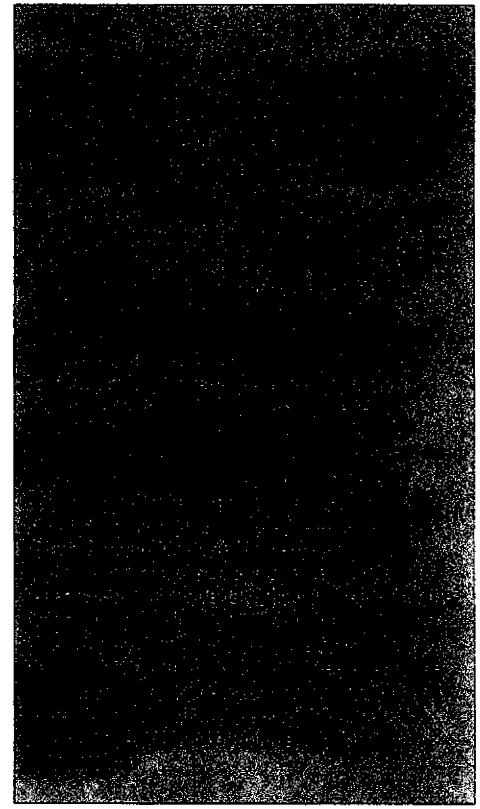

The Astrophysical Journal Supplement Series, 112:49–107, 1997 September

OPTICALLY IDENTIFIED SUPERNOVA REMNANTS IN THE NEARBY SPIRAL GALAXIES NGC 5204, NGC 5585, NGC 6946, M81, AND M101

David M. Matonick and Robert A. Fesen
Department of Physics and Astronomy, 6127 Wilder Laboratory, Dartmouth College, Hanover, NH 03755
Received 1997 January 24; accepted 1997 April 11

ABSTRACT

We present the results of an optical search for supernova remnants (SNRs) in the spiral galaxies NGC 5204, NGC 5585, NGC 6946, M81, and M101. Using the criterion that emission nebulae with [S II]/H$\alpha \geq 0.45$ are identified as SNRs, we found three SNRs in NGC 5204, five in NGC 5585, 27 in NGC 6946, 41 in M81, and 93 in M101. Including the 35 SNRs recently detected in NGC 2403 by Matonick et al., we have doubled the current number of galaxies that have been well searched for SNRs and increased the number of known extragalactic SNRs by about 50%. Since no SNRs were detected inside H II regions and because our optical search appears biased against detecting large, faint SNRs, we estimate that there could be 4 times more SNRs in each of our target galaxies than we detected. Statistical analysis of the spatial distribution of detected SNRs indicates that those in NGC 2403, M81, and M101 are associated with star-forming regions (e.g., H II regions, spiral arms, and molecular clouds), suggesting that a significant fraction of the detected SNRs are the result of SN II or SN Ib/c explosions. Thirty-one SNRs found in these six galaxies have estimated diameters greater than 100 pc, which is larger than is possible for a single SNR in an interstellar medium of density $\sim$0.1–1 cm^{-3}. Such objects are probably combinations of multiple SNRs and massive stellar winds.

We present an overview of extragalactic SNR searches, combining our SNR samples with published results of optical SNR searches in the Large and Small Magellanic Clouds and in M31, M33, NGC 300, and NGC 7793 to create an ensemble of 12 SNR samples. From these data, we find that an important selection effect is the apparent trend for higher $L(\mathrm{H}\alpha)_{\mathrm{mode}}$ with increasing galaxy distance because intrinsically fainter SNRs are more difficult to detect in more distant galaxies. In addition, several physical trends were found in the SNR ensemble, including a constant value of $D_{\mathrm{mode}} \approx 40$ pc for the SNR samples in these galaxies, suggesting that a significant fraction of the detected SNRs are in a similar evolutionary stage.

Subject headings: galaxies: ISM — supernova remnants — surveys

1. INTRODUCTION

The principal advantages of studying supernova remnants (SNRs) in distant galaxies are that (1) an entire galaxy can be examined with relatively few observations, (2) all the SNRs in a galaxy are at essentially the same distance, eliminating the uncertainty in relative distances that exists in the case of Galactic SNRs, and (3) relative positions of SNRs can be determined accurately. A review of extragalactic SNR searches in optical, radio, and X-ray wavelengths is given in Magnier et al. (1995). In Table 1 we list the galaxies in which SNRs (exclusive of remnants from historical SNs) have been detected in optical wavelengths. We also list the galaxy distance, the number of SNRs detected in optical surveys to date, and the principal references in which the SNR surveys were presented. As can be seen from the table, few large, nearby galaxies outside the Local Group ($R > 1$ Mpc) have been thoroughly searched for SNRs.

Mathewson & Clarke (1973a) were the first to use the optical [S II]/Hα criterion to identify remnants. Collisionally excited S$^+$ ions in the long cooling region behind a SNR shock create strong [S II] $\lambda\lambda$ 6716, 6731 emission (Raymond 1979; Dopita et al. 1984; Fesen, Blair, & Kirshner 1985; Osterbrock 1989), typically with [S II]/H$\alpha \gtrsim$ 0.4–0.5. In an H II region, because of the strong photoionization flux of its central star(s), most sulfur is in the form of S^{++}, and therefore [S II]/H$\alpha \approx$ 0.1–0.3. The [S II]/Hα criterion is now a well-established and reliable method for optically detecting SNRs.

As a step toward completing the ground-based search for SNRs in northern hemisphere galaxies and to create a larger ensemble of extragalactic SNR samples, we undertook an optical search for SNRs in five nearby spiral galaxies. We selected low-inclination nearby spiral galaxies with large populations of bright emission regions as targets. In § 2, we describe our observations and methods of data reduction, with the results and analysis of our search discussed in §§ 3 and 4. Comparisons of SNR samples from different galaxies are given in § 5.

2. OBSERVATIONS AND DATA REDUCTIONS

The list of program galaxies is given in Table 2. We restricted our SNR search to galaxies closer than about 7 Mpc. In Table 2 we list the right ascension (R.A.) and declination (decl.) of the galaxy centers as measured from our images in J2000.0 coordinates, the revised Hubble types, the inclinations (i) of the galaxies (Tully 1988), the position angle (P.A.) of each galaxy, measured east of north (de Vaucouleurs et al. 1991; Garcia-Gomez & Athanassoula 1991), the color excess (E_{B-V}) based on obscuration within our Galaxy (Tully 1988; Burstein & Heiles 1978), the heliocentric velocity (V_h) (Tully 1988), and the best estimate of each galaxy's distance (R) (Tully 1988; Freedman & Madore 1988; Freedman et al. 1994).

2.1. *Imaging*

Interference-filter images of the five target galaxies were taken in 1993 June and 1994 March using the f/7.6 1.3 m

TABLE 1

PRIOR OPTICAL EXTRAGALACTIC SNR SEARCH RESULTS

Galaxy	R^a (Mpc)	SNRs Detected[b]	References
LMC	0.055	28	1, 2, 3, 4, 5, 6, 7, 8, 9
SMC	0.063	11	2, 4, 5, 6, 8
NGC 6822	0.56	1	10
IC 1613	0.64	1	10
M31	0.69	221	10, 11, 12, 13, 14, 15
M33	0.84	98	10, 16, 17, 18, 19, 20, 21, 22
NGC 300	2.1	28	10, 23
NGC 253	2.5	2	10
IC 342	2.9	4	10
NGC 2403	3.2	35	10, 24
NGC 7793	3.4	28	23
NGC 4449	5.0	1	25, 26, 27, 28, 29
M101	5.4	1	30, 31, 32
NGC 6946	5.5	1	33, 34, 35, 36

[a] From the given references or from Tully 1988.

[b] Historical SNRs not included.

REFERENCES.—(1) Westerlund & Mathewson 1966; (2, 3, 4) Mathewson & Clarke 1972, 1973a, 1973b, respectively; (5, 6, 7) Mathewson et al. 1983, 1984, 1985, respectively; (8) Chu & Kennicutt 1988a; (9) Smith et al. 1994; (10) D'Odorico, Dopita, & Benvenuti 1980; (11) Rubin, Kumar, & Ford 1972; (12) Kumar 1976; (13) Blair, Kirshner, & Chevalier 1981; (14) Braun & Walterbos 1993; (15) Magnier et al. 1995; (16) Sabbadin & Bianchini 1979; (17) Blair & Kirshner 1985; (18) Long et al. 1990; (19) Smith 1991; (20) Smith et al. 1993; (21) Gordon et al. 1993; (22) Gordon 1994; (23) Blair & Long 1997; (24) Matonick et al. 1997; (25) Balick & Heckman 1978; (26) Kirshner & Blair 1980; (27) Blair, Kirshner, & Winkler 1983; (28) Blair et al. 1984; (29) Long 1985; (30) Skillman 1985; (31) Chu & Kennicutt 1986; (32) Yang, Skillman, & Sramek 1994; (33) Blair & Fesen 1994; (34, 35) Schlegel 1994a, 1994b, respectively; (36) Van Dyk et al. 1994.

McGraw-Hill Telescope at the Michigan-Dartmouth-MIT (MDM) Observatory.[1] These images were obtained using a Tektronix 1024 × 1024 pixel CCD with a plate scale of 0".508 pixel^{-1}, giving a 8'.7 × 8'.7 field of view. Characteristics of the interference filters used are listed in Table 3. Filter tracings for the [S II] and Hα filters were made by E. Carder in a *f*/7.5 beam to match as closely as possible the characteristics of the 1.3 m telescope. The filters were very effective at passing the [S II] and Hα lines and suppressing the [N II] λ6583 line, with only the weaker [N II] λ6548 line contaminating the Hα signal. The λ6446 continuum filter was used to remove starlight from Hα images, and the λ6964 filter was used to do the same for [S II]. These continuum filters do not pass any strong SNR or H II region emission lines. We took sets of three images through each

[1] Michigan-Dartmouth-MIT Observatory is operated by the University of Michigan, Dartmouth College, and the Massachusetts Institute of Technology.

TABLE 3

INTERFERENCE FILTER CHARACTERISTICS

Name	λ_c[a] (Å)	FWHM (Å)	T_{peak} (percent)
[S II]	6728	54	83
Hα	6560	23	80
Continuum	6446	123	81
Continuum	6964	350	92

[a] Central wavelengths for [S II] and Hα measured off filter tracings for *f*/7.5 beam.

filter, with exposure times ranging from 300 to 1200 s. Typical seeing was ≈1".5. Flux standard stars from the catalogs of Oke (1974), Stone (1977), and Massey et al. (1988) were observed each night, and bias frames and dome flats were taken on each run. Twilight flats also were taken in the 1994 March and 1993 June runs. Basic reduction of our images was done using IRAF.[2] In order to produce clearer results in subsequent image arithmetic, we resampled the image data and, while conserving the total flux, extracted four images with a scale of 0".254 pixel^{-1} from each full-frame image. Continuum-subtracted [S II] and Hα images were then constructed.

2.2. *Spectroscopy*

In order to find a set of objects for follow-up spectroscopy, we carried out a quick-look analysis of the data by blinking between the continuum-subtracted [S II] and Hα images. In order to limit the size of the region that the eye had to search, only a region about 1'.5 on a side was displayed and examined at a time. Specifically, we looked for nebulae that were almost as bright, or brighter, in [S II] as in Hα.

Spectra of 39 such nebulae in our five target galaxies were obtained with the 2.4 m Hiltner telescope at MDM Observatory, using the MK III spectrograph with a 600 lines mm^{-1} grism blazed at 5800 Å, giving a spectral coverage of 4800–7200 Å. A 1".68 wide slit was used, yielding a resolution of ≈7 Å with a dispersion of 2.3 Å pixel^{-1}. On one run we also used the Modular Spectrograph, with a 600 lines mm^{-1} grating, spectral coverage of 3700–8300 Å, and resolution of about 10 Å. On the Modular Spectrograph, a 2".5 wide slit was used, with a scale along the slit of 1".396

[2] IRAF is distributed by the National Optical Astronomy Observatories, which is operated by the Association of Universities for Research in Astronomy, Inc. (AURA) under cooperative agreement with the National Science Foundation.

TABLE 2

PROGRAM GALAXIES

Name	R.A. (J2000)	Decl. (J2000)	Type	i (deg)	P.A. (deg)	E_{B-V} (mag)	V_h (km s^{-1})	R (Mpc)
NGC 3031 (M81)	09 55 33	69 03 55	Sab	60	157	0.04	−43	3.6
NGC 5204	13 29 36	58 25 15	Sm	53	5	0.00	200	4.8
NGC 5457 (M101)	14 03 12	54 20 56	Scd	0	...	0.00	231	5.4
NGC 5585	14 19 48	56 43 47	Sd	51	30	0.00	303	7.0
NGC 6946	20 34 52	60 09 14	Scd	42	64	0.40	46	5.5

NOTE.—Units of right ascension are hours, minutes, and seconds, and units of declination are degrees, arcminutes, and arcseconds.

pixel^{-1} and a dispersion of 4.69 Å pixel^{-1}. A Tektronix 1024 × 1024 pixel CCD was used in all observations. The slit was positioned on the target nebula by setting it on a bright star in the field and rotating the instrument platform so that the slit overlaid both the star and the target. Exposures usually consisted of three frames of 600 s each.

A total of 14 objects were spectroscopically observed in M101, 12 in NGC 6946, six in M81, four in NGC 5585, and three in NGC 5204. In addition to our SNR candidate targets, spectra were also extracted of some H II regions lying along the slit. Three or four spectrophotometric flux standard stars from the catalogs of Oke (1974), Stone (1977), and Massey et al. (1988) were observed each night. Calibration frames consisted of biases, internal lamp flats, and comparison lamp exposures. Spectral data were reduced, extracted, and corrected for interstellar extinction using IRAF. The [S II]/Hα ratio was measured for each spectroscopically observed object, with spectral line ratios accurate to about 10%.

2.3. *SNR Identification Technique*

To carry out a systematic search for SNR candidates in our program galaxies, we constructed "difference" images similar to those used by Braun & Walterbos (1993) in their search for SNRs in M31. For complex fields, they used continuum-subtracted Hα and [S II] images and made an image by taking $I(\mathrm{H}\alpha) - 2I([\mathrm{S\,II}])$, which left any region of high [S II]/Hα with negative pixels, which could then be more easily discerned on an image display. Modifying this method, we took the continuum-subtracted Hα and [S II] images and made a difference image by taking $I([\mathrm{S\,II}]) - nI(\mathrm{H}\alpha)$, where $n \approx 0.4$ and setting any negative pixels to zero. Any bright feature in a difference image that was verified as a real emission-line object was marked as a SNR candidate. An example of these steps is shown in Figure 1 for a small section of the north field of M81.

We measured the total counts for each SNR candidate in [S II] and Hα, converted counts to flux using standard stars, corrected for interstellar extinction within the Galaxy, and calculated $([\mathrm{S\,II}]/\mathrm{H}\alpha)_{\mathrm{image}}$. These image line ratios were then corrected for contamination by the [N II] λ6548 line in the Hα filter and Hα absorption in the standard stars by fitting a curve to an $([\mathrm{S\,II}]/\mathrm{H}\alpha)_{\mathrm{image}}$ versus $([\mathrm{S\,II}]/\mathrm{H}\alpha)_{\mathrm{spectrum}}$ plot and using this curve to obtain corrected values of [S II]/Hα for objects that were not spectroscopically observed. Two examples of these plots and the correction procedure are shown in Figure 2. The corrected line ratios are accurate to about 15%. Overlap between galaxy fields was taken into account. Using the [S II]/Hα ratios, either corrected or obtained directly from spectra, an improved value of Hα intensity was calculated by taking

$$I(\mathrm{H}\alpha) = \frac{I([\mathrm{S\,II}])}{[\mathrm{S\,II}]/\mathrm{H}\alpha},$$

thereby correcting for [N II] λ6548 contamination in the Hα filter, Hα absorption lines in the standard stars, and any nonphotometric conditions in the Hα imaging observations. Objects with $[\mathrm{S\,II}]/\mathrm{H}\alpha \geq 0.45$ were considered SNRs.

Positions of all objects identified as SNRs were obtained in J2000 coordinates by use of *Hubble Space Telescope* (*HST*) guide stars in each field and refer to the center of the aperture used to measure the flux of each object. Diameters were measured on the continuum-subtracted [S II] images,

FIG. 1*a*

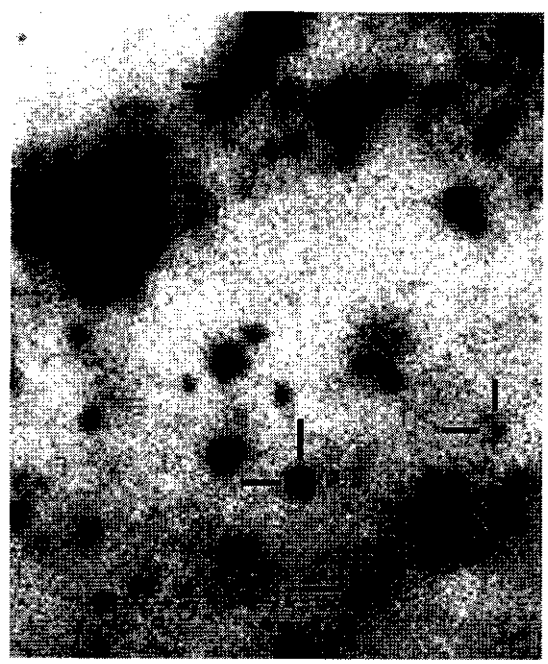

FIG. 1*b*

FIG. 1.—(*a*) [S II] and (*b*) Hα images of a small (1'.3 × 1'.6) subfield of M81. Objects later identified as SNRs are marked, from top to bottom, as M81 Nos. 19, 13, 17, and 15. (*c*) λ6964 continuum image of the same subfield. (*d*) [S II] and (*e*) Hα continuum-subtracted images of the subfield. (*f*) $I([\mathrm{S\,II}]) - 0.4I(\mathrm{H}\alpha)$ image of the subfield. Note how clearly the objects identified as SNRs stand out in the final frame (*f*).

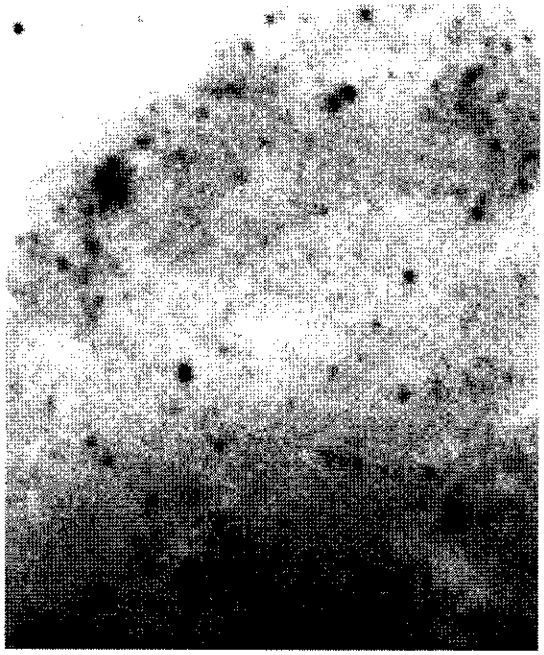

FIG. 1c

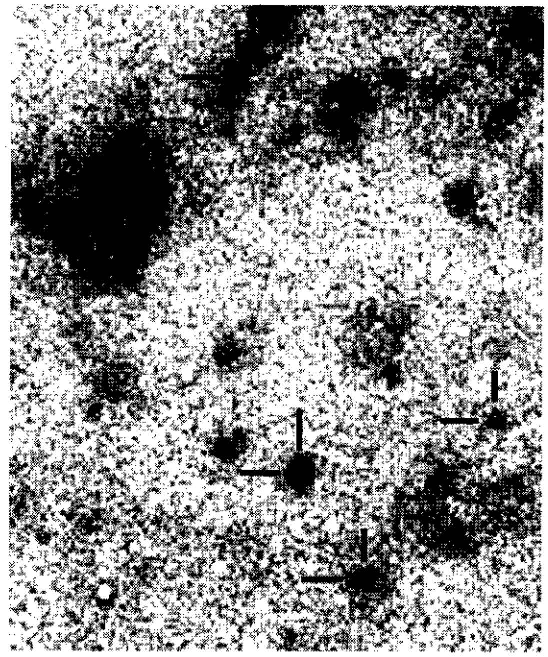

FIG. 1d

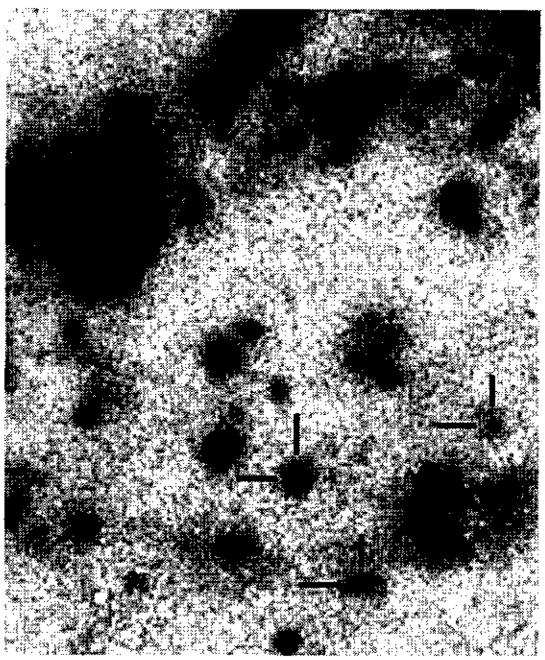

FIG. 1e

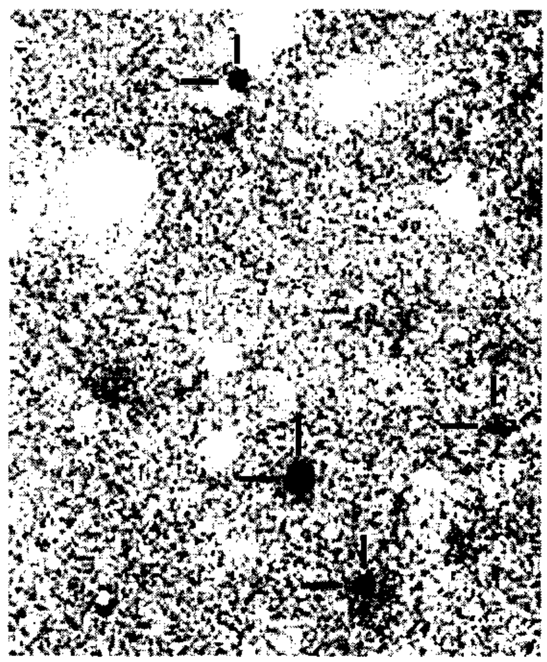

FIG. 1f

using a method which depended on object morphology. For a shell structure, an ellipse was fitted to the brightest portion of the shell. Arcs were fitted in the same way as shells, assuming that the arc represented the visible part of a circular object. Filled SNRs were fitted with an isophote at the point where the counts were about 5 times the local average background in the image. Among these three types of resolved objects, shells were probably the most reliably measured. For a filled object, fitting an isophote was less certain because it was easier to overestimate the object's

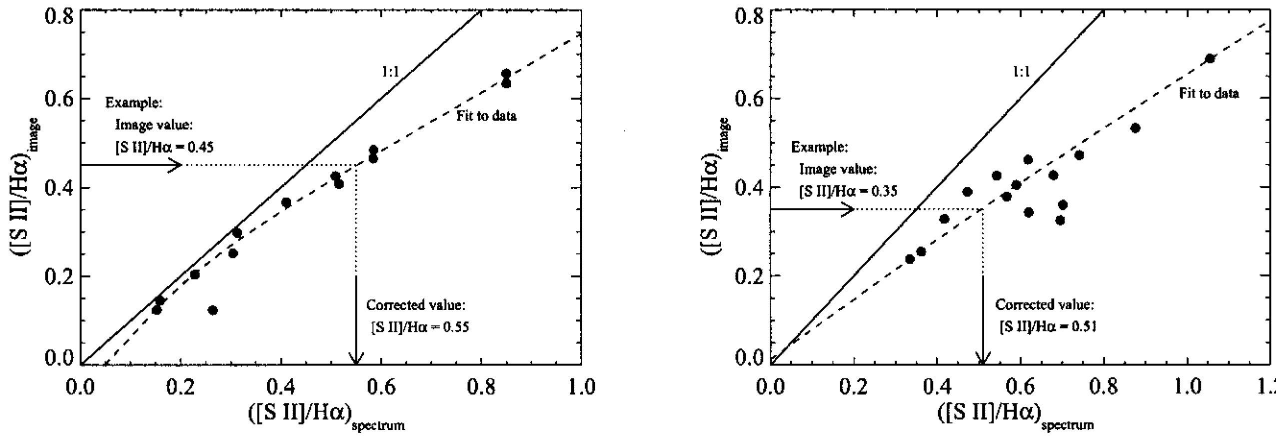

FIG. 2a FIG. 2b

FIG. 2.—Plots of [S II]/Hα ratios from image data vs. [S II]/Hα ratios from spectra for two of the galaxies. Note how the points deviate more from a 1:1 relationship (*solid line*) with higher [S II]/Hα. Examples of how the $([\mathrm{S\,II}]/\mathrm{H}\alpha)_{\mathrm{image}}$ values were corrected for [N II] λ6548 contamination are also shown. (*a*) NGC 6946. The dashed line is a first-order cubic spline fit to the data. (*b*) M101 south field. Includes objects calibrated in overlapping fields. The dashed line is a third-order polynomial fit. We were most concerned with the fits for ratio values $\gtrsim 0.2$. In some cases, the fit was simply a straight line, and the correction was identical to increasing the image ratios by a constant factor. The [S II]/Hα values of objects for which we had spectra were obtained from the spectra, and this correction was not applied.

size. For arclike objects, we ignored the possibility that the arc might be part of an elliptically shaped object, in which case we might have overestimated the object's size. Partially resolved SNRs were measured by fitting a Gaussian to the point-spread function of the SNR. The measured SNR diameter was then deconvolved using the average FWHM of stars in the remnant's field. We were unable to estimate diameters for some of our SNRs, particularly those in very confused regions and those that were either unresolved or too faint to allow a Gaussian to be fit accurately.

3. SNR DETECTION RESULTS

SNRs detected in each galaxy are listed with objects ordered in right ascension in Tables 4–12. Each table contains the SNR's designated number (e.g., M81 SNR No. 15), the right ascension and declination in J2000 coordinates, the field in which the SNR was observed, the estimated diameter in parsecs (with major and minor axes given for highly elliptical remnants), the Hα intensity, the [S II]/Hα ratio, information on whether the SNR was observed spectroscopically, and a brief description of the SNR's morphology. Positions are accurate to 1″, diameters to about ±10 pc, Hα intensities to ±15%, and [S II]/Hα ratios to ±15% (see also Matonick 1997). Objects for which no value of the diameter is given were in confused regions or were too small and faint to be estimated. Note that ground-based measurements of extragalactic SNR diameters have been found to differ from *HST* measurements by ~20% to nearly a factor of 3 (Blair & Davidsen 1993). Therefore, SNR diameter estimates from ground-based observations should be interpreted with caution.

Finding charts showing the locations of all remnants identified are presented below. (For objects that are difficult to discern on these finding charts, see Matonick 1997). For each galaxy, we show images (mostly in Hα) of the whole galaxy field, as well as a few smaller areas to better display the SNRs. Numbered tick marks show the location of each remnant, using the numbers in the SNR tables. Light and dark numbers and tick marks were used to facilitate readability. North is up and east to the left in all finding charts.

We also investigated whether or not the remnants of any historical SNs were detected by our methods. Although SN 1993J in M81 is visible in our images (Finn et al. 1995), it would not have been detected by our search methods alone. To check for other historical SNs, we used the positional information in Barbon, Cappellaro, & Turatto (1989) and found that, although some SNs occurred within our observed galaxy fields, no emission was visible in our

TABLE 4

NGC 5204 SUPERNOVA REMNANTS

SNR No.	R.A. (J2000)	Decl. (J2000)	Diameter[a] (pc)	I(Hα) (ergs cm^{-2} s^{-1})	[S II]/Hα	Spectra?	Morphology
1	13 29 30.2	58 25 21.1	20	1.7E−15	0.53	No	Stellar
2	13 29 34.4	58 24 24.8	60	1.1E−14	0.69	Yes	Arc
3	13 29 36.9	58 24 26.2	50	3.7E−15	0.52	Yes	Stellar

NOTE.—Units of right ascension are hours, minutes, and seconds, and units of declination are degrees, arcminutes, and arcseconds.

[a] R = 4.8 Mpc.

TABLE 5

RELATIVE LINE INTENSITIES FOR NGC 5204 SNRs WITH SPECTRA

LINE	SNR No. 2	3
Hβ λ4861	100	100
[O III] λ4959	25	36
[O III] λ5007	99	92
[N I] λ5200	...	...
He I λ5876	...	...
[O I] λ6300	48	37
[O I] λ6364	20	...
[N II] λ6548	16	12
Hα λ6563	300	300
[N II] λ6583	30	34
[S II] λ6716	119	97
[S II] λ6731	90	58
SNR Parameters:		
sec z	1.12	1.12
E_{B-V}	0.54	0.13
I(Hα)[a]	1.1E−14	3.7E−15

[a] From photometry, given in units of ergs cm^{-2} s^{-1}.

TABLE 6

NGC 5585 SUPERNOVA REMNANTS

SNR No.	R.A. (J2000)	Decl. (J2000)	Diameter[a] (pc)	I(Hα) (ergs cm^{-2} s^{-1})	[S II]/Hα	Spectra?	Morphology
1	14 19 39.2	56 41 38.7	200 × 90	1.6E−14	0.66	Yes	Shell
2	14 19 49.2	56 44 58.4	30	1.5E−15	0.68	No	Stellar
3	14 19 51.6	56 44 21.0	20	4.3E−15	0.64	Yes	Filled
4	14 19 51.8	56 44 08.6	120 × 30	3.1E−14	0.47	Yes	Filled
5	14 19 55.4	56 45 08.0	...[b]	1.5E−14	0.49	Yes	...

NOTE.—Units of right ascension are hours, minutes, and seconds, and units of declination are degrees, arcminutes, and arcseconds.

[a] R = 7.0 Mpc. Elliptical remnants are described as, e.g., "200 × 90", where the numbers denote the length of the major and the minor axis, respectively.

[b] Object too close to nearby H II region to allow estimation of diameter.

TABLE 7

RELATIVE LINE INTENSITIES FOR NGC 5585 SNRs WITH SPECTRA

LINE	SNR No. 1	3	4	5
Hβ λ4861	100	...	100	100
[O III] λ4959	31	...	63	20
[O III] λ5007	74	...	245	44
[N I] λ5200	...	...	...	...
He I λ5876	...	...	...	...
[O I] λ6300	72	...	...	32
[O I] λ6364	14	...	...	14
[N II] λ6548	11	...	23	11
Hα λ6563	300	300	300	300
[N II] λ6583	31	50	47	31
[S II] λ6716	116	115	87	86
[S II] λ6731	83	70	57	63
SNR Parameters:				
sec z	1.10	1.12	1.10	1.17
E_{B-V}	0.00	0.00[a]	0.51	0.14
I(Hα)[b]	1.6E−14	4.3E−15	3.1E−14	1.5E−14

[a] Burstein & Heiles 1978.

[b] From photometry, given in units of ergs cm^{-2} s^{-1}.

TABLE 8

NGC 6946 Supernova Remnants

SNR No.	R.A. (J2000)	Decl. (J2000)	Diameter[a] (pc)	I(Hα) (ergs cm^{-2} s^{-1})	[S II]/Hα	Spectra?	Morphology
1	20 34 23.3	60 08 18.6	30	6.7E−15	0.52	No	Stellar
2	20 34 26.0	60 11 10.6	30	4.7E−15	0.46	No	Stellar
3	20 34 33.6	60 09 52.4	40	7.7E−16	0.91	No	Stellar
4	20 34 33.8	60 09 25.2	...	3.3E−15	0.85	Yes	...
5	20 34 37.6	60 08 52.7	180	2.0E−15	0.76	No	Arc
6	20 34 37.8	60 11 54.5	20	5.3E−16	1.14	No	Stellar
7	20 34 37.9	60 07 22.5	40	1.4E−15	0.97	No	Stellar
8	20 34 43.9	60 08 24.6	50	4.4E−15	0.49	No	Stellar
9	20 34 51.4	60 07 39.2	20	2.2E−15	0.67	No	Stellar
10	20 34 51.5	60 09 09.1	20	3.7E−15	0.77	No	Stellar
11	20 34 52.5	60 07 28.3	...	2.9E−15	0.46	No	...
12	20 34 54.2	60 11 03.5	...	1.5E−15	0.64	No	...
13	20 34 55.9	60 07 49.2	9	3.2E−15	0.58	No	Stellar
14	20 34 57.8	60 08 10.0	20	2.5E−15	0.68	No	Stellar
15	20 35 00.3	60 11 46.2	30	7.9E−15	0.58	Yes	Stellar
16	20 35 00.6	60 11 30.8	20	7.1E−14	0.85	Yes[b]	Stellar
17	20 35 01.1	60 12 00.3	20	1.0E−15	0.77	No	Stellar
18	20 35 02.3	60 06 31.2	40	6.7E−15	0.52	Yes	Stellar
19	20 35 02.9	60 05 26.7	160	1.4E−14	0.71	No	Diffuse
20	20 35 05.5	60 10 01.0	...	3.8E−15	0.68	No	...
21	20 35 08.8	60 06 03.0	180	8.1E−15	0.94	No	Diffuse
22	20 35 09.6	60 12 30.2	...	2.9E−15	0.77	No	...
23	20 35 11.6	60 07 41.2	30	7.3E−15	0.45	No	Stellar
24	20 35 16.9	60 11 05.8	50	2.1E−15	0.79	No	Stellar
25	20 35 21.1	60 08 44.4	60	2.1E−14	0.58	Yes	Stellar
26	20 35 25.5	60 07 51.2	30	2.1E−15	0.59	No	Stellar
27	20 35 26.0	60 08 43.0	40	1.1E−14	0.51	Yes	Stellar

Note.—Units of right ascension are hours, minutes, and seconds, and units of declination are degrees, arcminutes, and arcseconds.

[a] $R = 5.5$ Mpc.

[b] Blair & Fesen 1994.

images at their reported positions. These objects were SN 1954J in NGC 2403 and SNs 1917A, 1939C, 1948B, 1968D, and 1969P in NGC 6946. SN 1970G in M101 has been recently recovered by Fesen (1993), but it was not detectable as a remnant by our technique.

3.1. *NGC 5204*

Three SNRs with [S II]/Hα ratios ranging from 0.52 to 0.69 and diameters of 20–60 pc, located predominantly in the southwest region of the galaxy, were found in this small,

TABLE 9

Relative Line Intensities for NGC 6946 SNRs with Spectra

Line	SNR No. 4	15	16[a]	18	25	27
Hβ λ4861	...	100	100	100	100	100
[O III] λ4959	...	31	210	...	...	...
[O III] λ5007	...	110	670	...	40	21
[N I] λ5200	...	...	18	...	...	...
He I λ5876	...	...	15	...	...	...
[O I] λ6300	78	...	85	...	22	32
[O I] λ6364	...	...	27	...	...	...
[N II] λ6548	66	34	90	36	41	26
Hα λ6563	300	300	300	300	300	300
[N II] λ6583	217	126	255	133	106	100
[S II] λ6716	143	106	140	83	99	89
[S II] λ6731	110	70	115	71	72	66
SNR Parameters:						
sec z	1.22	1.78	1.14	1.71	1.53	1.82
E_{B-V}	0.40[b]	0.45	0.56	0.40	0.75	0.55
I(Hα)[c]	3.3E−15	7.9E−15	7.1E−14	6.7E−15	2.1E−14	1.1E−14

[a] Blair & Fesen 1994.

[b] Burstein & Heiles 1978.

[c] From photometry, given in units of ergs cm^{-2} s^{-1}.

TABLE 10

M81 SUPERNOVA REMNANTS

SNR No.	R.A. (J2000)	Decl. (J2000)	Field	Diameter (pc)[a]	$I(H\alpha)$ (ergs cm^{-2} s^{-1})	[S II]/Hα	Spectra?	Morphology
1	9 54 44.8	69 04 24.3	West	120	4.7E−15	1.20	No	Arc
2	9 54 46.3	69 03 28.6	West	60	1.6E−15	0.72	Yes	Filled
3	9 54 47.5	69 03 56.5	West	50	3.6E−15	0.71	No	Stellar
4	9 54 51.3	69 02 58.5	West	40	2.9E−15	0.58	No	Stellar
5	9 54 54.6	69 09 20.2	North	20	2.8E−15	0.53	No	Stellar
6	9 54 55.1	69 01 14.6	West	40	1.4E−15	0.86	No	Stellar
7	9 55 00.2	69 08 05.8	North	20	1.9E−15	1.01	No	Stellar
8	9 55 04.5	69 05 55.2	North	...	8.8E−16	1.28	No	...
9	9 55 04.8	69 05 51.2	North	10	8.7E−16	1.27	No	Stellar
10	9 55 07.3	69 03 14.0	West	30	1.7E−15	1.10	No	Stellar
11	9 55 09.6	69 04 14.6	West	40	1.4E−15	1.58	No	Stellar
12	9 55 10.5	69 08 47.0	North	40	1.1E−15	1.04	No	Stellar
13	9 55 14.5	69 07 41.4	North	...	1.5E−15	1.07	No	...
14	9 55 16.3	69 03 02.4	West	110 × 80	7.9E−15	0.58	No	Filled
15	9 55 18.2	69 07 17.7	North	20	3.4E−15	0.63	No	Stellar
16	9 55 19.3	69 09 32.7	North	30	4.6E−15	0.63	No	Stellar
17	9 55 20.0	69 07 33.2	North	30	8.6E−15	1.22	Yes	Stellar
18	9 55 21.7	69 01 47.2	West	130	3.6E−14	0.70	Yes	Filled
19	9 55 21.7	69 08 32.0	North	20	9.4E−15	0.53	No	Stellar
20	9 55 22.7	69 12 55.7	North	40	1.1E−15	0.94	No	Stellar
21	9 55 32.2	68 56 47.7	South	20	1.2E−15	1.17	No	Stellar
22	9 55 32.7	69 00 32.9	West	90	1.1E−14	0.85	No	Filled
23	9 55 33.8	69 00 40.2	West	...	1.7E−15	1.26	No	...
24	9 55 41.5	69 07 02.0	North	...	1.6E−15	0.76	No	...
25	9 55 42.2	69 07 00.9	North	10	3.9E−15	0.93	Yes	Stellar
26	9 55 52.4	69 05 22.2	Southeast	...	2.2E−15	0.88	No	...
27	9 55 52.5	68 59 16.6	Southeast	...	5.8E−15	0.62	No	...
28	9 56 04.2	68 59 16.2	South	10	6.4E−15	0.49	No	Stellar
29	9 56 04.7	68 59 00.1	Southeast	...	4.4E−15	0.66	No	...
30	9 56 11.7	68 57 35.2	South	90	4.8E−15	0.67	No	Filled
31	9 56 15.6	69 04 59.4	East	...	8.4E−16	1.48	No	...
32	9 56 16.0	69 00 51.7	South	20	7.5E−16	1.64	No	Stellar
33	9 56 16.4	69 02 39.5	East	20	2.3E−15	1.33	No	Stellar
34	9 56 18.3	69 00 28.3	South	...	6.6E−16	1.16	No	...
35	9 56 21.9	69 05 01.2	East	30	4.3E−15	1.02	No	Stellar
36	9 56 23.2	69 04 14.6	Southeast	...	5.0E−15	0.70	No	...
37	9 56 24.7	69 04 27.5	East	...	2.5E−15	0.95	No	...
38	9 56 25.9	69 04 17.0	East	...	1.7E−15	1.02	No	...
39	9 56 29.7	68 55 53.9	South	20	6.0E−16	1.56	No	Stellar
40	9 56 29.9	68 56 16.6	South	100	2.0E−14	0.45	No	Shell
41	9 56 31.3	69 01 23.2	Southeast	60	1.1E−15	0.88	No	Filled

NOTE.—Units of right ascension are hours, minutes, and seconds, and units of declination are degrees, arcminutes, and arcseconds.

[a] $R = 3.6$ Mpc. Elliptical remnants are described as, e.g., "200 × 90", where the numbers denote the length of the major and the minor axis, respectively.

TABLE 11

RELATIVE LINE INTENSITIES FOR M81 SNRs WITH SPECTRA

LINE	SNR No. 2	17	18	25
Hβ λ4861	...	100	100	100
[O III] λ4959	...	52	...	78
[O III] λ5007	...	172	31	263
[N I] λ5200	...	...	...	...
He I λ5876	...	...	...	...
[O I] λ6300	...	101	18	59
[O I] λ6364	...	32	5	28
[N II] λ6548	...	94	69	105
Hα λ6563	300	300	300	300
[N II] λ6583	162	298	179	268
[S II] λ6716	136	207	135	155
[S II] λ6731	81	157	74	127
SNR Parameters:				
sec z	1.47	1.34	1.47	1.44
E_{B-V}	0.04[a]	0.18	0.23	0.22
$I(H\alpha)$[b]	1.6E−15	8.6E−15	3.6E−14	3.9E−15

[a] Burstein & Heiles 1978.

[b] From photometry, given in units of ergs cm^{-2} s^{-1}.

TABLE 12

M101 SUPERNOVA REMNANTS

SNR No.	R.A. (J2000)	Decl. (J2000)	Field	Diameter[a] (pc)	$I(H\alpha)$ (ergs cm^{-2} s^{-1})	[S II]/Hα	Spectra?	Morphology
1	14 02 20.0	54 21 36.2	West	130 × 90	8.5E−15	0.51	No	Filled
2	14 02 24.6	54 17 58.5	West	...	8.8E−16	0.63	No	...
3	14 02 25.0	54 17 46.0	West	40	1.3E−15	0.72	No	Stellar
4	14 02 25.7	54 18 35.7	West	...	3.8E−15	0.58	No	...
5	14 02 27.1	54 16 54.4	West	...	2.2E−15	0.60	No	...
6	14 02 32.2	54 15 57.2	West	30	2.7E−15	0.59	No	Stellar
7	14 02 32.8	54 25 54.0	North	80	8.2E−16	1.59	No	Filled
8	14 02 36.3	54 23 57.5	North	150 × 90	1.4E−15	0.83	No	Filled
9	14 02 38.4	54 22 24.7	West	40	2.1E−15	0.67	No	Stellar
10	14 02 41.2	54 16 08.8	West	350 × 250	1.3E−14	0.78	No	Filled
11	14 02 41.7	54 22 36.0	North	30	2.3E−15	0.81	No	Stellar
12	14 02 43.8	54 20 05.5	West	120	9.7E−15	0.54	No	Filled
13	14 02 44.1	54 20 34.4	West	30	1.1E−15	0.69	No	Stellar
14	14 02 45.5	54 13 26.7	South	70	3.7E−15	0.59	No	Stellar
15	14 02 45.6	54 25 22.8	North	...	1.5E−14	0.51	No	Diffuse
16	14 02 46.0	54 24 41.0	North	50	9.6E−16	0.46	No	Stellar
17	14 02 49.0	54 20 55.7	West	40	6.8E−15	0.90	Yes	Stellar
18	14 02 49.5	54 14 35.7	West	60	3.0E−15	0.62	No	Stellar
19	14 02 49.7	54 22 45.5	North	140	2.1E−14	0.93	Yes	Filled
20	14 02 49.9	54 18 55.7	West	20	6.3E−15	0.59	No	Stellar
21	14 02 51.2	54 17 46.0	West	30	1.9E−14	0.88	Yes	Stellar
22	14 02 51.4	54 17 49.5	West	50	5.1E−15	0.68	No	Stellar
23	14 02 51.5	54 29 08.1	North	40	4.0E−15	0.55	No	Stellar
24	14 02 51.8	54 19 32.4	West	30	7.2E−15	1.06	Yes	Stellar
25	14 02 53.5	54 14 24.1	West	30	7.5E−15	0.70	No	Stellar
26	14 02 54.4	54 23 24.7	North	<2	2.8E−15	0.56	No	Stellar
27	14 02 55.2	54 24 17.2	North	40	7.4E−16	1.14	No	Stellar
28	14 02 56.0	54 14 57.2	West	10	2.3E−15	0.74	No	Stellar
29	14 02 58.2	54 18 33.7	West	20	9.0E−16	0.67	No	Stellar
30	14 02 59.1	54 19 49.7	West	30	2.0E−15	0.77	No	Stellar
31	14 02 59.1	54 17 02.5	South	...	1.5E−14	0.59	No	...
32	14 02 59.5	54 22 45.2	North	20	3.5E−15	0.74	No	Stellar
33	14 03 00.5	54 20 02.4	West	10	8.0E−15	0.70	Yes	Stellar
34	14 03 02.0	54 23 24.7	North	30	3.6E−15	0.61	No	Stellar
35	14 03 03.5	54 14 29.3	South	50	3.2E−15	0.57	No	Stellar
36	14 03 03.9	54 14 03.5	West	150 × 110	3.4E−15	0.70	No	Filled
37	14 03 04.1	54 27 36.0	North	...	6.9E−15	0.72	No	...
38	14 03 06.5	54 28 17.1	North	130 × 50	3.3E−15	0.71	Yes	Filled
39	14 03 09.0	54 16 25.2	West	30	3.3E−15	0.55	No	Stellar
40	14 03 09.3	54 18 31.8	East	40	2.1E−15	0.68	No	Stellar
41	14 03 10.5	54 23 27.1	East	20	4.1E−15	0.45	No	Stellar
42	14 03 11.0	54 22 03.2	East	30	1.5E−15	0.64	No	Stellar
43	14 03 12.1	54 18 52.0	East	20	1.1E−15	0.78	No	Stellar
44	14 03 12.2	54 23 27.2	East	...	2.5E−14	0.53	Yes	...
45	14 03 12.7	54 17 34.9	East	110 × 80	8.7E−15	0.47	No	Filled
46	14 03 12.7	54 19 00.8	East	50	1.5E−15	0.48	No	Stellar
47	14 03 13.0	54 24 38.7	North	...	1.5E−15	0.54	No	...
48	14 03 13.2	54 17 07.5	East	...	1.7E−14	0.49	No	...
49	14 03 13.2	54 21 56.7	East	20	1.7E−15	0.52	No	Stellar
50	14 03 14.5	54 21 51.7	East	9	2.5E−15	0.81	Yes	Stellar
51	14 03 17.3	54 17 10.8	East	120	1.0E−14	0.50	No	Filled
52	14 03 18.0	54 17 54.0	East	9	9.4E−16	0.64	No	Stellar
53	14 03 20.7	54 16 52.5	East	170	9.6E−15	0.73	No	Shell
54	14 03 20.7	54 19 42.2	East	20	5.7E−15	0.52	No	Stellar
55	14 03 23.1	54 22 47.7	East	30	1.1E−15	0.70	No	Stellar
56	14 03 24.0	54 21 44.2	East	30	1.9E−15	0.51	No	Stellar
57	14 03 24.2	54 19 44.0	East	30	1.8E−15	0.47	No	Stellar
58	14 03 24.5	54 25 01.9	North	150 × 90	5.3E−15	0.60	No	Filled
59	14 03 24.8	54 17 21.6	East	40	1.7E−15	0.69	No	Stellar
60	14 03 25.4	54 18 22.7	East	20	2.9E−15	0.65	No	Stellar
61	14 03 25.7	54 21 24.7	East	30	4.6E−15	0.48	No	Stellar
62	14 03 26.3	54 24 32.9	East	50	7.1E−15	0.50	No	Stellar
63	14 03 26.7	54 23 41.5	East	...	6.5E−15	0.46	No	...
64	14 03 26.8	54 20 44.5	East	<2	1.9E−15	0.69	No	Stellar
65	14 03 27.2	54 18 31.2	East	50	5.6E−15	0.57	No	Stellar
66	14 03 27.6	54 17 08.6	East	30	3.9E−15	0.57	No	Stellar
67	14 03 27.7	54 24 30.8	North	190 × 140	6.9E−15	0.46	No	Arc
68	14 03 28.2	54 23 04.8	East	20	2.8E−15	0.46	No	Stellar
69	14 03 28.4	54 24 11.0	East	100 × 70	7.5E−15	0.50	No	Filled
70	14 03 28.6	54 17 01.3	East	110	1.2E−14	0.54	No	Filled
71	14 03 28.7	54 23 17.7	East	30	2.0E−14	0.76	Yes	Stellar
72	14 03 30.3	54 23 39.5	East	30	9.1E−15	0.50	No	Stellar

TABLE 12—*Continued*

SNR No.	R.A. (J2000)	Decl. (J2000)	Field	Diameter[a] (pc)	$I(H\alpha)$ (ergs cm^{-2} s^{-1})	[S II]/Hα	Spectra?	Morphology
73........	14 03 30.7	54 24 42.0	East	...	4.7E−15	0.53	No	...
74........	14 03 30.8	54 21 06.6	East	30	5.2E−15	0.48	No	Stellar
75........	14 03 32.3	54 17 40.9	East	50	7.0E−15	0.48	No	Stellar
76........	14 03 32.8	54 17 41.0	East	...	6.3E−15	0.62	Yes	...
77........	14 03 33.8	54 20 16.2	East	40	1.9E−15	0.58	No	Stellar
78........	14 03 34.0	54 17 41.5	East	230	3.8E−15	0.49	No	Arc
79........	14 03 34.4	54 22 17.3	East	40	4.7E−15	0.45	No	Stellar
80........	14 03 34.5	54 21 57.0	East	120	3.5E−15	0.45	No	Filled
81........	14 03 35.6	54 18 12.8	East	30	9.4E−16	0.60	No	Stellar
82........	14 03 35.7	54 27 17.0	Northeast	...	4.2E−15	0.52	No	...
83........	14 03 35.9	54 19 24.1	East	200	2.8E−14	0.76	Yes	Shell
84........	14 03 36.0	54 31 42.0	Northeast	130	1.5E−14	0.51	No	Filled
85........	14 03 40.2	54 18 21.2	East	50	4.2E−15	0.60	No	Shell
86........	14 03 41.0	54 32 12.0	Northeast	...	2.5E−15	0.73	No	...
87........	14 03 42.2	54 29 54.0	Northeast	230 × 160	4.7E−14	0.48	No	Shell
88........	14 03 51.7	54 21 03.0	East	...	2.5E−15	0.69	No	...
89........	14 03 52.4	54 21 30.3	East	30	1.0E−14	0.62	No	Stellar
90........	14 03 53.0	54 21 17.2	East	40	6.9E−15	0.64	No	Stellar
91........	14 03 53.7	54 21 24.5	East	30	6.2E−15	0.71	No	Stellar
92........	14 03 59.7	54 24 35.0	Northeast	120	7.6E−15	0.52	No	Filled
93........	14 04 02.9	54 24 48.0	Northeast	90	5.2E−15	0.59	No	Filled

NOTE.—Units of right ascension are hours, minutes, and seconds, and units of declination are degrees, arcminutes, and arcseconds.

[a] $R = 5.4$ Mpc. Elliptical remnants are described as, e.g., "200 × 90", where the numbers denote the length of the major and minor axis, respectively.

irregular spiral (see Table 4). An Hα image of the central region of NGC 5204 with the SNRs marked is shown in Figure 3. Spectra of SNRs Nos. 2 and 3 are presented in Figure 4, with relative line intensities, E_{B-V} values, air masses, and Hα intensities given in Table 5. Lines for which no values were given in spectral tables were below the 3 σ threshold for detection. All these NGC 5204 SNR spectra show relatively weak [N II] λλ6548, 6583 lines. A typical H II region spectrum from NGC 5204 is shown for comparison in Figure 5.

3.2. *NGC 5585*

Five SNRs were found in this Sd galaxy. The SNRs have [S II]/Hα ratios ranging from 0.47 to 0.68, diameters from 20 to 200 pc, are of a variety of morphologies, and are located mostly in the northeast region of the galaxy. A listing of the SNRs detected in NGC 5585 is given in Table 6. A finding chart for the NGC 5585 SNRs is shown in Figure 6, with spectra of four of the SNRs shown in Figure 7. Note in these spectra, as in those of the SNRs in NGC

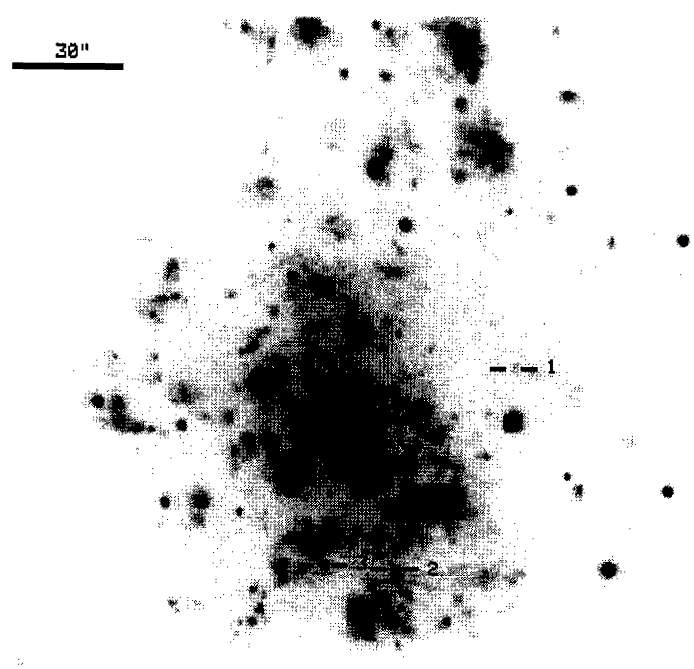

FIG. 3.—Hα image of the central region of NGC 5204, with SNRs marked

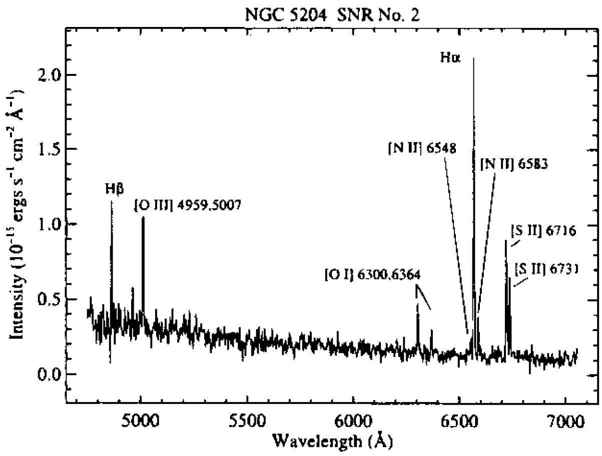

FIG. 4a

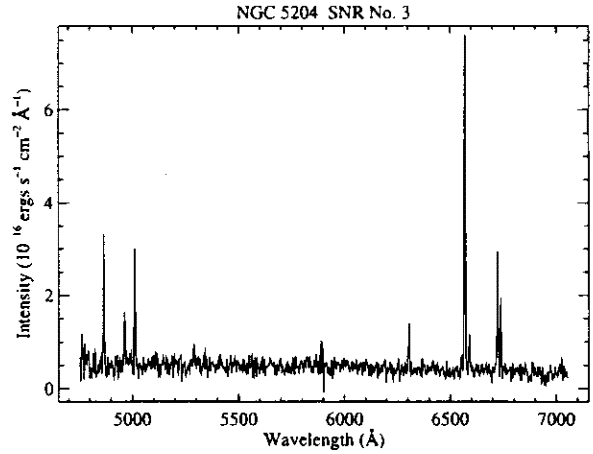

FIG. 4b

FIG. 4.—NGC 5204 SNR spectra

5204, that the lines of [N II], especially [N II] λ6548, are quite weak relative to the Hα emission, meaning that [N II] contamination in our Hα filter images was relatively insignificant. SNR line intensities relative to Hα, as well as the air mass at observation, the measured E_{B-V}, and the Hα intensity are listed in Table 7.

A particularly interesting SNR detected in NGC 5585 is SNR No. 1. This enormous (200 × 90 pc) object sits immediately south of a small point-source H II region. Elliptical in shape, SNR No. 1 shows a distinctive shell structure that, while only slightly evident in Hα, can be seen quite clearly in a [S II] image. No strong continuum source(s) could be seen in projection near the center of this object. Fabbiano, Kim, & Trinchieri (1992) published an *Einstein* Imaging Proportional Counter (IPC) contour map of the X-ray emission detected in NGC 5585 that consists of only two contour levels with no point sources detected. However, the peak of the contours is not centered on the optically bright nucleus of NGC 5585 but is offset slightly to the southwest, toward SNR No. 1, which is contained within the peak of the contours. This fact suggests that the IPC contours may have been influenced by X-ray emission from SNR No. 1. *ROSAT* High Resolution Imager (HRI) data on this galaxy

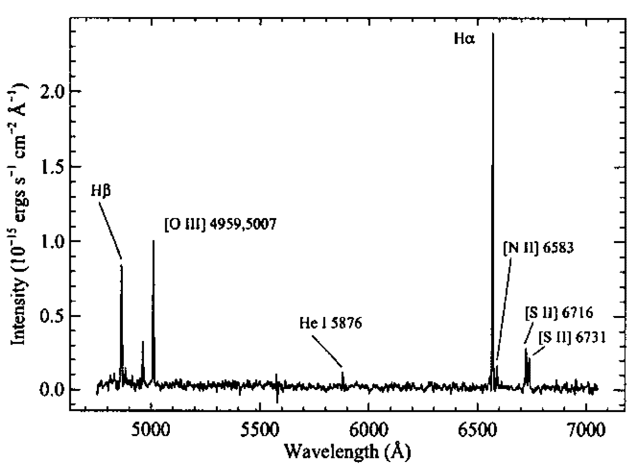

FIG. 5.—Spectrum of a typical NGC 5204 H II region, namely, the bright H II region south of NGC 5204 SNR No. 1.

will be better able to determine if NGC 5585 SNR No. 1 is indeed a strong emitter of X-rays.

3.3. *NGC 6946*

We identified 27 SNRs in this Scd galaxy (Table 8). The SNRs have [S II]/Hα ratios of 0.46–1.14. Most of the SNRs detected in NGC 6946 appear nearly stellar. Finding charts for the NGC 6946 SNRs are shown in Figure 8, with spectra of five of the SNRs shown in Figure 9. (The feature near 6300 Å in SNR No. 18 is poorly subtracted night-sky emission.) Relative line intensities measured in these spectra are given in Table 9. A typical H II region spectrum from NGC 6946 is shown in Figure 10.

NGC 6946 SNR No. 16 was observed by Blair & Fesen (1994), who presented both spectra and interference filter image data of this unusually bright SNR. The SNR appeared marginally resolved in their images, as it does in ours. A comparison between our estimated diameter and Hα intensity for this object and Blair & Fesen's estimates is shown in Table 14. Our corrected Hα intensity is identical to the value quoted by Blair & Fesen. Our [S II] image intensity value, derived completely independently of any spectral data from Blair & Fesen, is also nearly identical to their image and spectral [S II] intensity values. Our diameter estimate of 20 pc for SNR No. 16 is close to the 27 pc (using $R = 5.5$ Mpc) estimate of Blair & Fesen, but we suspect that their value is more accurate, given the higher resolution of their images.

Blair & Fesen (1994) also identified a faint nebula ~25″ northwest of their SNR as a possible remnant (see their Fig. 1). We have identified this object as SNR No. 15. One can also see, in Figure 1 of Blair & Fesen, the object we have identified as NGC 6946 SNR No. 17; it is the faint bit of emission just to the southwest of the "[S II]" label in their Figure 1*b*.

Blair & Fesen (1994) noticed a discrepancy between the Hα flux they measured for SNR No. 16 and that quoted by Bonnarel, Boulesteix, & Marcelin (1986) for the same object, in that Blair & Fesen's Hα flux was about a factor of 6 smaller. We found the same discrepancy for SNR No. 16. Choosing about six other objects measured by Bonnarel et al. (1986) that we also measured, we found our Hα intensities were smaller than theirs by factors ranging from ~2 to 10.

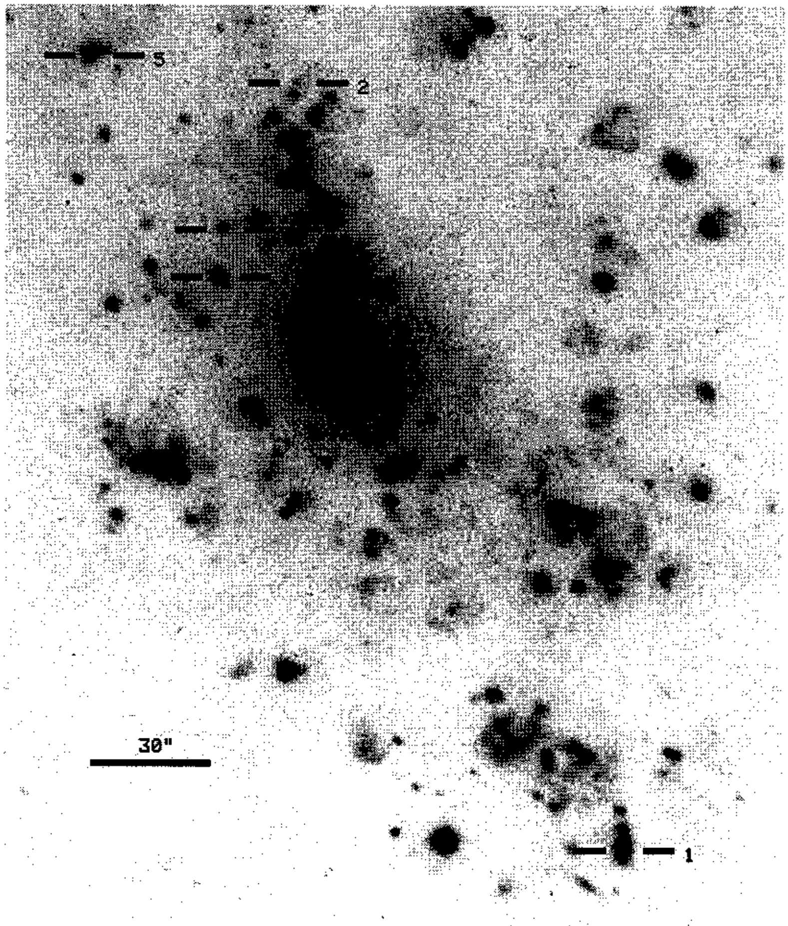

FIG. 6.—Hα image of the central region of NGC 5585, with SNRs marked

3.4. *M81*

In this Sab galaxy, we identified a total of 41 SNRs with [S II]/Hα ratios ranging from 0.45 to 1.64 and estimated diameters of 10–130 parsecs (Table 10). The five fields which constitute our M81 image data are marked on a Digitized Sky Survey[3] image of M81 in Figure 11. Hα image finding charts of the SNRs detected in M81 are shown in Figures 12–16. In the west field of M81, we have marked SN 1993J (Finn et al. 1995), which was still quite bright at the time this image was taken (1994 March 7). Spectra of four M81 SNRs are presented in Figure 17. Line intensities relative to Hα for these spectra, as well as the air masses at observation, the E_{B-V} values, and the Hα intensities, are given in Table 11. A typical H II region spectrum from M81 is shown in Figure 18.

Petit, Sivan, & Karachentsev (1988) published a photographic survey of M81 H II regions. Five of their H II regions also were measured by us, four of which we found to be SNRs (see Table 14 below). The agreement between Hα intensities measured by us and Petit et al. is reasonable, considering that their data were photographic.

In their *Einstein* HRI image of M81, Fabbiano (1988) detected an X-ray source, X-6, in the galaxy's southwest arm at R.A. (J2000) = $9^h55^m32^s.74$, decl. (J2000) = $+69°00'33''.1$. This HRI position is uncertain by ~4". They measured an X-ray luminosity for X-6 of $L_X = 1.5 \times 10^{39}$ ergs s^{-1} (in the 0.2–4.0 keV channel; M81 distance = 3.6 Mpc). Fabbiano believed that such a high X-ray luminosity (along with a marginal detection of possible variability) indicated that X-6 was probably an X-ray binary. We detected M81 SNR No. 22 less than 1" from the position of X-6, which also is nearly coincident with a discrete radio source visible in a VLA 20 cm map of M81 by Bash & Kaufman (1986). Therefore, despite the high X-ray luminosity observed, the optical counterpart to X-6 may be our SNR No. 22.

3.5. *M101*

Our search of M101 yielded 93 SNRs (see Table 12) with [S II]/Hα ratios of 0.45–1.59 and estimated diameters of less than 2 to greater than 300 pc. The five fields observed in M101 are shown on a Digitized Sky Survey image in Figure 19. SNRs detected in M101 are shown on the finding charts in Figures 20–24, with spectra of 11 SNRs shown in Figure

[3] Based on photographic data of the National Geographic Society/Palomar Observatory Sky Survey (NGS-POSS) obtained using the Oschin Telescope on Palomar Mountain. The NGS-POSS was funded by a grant from the National Geographic Society to the California Institute of Technology. The plates were processed into the present compressed digital form with their permission. The Digitized Sky Survey was produced at the Space Telescope Science Institute under US Government grant NAG W-2166.

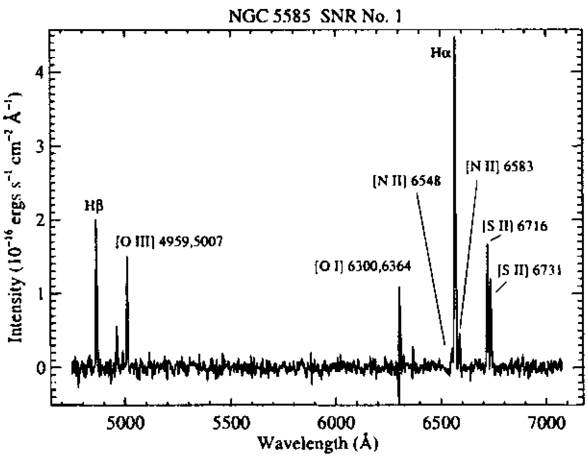

FIG. 7a

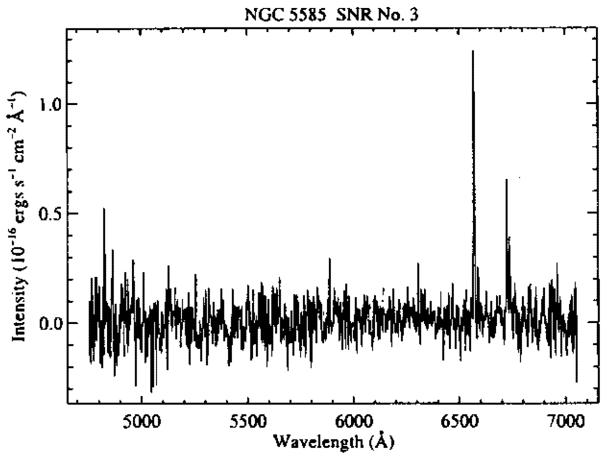

FIG. 7b

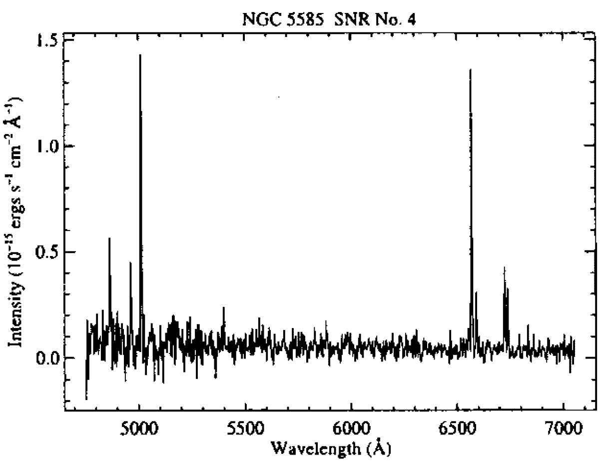

FIG. 7c

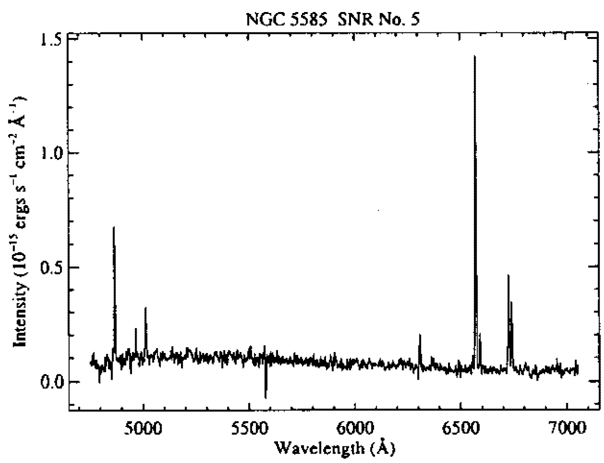

FIG. 7d

FIG. 7.—NGC 5585 SNR spectra

TABLE 13

RELATIVE LINE INTENSITIES FOR M101 SNRs WITH SPECTRA

LINE	SNR No. 17	19	21	24	33	38	44	50	71	76	83
Hβ λ4861	100	100	100	100	100	...	100	100	100	100	100
[O III] λ4959	28	38	185	103	69	...	...	26	14	32	35
[O III] λ5007	127	173	532	276	194	...	35	188	26	75	177
[N I] λ5200	...	...	...	...	...	...	...	...	...	...	...
He I λ5876	...	...	...	...	...	...	...	...	...	...	...
[O I] λ6300	39	52	76	100	...	54	21	50	32	52	30
[O I] λ6364	...	33	21	49	...	...	7	...	9	20	11
[N II] λ6548	61	60	57	99	72	...	41	117	46	26	74
Hα λ6563	300	300	300	300	300	300	300	300	300	300	300
[N II] λ6583	163	192	186	208	215	...	...	358	127	78	180
[S II] λ6716	162	175	163	167	124	119	93	102	131	113	153
[S II] λ6731	110	116	107	151	89	88	65	139	96	72	74
SNR Parameters:											
sec z	1.23	1.15	1.15	1.33	1.54	1.25	1.18	1.12	1.18	1.28	1.09
E_{B-V}	0.45	0.55	0.59	0.60	0.56	0.00[a]	0.51	0.35	0.35	0.04	0.42
I(Hα)[b]	6.8E−15	2.1E−14	1.9E−14	7.2E−15	8.0E−15	3.3E−15	2.5E−14	2.5E−15	2.0E−14	6.3E−15	2.8E−14

[a] Burstein & Heiles 1978.
[b] From photometry, given in units of ergs cm^{-2} s^{-1}.

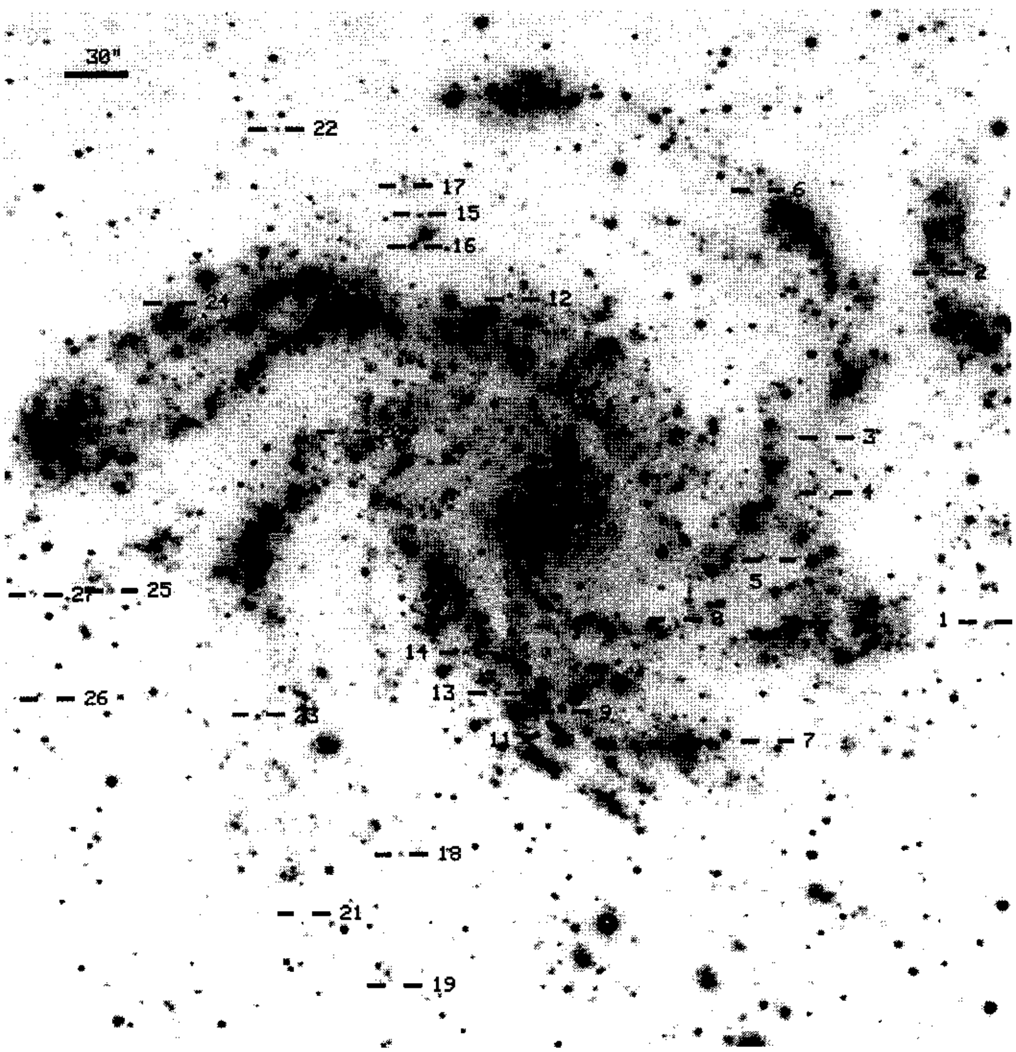

FIG. 8a

FIG. 8.—(a) Full-frame Hα image of NGC 6946 with SNRs marked. (b–e) Detailed finding charts of the SNRs found in the northeast, southeast, southwest, and northwest regions of NGC 6946. (f) Central region of NGC 6946, showing the SNR detected near the galaxy's center.

25. Line intensities of these spectra, relative to Hα, are listed in Table 13. A spectrum of a typical H II region from M101 is shown in Figure 26. Note that SNR No. 38, unlike most of the other SNRs in M101 for which we obtained spectra, showed no measurable [N II] λλ6548, 6583 lines.

With an estimated diameter of 200 pc, SNR No. 83 is one of the largest SNRs we found in this galaxy. As seen in the finding charts (Figs. 21*d* and 21*e*), this remnant has a shell-like morphology, with the shell made up of knots of bright emission. SNR No. 83 is clearly a remnant, with a spectrum indicating [S II]/Hα = 0.76. An even larger remnant, SNR No. 10, has a filled morphology and axes of 350 × 250 pc. Although its total Hα intensity is rather high (1.3×10^{-14} ergs cm^{-2} s^{-1}), its surface brightness is low because of its immense size, and it thus appears on the finding chart in Figure 22*d* as a faint object. Two faint stars (one of which is visible in Figs. 22*a* and 22*d*) are seen in projection on SNR No. 10 in our continuum image data; their physical association with this remnant is unclear. A single bright star also is seen in projection on SNR No. 87 in our continuum image data (at the same location as the westernmost bright feature of the remnant visible in Fig. 23), and its physical association with the remnant also is unclear.

Williams & Chu (1995) examined *ROSAT* PSPC and HRI data of M101. They found a source, their S7, located at R.A. (J2000) = $14^h03^m21^s.0$, decl. (J2000) = +54°19′39″ (±4″) and superposed on a central region of diffuse X-ray emission. Unfortunately, the data did not contain enough information to allow Williams & Chu to speculate as to what type of object S7 might be. We detected the relatively bright, unresolved M101 SNR No. 54 only ∼3″ from the reported position of S7, making it a possible optical counterpart of this X-ray source.

4. ANALYSIS OF DETECTED SNRS

4.1. *Selection Effects, Biases, and Completeness*

Because our SNR samples are neither complete nor uniform, one cannot perform a thorough quantitative analysis of biases and selection effects. However, to under-

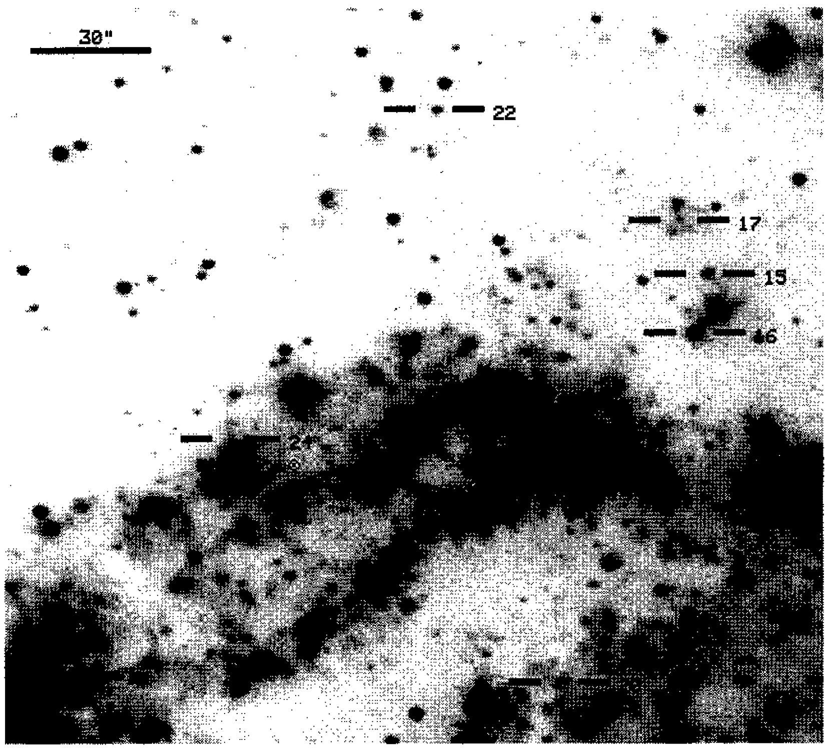

FIG. 8*b*

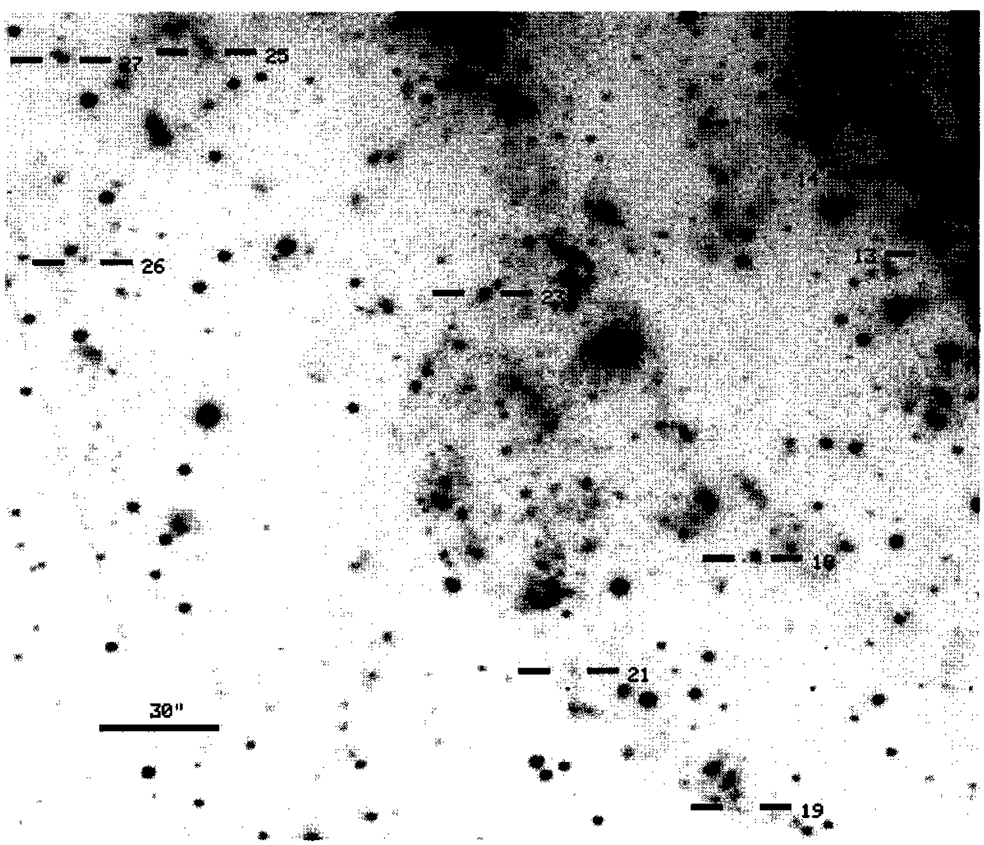

FIG. 8*c*

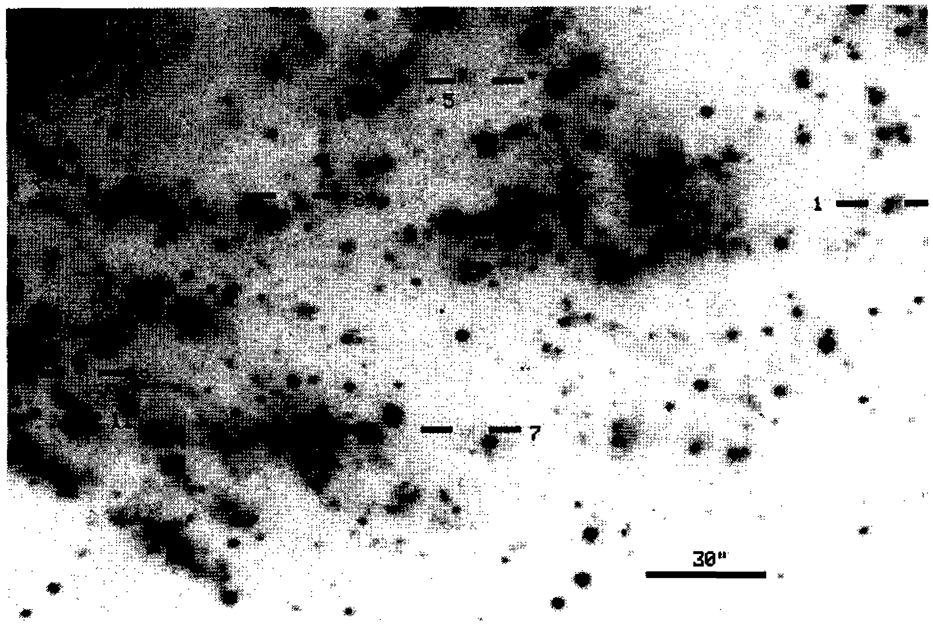

FIG. 8*d*

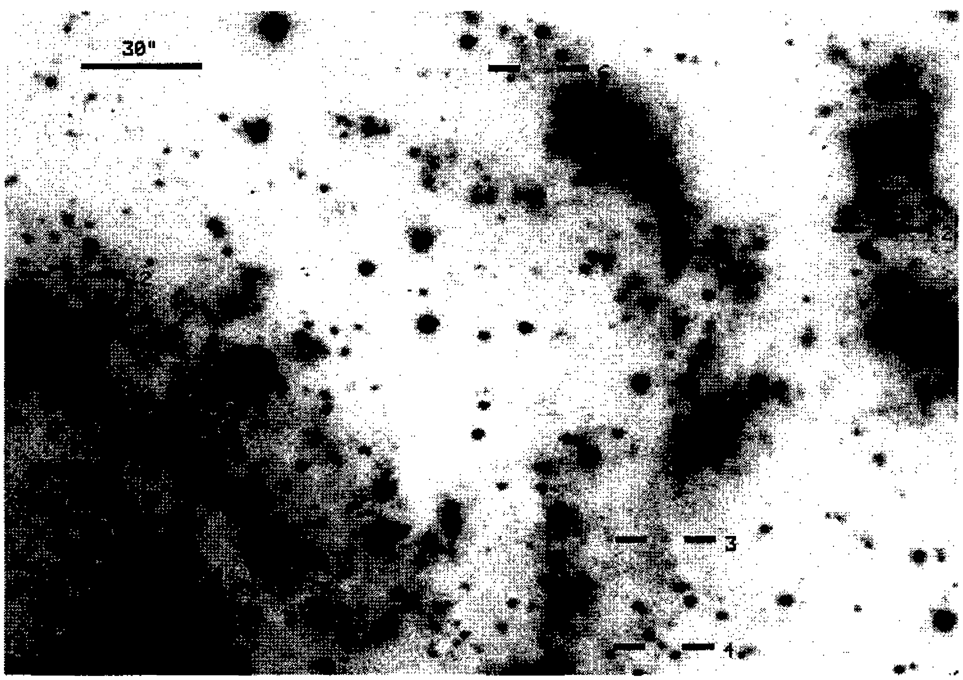

FIG. 8*e*

stand the limits of our SNR samples in any further analysis, we qualitatively discuss below source confusion, completeness limits, and SNR identification criterion biases.

A bias regarding the diameters of detected SNRs versus their galactocentric distance could exist because of the increased ease of finding more large SNRs in the outer or interarm regions of a galaxy, where the surface density of H II regions is lower. While there appears to be a bias that favors the detection of larger SNRs in the interarm regions of M81 and M101, no such bias was found in NGC 6946. Similar to SNR confusion with bright H II regions is the possibility that faint SNRs might be easier to detect at large galactocentric distances where the background continuum light of a galaxy is weak. However, except for NGC 6946 and M81, which have bright central regions virtually devoid of detected SNRs, no significant trends in SNR Hα intensity

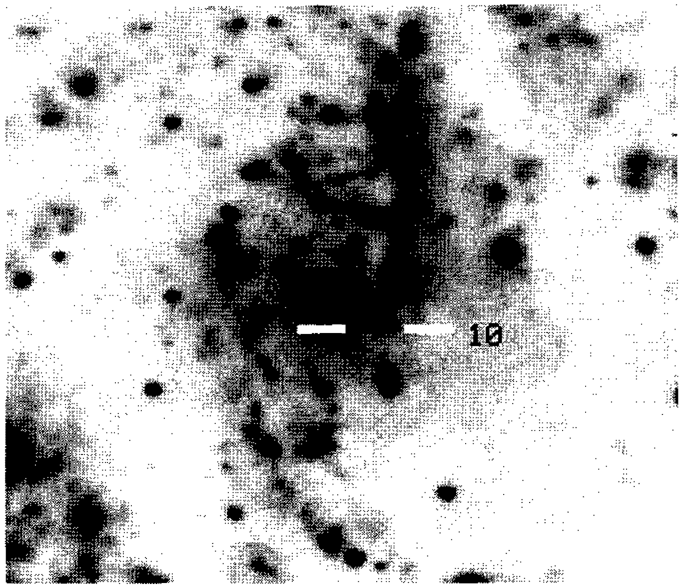

FIG. 8*f*

with galactocentric distance were seen in any of the sample galaxies. We note that no such effect was detected in either M33 (Smith 1991) or NGC 2403 (Matonick et al. 1997).

Evolved SNRs increase in size and decrease in brightness as they age, and at any given time there will be more old SNRs than young. Thus, if a sample of SNRs was complete, one would expect to see the number of SNRs increase with increasing size and decreasing brightness. Completeness limits in SNR samples can therefore be estimated by noting at what intensity and diameter the number of detected remnants begins to decrease (Green 1991; Smith 1991; Gordon 1994). Histograms of the log of Hα intensity for the SNRs detected in NGC 6946, M81, and M101 are shown in Figure 27. The estimated value of Hα intensity below which each SNR sample is significantly incomplete is marked on the peak of each histogram. The incompleteness estimate for NGC 6946 is $I(\mathrm{H}\alpha) \lesssim 2.4 \times 10^{-15}$ ergs cm^{-2} s^{-1}, for M81 it is $I(\mathrm{H}\alpha) \lesssim 2.0 \times 10^{-15}$ ergs cm^{-2} s^{-1}, and for M101 it is $I(\mathrm{H}\alpha) \lesssim 3.2 \times 10^{-15}$ ergs cm^{-2} s^{-1}. Note that the detection limit for all the samples is $I(\mathrm{H}\alpha) \sim 5 \times 10^{-16}$ ergs cm^{-2} s^{-1}. Histograms of SNR diameter are shown in Figure 28 for NGC 6946, M81, and M101. The peak of each histogram is labeled, and each SNR sample appears to be incomplete for $D \gtrsim 30$ pc.

TABLE 14

COMPARISONS WITH PREVIOUS OBSERVATIONS

Object Name	D[a] (pc)	$I(\mathrm{H}\alpha)$[b] (ergs cm^{-2} s^{-1})	[S II]/Hα	References
		NGC 6946		
SNR No. 16......	20	7.1×10^{-14}	0.85[c]	1
....	27	7.1×10^{-14}	0.85	2
		M81		
SNR No. 15......	20	3.4×10^{-15}	0.63	1
No. 180...........	...	7.9×10^{-15}	...	3
SNR No. 17......	30	8.6×10^{-15}	1.22	1
No. 189...........	...	6.5×10^{-15}	...	3
SNR No. 18......	130	3.6×10^{-14}	0.70	1
No. 199...........	...	5.4×10^{-14}	...	3
SNR No. 21......	20	1.2×10^{-15}	1.17	1
No. 229...........	...	2.4×10^{-15}	...	3

[a] Calculated using galaxy distance estimates from Table 2.

[b] Corrected for interstellar extinction using the E_{B-V} values from Table 2.

[c] Blair & Fesen 1994.

REFERENCES.—(1) This work; (2) Blair & Fesen 1994; (3) Petit et al. 1988.

Figure 29 shows log $I(\mathrm{H}\alpha)$ versus diameter (converted from parsecs to arcseconds) for detected SNRs in all the sample galaxies combined (including the NGC 2403 SNRs from Matonick et al. 1997). This figure shows that the total sample is biased against detecting large, faint SNRs. The area below the dashed line marks the approximate region of incompleteness. A similar result was obtained in the M31 SNR sample of Braun & Walterbos (1993).

There are certain emission nebulae that have [S II]/Hα ≥ 0.45 but that are not SNRs, namely stellar wind–shocked nebulae and diffuse ionized gas. As discussed by Hunter (1994) and Walterbos & Braun (1994), most stellar wind–shocked nebulae and diffuse ionized gas objects have [S II]/Hα < 0.6 and size greater than 100 pc. To check our SNR samples for possible contamination by such objects, in Figure 30 we plot [S II]/Hα versus diameter for the detected SNRs in all the galaxy samples combined. The plot is marked with two dashed lines to separate out the 15 objects with [S II]/Hα < 0.6 and diameter greater than 100 pc. These ambiguous objects constitute ~14% of the NGC 2403 SNR sample (Matonick et al. 1997) and ~11% of the

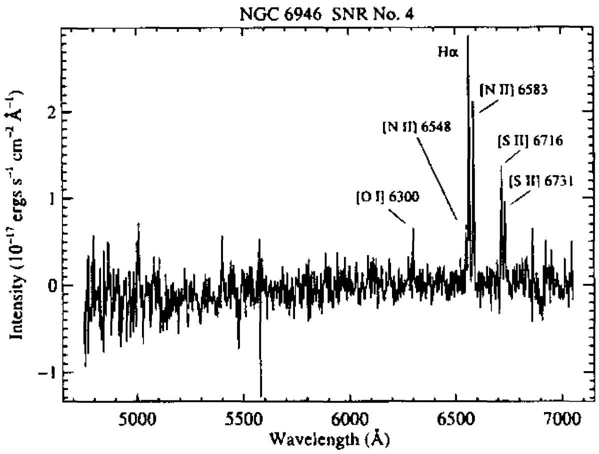

FIG. 9*a*

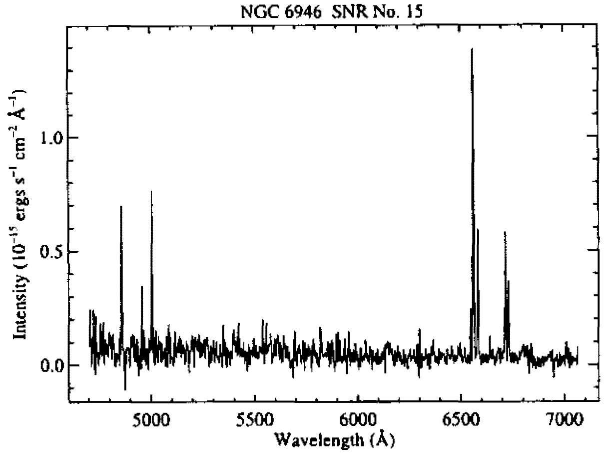

FIG. 9*b*

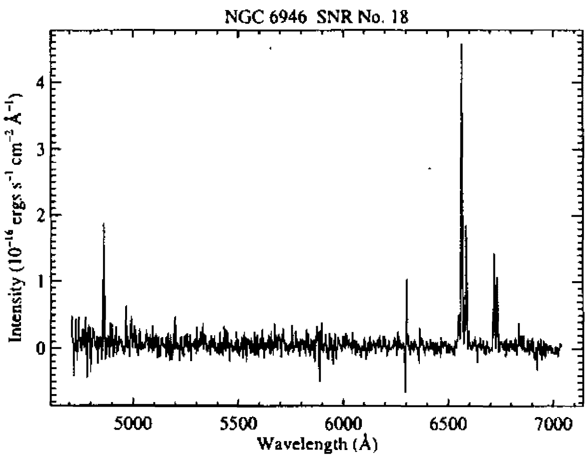

FIG. 9*c*

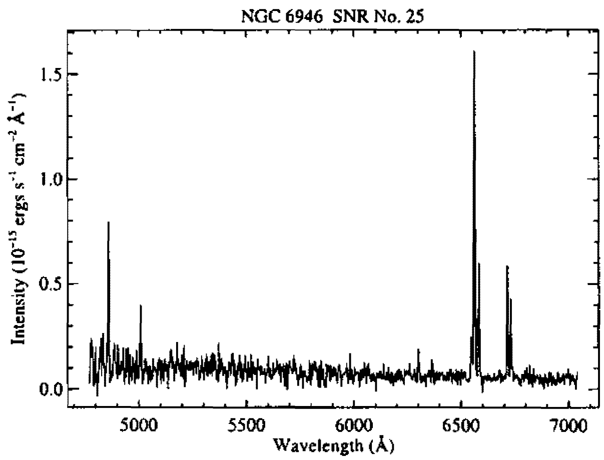

FIG. 9*d*

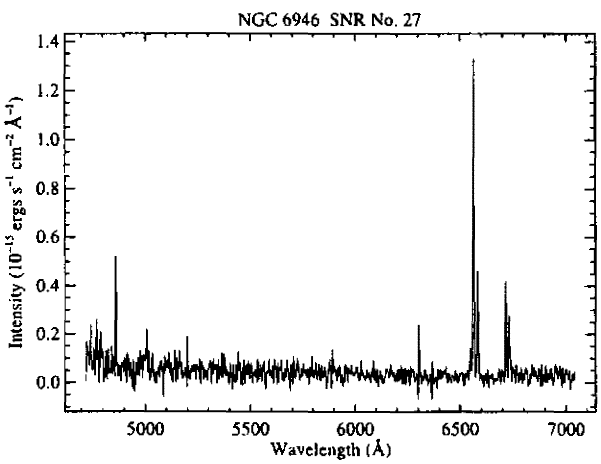

FIG. 9*e*

FIG. 9.—NGC 6946 SNR spectra

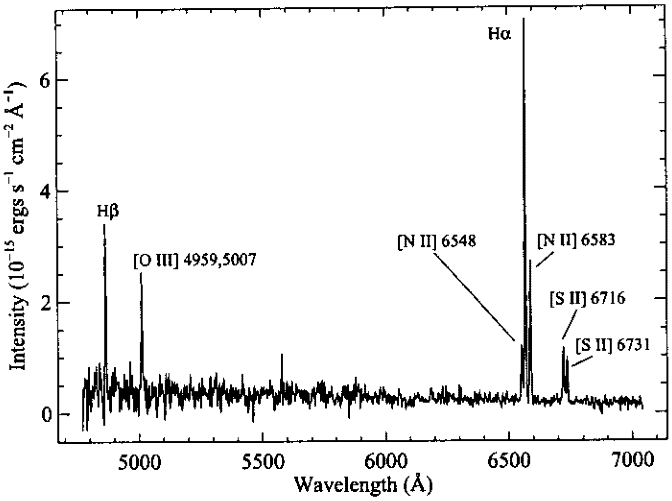

FIG. 10.—A typical NGC 6946 H II region spectrum, from the middle of three small H II regions about 15″ southwest of NGC 6946 SNR No. 5.

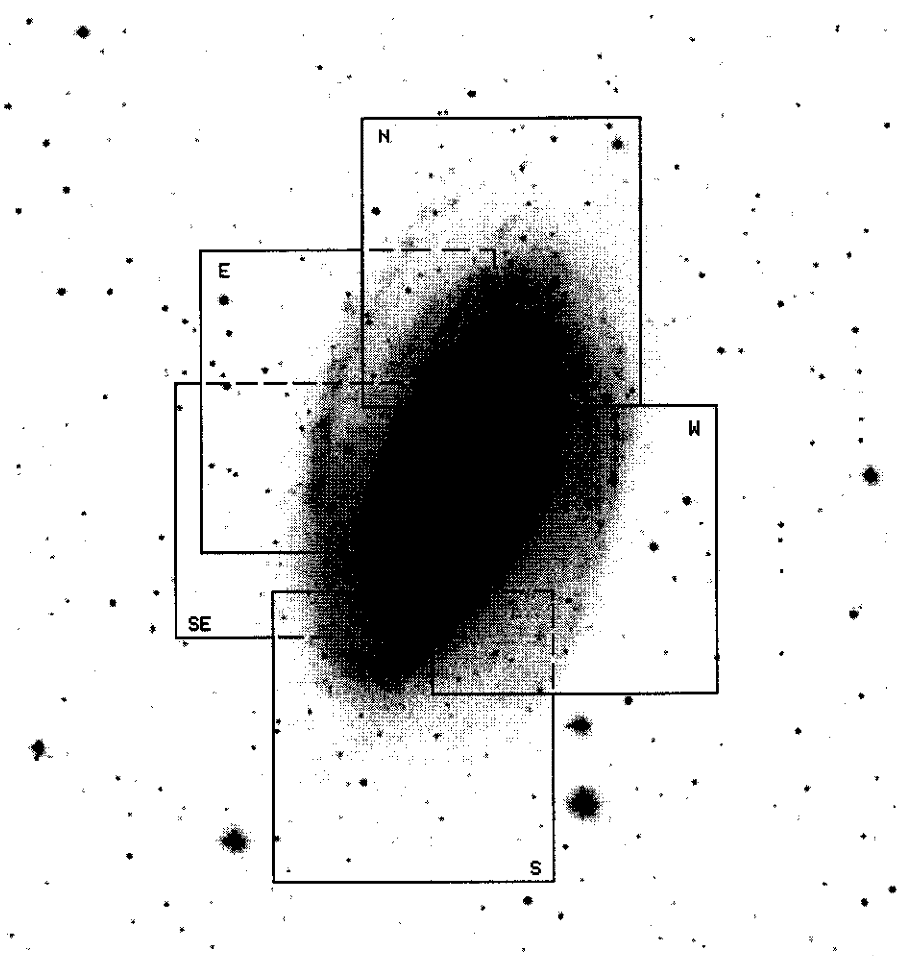

FIG. 11.—Digitized Sky Survey E image of M81 showing the fields observed

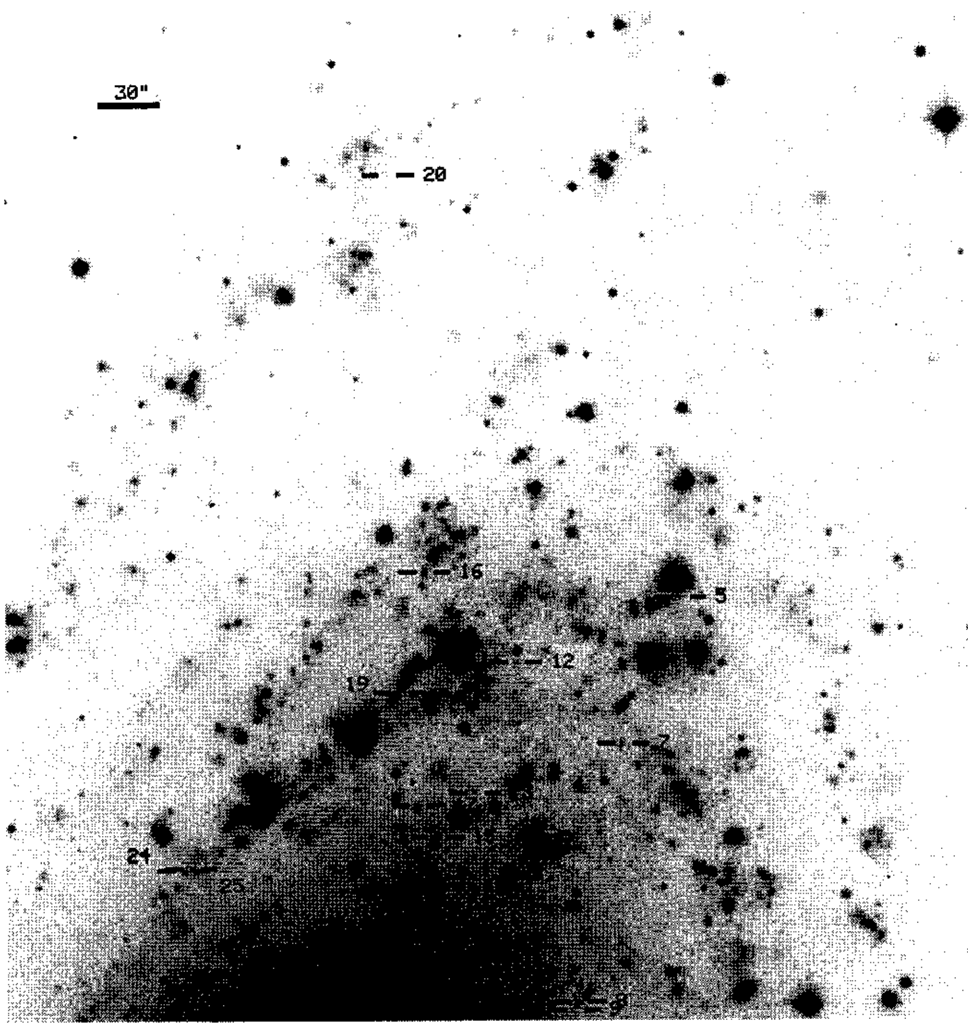

Fig. 12*a*

Fig. 12.—(*a*) Full-frame Hα image of the north field of M81 with SNRs marked. (*b*, *c*) Detailed finding charts of the SNRs detected in two sections of this field.

M101 sample, but only ~7% of our total SNR sample. This estimate of contamination from non-SNR objects agrees with that of Braun & Walterbos (1993), who, in their M31 SNR survey, believed that a realistic estimate of contamination from stellar wind–shocked nebulae was about 10%. However, we also agree with Blair & Long (1997), who found some diffuse ionized gas in NGC 7793 with [S II]/Hα > 0.6, as to the importance of using the discreteness of objects, along with their [S II]/Hα ratios, when identifying SNRs in surveys like ours. This additional criterion is necessary to avoid confusing SNRs with diffuse ionized gas. Note that no correlation was found between the morphologies and [S II]/Hα values of our 15 objects with [S II]/Hα < 0.6 and diameter greater than 100 pc or, for that matter, between the morphologies and the [S II]/Hα ratios of the other remnants in our samples.

Blair & Long (1997) noted the lack of a pronounced gap in [S II]/Hα values between the SNRs and H II regions they observed in NGC 300 and NGC 7793. This result is similar to that found by Walterbos & Braun (1992) in M31, where they examined all the emission nebulae in their fields and found that the [S II]/Hα distribution is not bimodal. In our SNR samples, we likewise find a sudden absence of emission nebulae below [S II]/Hα ≈ 0.4–0.5. In fact, the objects we measured and rejected as possible SNRs had [S II]/Hα ratios ranging from 0.13 to 0.44, although it must be remembered that our samples are biased because we selected objects from our difference images, which highlighted [S II]–bright nebulae.

Braun & Walterbos (1993) estimate that about half of all SNs are massive (Type II or Ib/c, as opposed to Type Ia), and of these, about half go off in associations and leave no detectable remnant. If we assume that remnants of Type Ia SNs are not as easily detectable as those of Type II or Ib/c, because of a possible tendency of Type Ia SNs to occur in the less gas-rich regions of a galaxy, only ~25% of all SN events may leave readily detectable optical remnants. Therefore, we obtain a crude estimate that there could be 4 times more SNRs in each of the program galaxies than were detected in this survey, i.e., ~10 SNRs in NGC 5204, ~20 in NGC 5585, ~100 in NGC 6946, ~160 in M81, and ~370 in M101. If the optically observable lifetime of a SNR

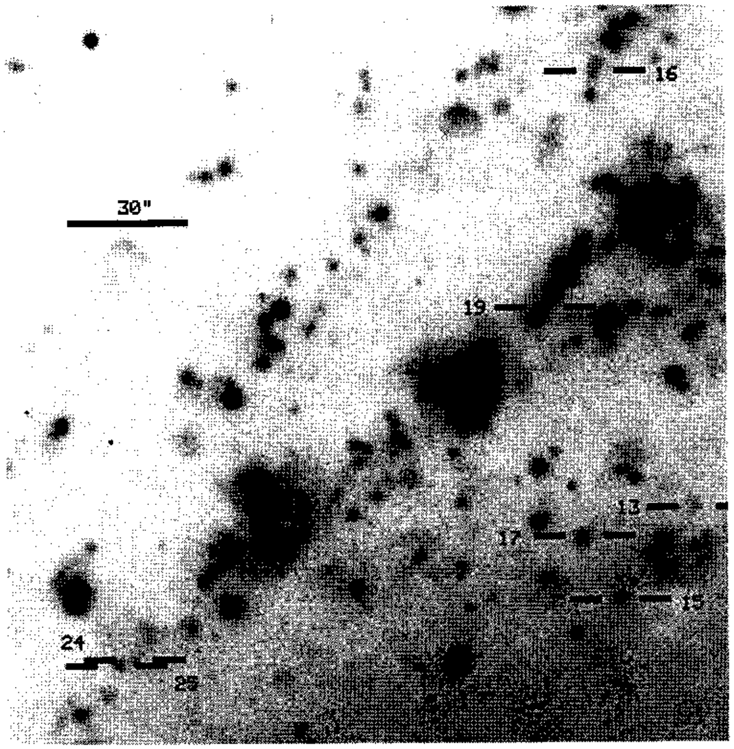

FIG. 12*b*

is ~20,000 years (Braun, Goss, & Lyne 1989), we obtain a rough estimate of the SN rate in each of the galaxies: 1 SN per 2000 yr for NGC 5204, per 1000 yr for NGC 5585, per 200 yr for NGC 6946, per 130 yr for M81, and per 50 yr for M101. Note that the SN rate estimates in M81 and M101 obtained here are similar to the estimates from historical SNs within the observed galaxy fields (1 SN per 100 yrs for M81, 1 SN per 50 yrs for M101: Barbon et al. 1989, including SN 1993J in M81).

4.2. *Spatial Distributions of SNRs*

Some idea of the stellar populations that give rise to SNRs can be obtained by examining the distributions of SNRs relative to known star-forming regions such as H II regions, molecular clouds, and spiral arms. Massive Population I stars (which explode as Type II or Type Ib/c SNs) would tend to be found near such regions, while more evolved, lower mass Population II stars (which explode as Type Ia SNs) are expected to be distributed in a more random manner across the plane of a galaxy's disk. Previous work on the distributions of SNs and SNRs in galaxies includes Maza & van den Bergh (1976), Huang (1987), Chu & Kennicutt (1988b), Cohen et al. (1988), Forest, Spenny, & Johnson (1988), van den Bergh (1988), Bartunov, Makarova, & Tsvetkov (1992), Van Dyk (1992), Bartunov, Tsvetkov, & Filimonova (1994), and van den Bergh (1997).

Below we examine the distributions of our detected SNRs (including those in NGC 2403) relative to spiral arms, H II regions, and molecular clouds, as well as the radial distributions of SNR surface density. Although historical SNs occurred within the observed galaxy fields, we chose not to include them in our analysis of the spatial distributions of SNRs in order that our conclusions would be based solely on the SNRs found by our methods.

4.2.1. *SNR Distributions Relative to Spiral Arms*

Spiral arm tracers are discussed in Kaufman et al. (1989) and include both young and old stars. We used our continuum images that best showed the spiral arm structure and traced the spiral arms along the peak surface brightness in each discernible arm. Three of our sample galaxies (NGC 6946, M81, and M101) had spiral arms prominent enough to allow us to measure their positions in this way. The spiral arm patterns observed for these galaxies are shown in Figure 31, plotted as they appear on the sky, along with the detected SNRs. (A few overlapping arms and small gaps appear in the plotted arms of M81 and M101; these negligible discrepancies are the result of imperfectly measuring the overlapping spiral arms on different galaxy field images.) To get some idea of the number of SNRs detected "within" spiral arms, we estimated the most common value of spiral arm width in each of the galaxies (~25").

Using the values of inclination and position angle given in Table 2, we deprojected the coordinates of the SNRs and spiral arms in NGC 6946, M81 and M101 to face-on (Fig. 32). We then measured the distance between each SNR and its nearest spiral arm point. Following the convention used by Maza & van den Bergh (1976) and Bartunov et al. (1994), the distance from a SNR to its nearest spiral arm point is negative if the SNR is "behind" the spiral arm (i.e., between the spiral arm and the galaxy's center). The distributions of our detected SNRs in NGC 6946, M81, and M101, relative to the spiral arms, are shown in Figure 33.

In order to check for an association between our detected

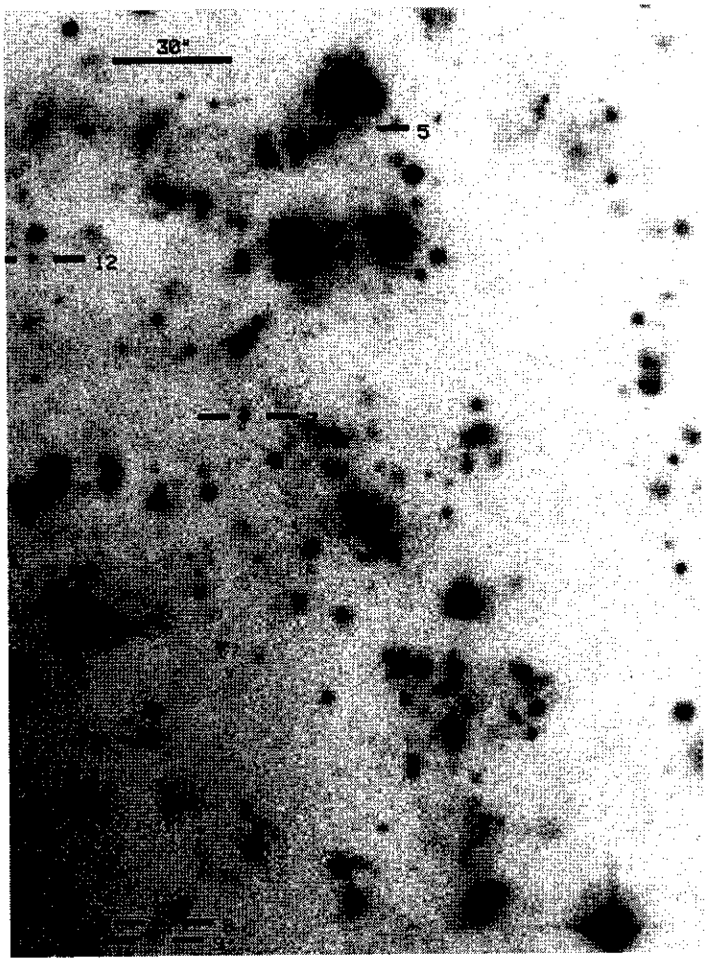

FIG. 12c

SNRs and the spiral arms, in each galaxy we compared the distribution of detected SNRs with a random distribution of 10,000 simulated SNRs placed within galactocentric radial limits exhibiting emission nebulae (either H II regions or SNRs). Specifically, a random distribution was obtained by converting positions of SNRs and H II regions into (r, ϕ) coordinates within the plane of each galaxy. At a random value of ϕ, a simulated SNR was placed at a random value of r limited by the minimum and maximum r values of the observed nebulae within a 20° section of the plane of the galaxy containing the fixed ϕ. This method prevented us from placing simulated SNRs outside our observed galaxy fields or in regions where no emission nebulae were detected. The distance from each simulated SNR to its nearest spiral arm was measured, just as was done for the detected SNRs. The resulting distributions of simulated SNRs relative to the spiral arms in NGC 6946, M81, and M101 are plotted as solid curves in Figure 33 and are shown normalized to the number of detected SNRs in each galaxy.

For each of the galaxies, we have two distributions of SNR distance to the nearest spiral arm: one for the detected SNRs, and another for the randomly distributed, simulated SNRs. Because the data comprising the two distributions in each galaxy are continuous and a function of a single variable (the distance to the nearest spiral arm), one method for statistically comparing the two distributions is the Kolmogorov-Smirnov (K-S) test (Press et al. 1989), which gives the probability that two data sets were drawn from the same parent distribution. A small probability ($\lesssim 0.05$) tells us that the two distributions are significantly different. If the two distributions in a given galaxy are *different*, it would mean that our detected SNRs in that galaxy are *not* distributed randomly, but are probably associated with the spiral arms.

Running K-S tests on the three pairs of distributions shown in Figure 33, we obtain the probabilities listed in Table 15. The tests indicate that the SNRs detected in M81 and M101 probably are associated with the spiral arms in those galaxies, whereas the K-S probability obtained for NGC 6946 is ambiguous. The probable association between our detected SNRs and the spiral arms in M81 and M101 agrees with the results obtained by Maza & van den Bergh (1976) and Bartunov et al. (1994) for historical SNs in spiral galaxies and suggests that the progenitors of the M81 and M101 SNRs were mostly massive stars that exploded as Type II or Ib/c SNs.

4.2.2. *SNR Distributions Relative to* H II *Regions*

In prior studies of SNs positions relative to H II regions (e.g., Van Dyk 1992), the distance from a SN to its nearest H II region was found by using the radius of each H II

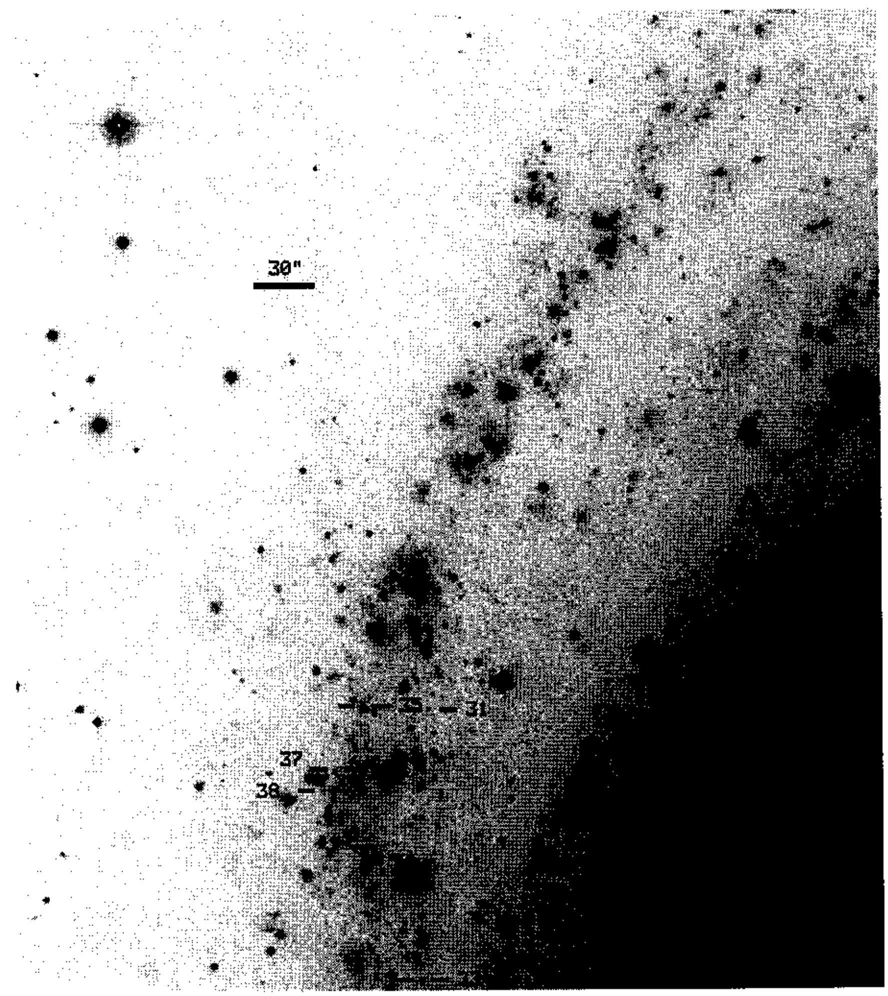

FIG. 13a

FIG. 13.—(a) Full-frame Hα image of the east field of M81, with SNRs marked. (b) Detailed finding chart of the SNRs detected in a section of this field.

region, which required defining an H II region edge. Because the edge of an H II region is difficult to determine consistently from images and because we wanted to take into account the spatial extent of the many large, resolved H II regions in each galaxy, we used IRAF to mark the bright points of each H II region. Large, resolved H II regions are marked by several points; an unresolved H II region is marked by a single point. Plots of the marked H II region points as they appear on the sky, along with the detected SNRs, are shown for each of our sample galaxies in Figure 34. Distributions of detected SNRs relative to H II regions are shown in Figure 35 for NGC 6946, NGC 2403, M81, and M101. (Because so few SNRs were detected in NGC 5204 and NGC 5585, these galaxies are not included in this analysis.)

Distributions of the deprojected distances from 10,000 simulated SNRs to their nearest H II regions are shown in Figure 35, and again are normalized to the number of detected SNRs in each galaxy. Running K-S tests on each of these four pairs of distributions, we obtained the K-S probabilities shown in Table 15. These results show that the detected SNRs in M81 and M101 are clearly associated with the H II regions. The K-S probability for NGC 2403 is near the canonical cutoff value for indicating that two distributions are significantly different, but it is still low enough to suggest that the detected SNRs in this galaxy probably are associated with its H II regions. Finally, the relatively high K-S probability for NGC 6946 suggests that the SNRs detected in this galaxy probably are not closely associated with its H II regions.

Our deduced associations between SNRs and H II regions in NGC 2403, M81, and M101 agree with the results of Bartunov et al. (1994), Van Dyk (1992), and Huang (1987) for Type II and Ib/c historical SNs and with the results of Chu & Kennicutt (1988b), Forest et al. (1988), and van den Bergh (1988) for SNRs in the LMC, the majority of which they believed to be the result of Population I progenitors. Therefore, a significant fraction of the detected SNRs in these galaxies are probably the end products of core-collapse SNs (Types II and Ib/c). Although Bartunov et al. (1994) found that Type Ia SNs are not concentrated toward H II regions, the observed lack of an apparent association between detected SNRs and H II regions in NGC 6946 is, in itself, not enough for us to make any conclusions yet about

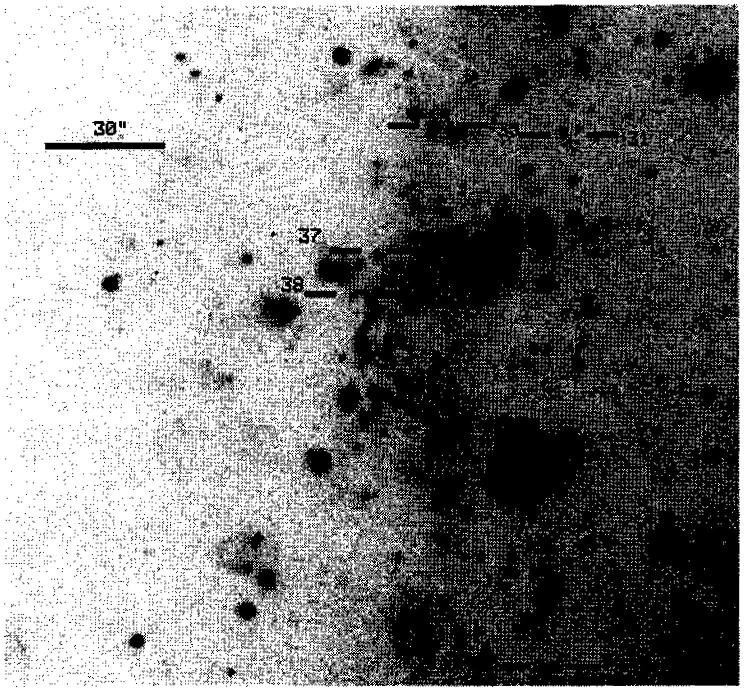

FIG. 13b

possible SNR progenitors in this galaxy. One possible reason for NGC 6946 behaving differently from the other galaxies, in comparing associations of SNRs with either H II regions or spiral arms, is that NGC 6946 has a foreground extinction a factor of 10 larger than the next most obscured galaxy. Such relatively high obscuration could have a dramatic effect on the ease of detecting remnants in this galaxy and therefore leave us with a distribution of SNRs different from those in the other galaxies.

4.2.3. *SNR Distributions Relative to Molecular Clouds*

Positions of molecular clouds in external galaxies can be obtained through radio observations of CO emission. The only complete map of CO emission currently available in the literature on our program galaxies is the one of M81 by Brouillet et al. (1991). Their observations covered nearly the whole face of M81, with a half-power beam width (HPBW) of 23" or 60". Using the coordinates given in Tables 1 and 3 of Brouillet et al. for the positions of where CO emission was detected (precessed to J2000 epoch coordinates), we plot, in Figure 36*a*, the CO emission regions as they appear on the sky, along with our detected SNRs. The diameters of the circles representing the CO emission are equal to the HPBWs at which the regions were observed.

In order to put the distance from a SNR to its nearest CO emission region on a uniform scale, we use a relative distance to the nearest CO emission region. A relative distance of less than 0 means that the SNR is located within the HPBW used to observe the region, and a relative distance of −1 means the SNR is centered on the region. The distribution of detected SNRs in M81 relative to the CO emission regions is shown in Figure 36*b*.

TABLE 15

KOLMOGOROV-SMIRNOV TEST RESULTS

Galaxy	P^a	Interpretation
		Spiral Arms
NGC 6946	0.15	Ambiguous; SNRs not strongly associated with spiral arms.
M81	0.001	SNRs probably associated with spiral arms.
M101	0.001	SNRs probably associated with spiral arms.
		H II Regions
NGC 6946	0.40	SNRs probably not associated with H II regions.
NGC 2403	0.05	SNRs probably associated with H II regions.
M81	3×10^{-7}	SNRs associated with H II regions.
M101	3×10^{-13}	SNRs associated with H II regions.
		Molecular clouds
M81	0.05	SNRs probably associated with molecular clouds.

[a] Probability that the distribution of detected SNRs in each galaxy, relative to the given objects, is from the same parent distribution as a random distribution of 10,000 simulated SNRs.

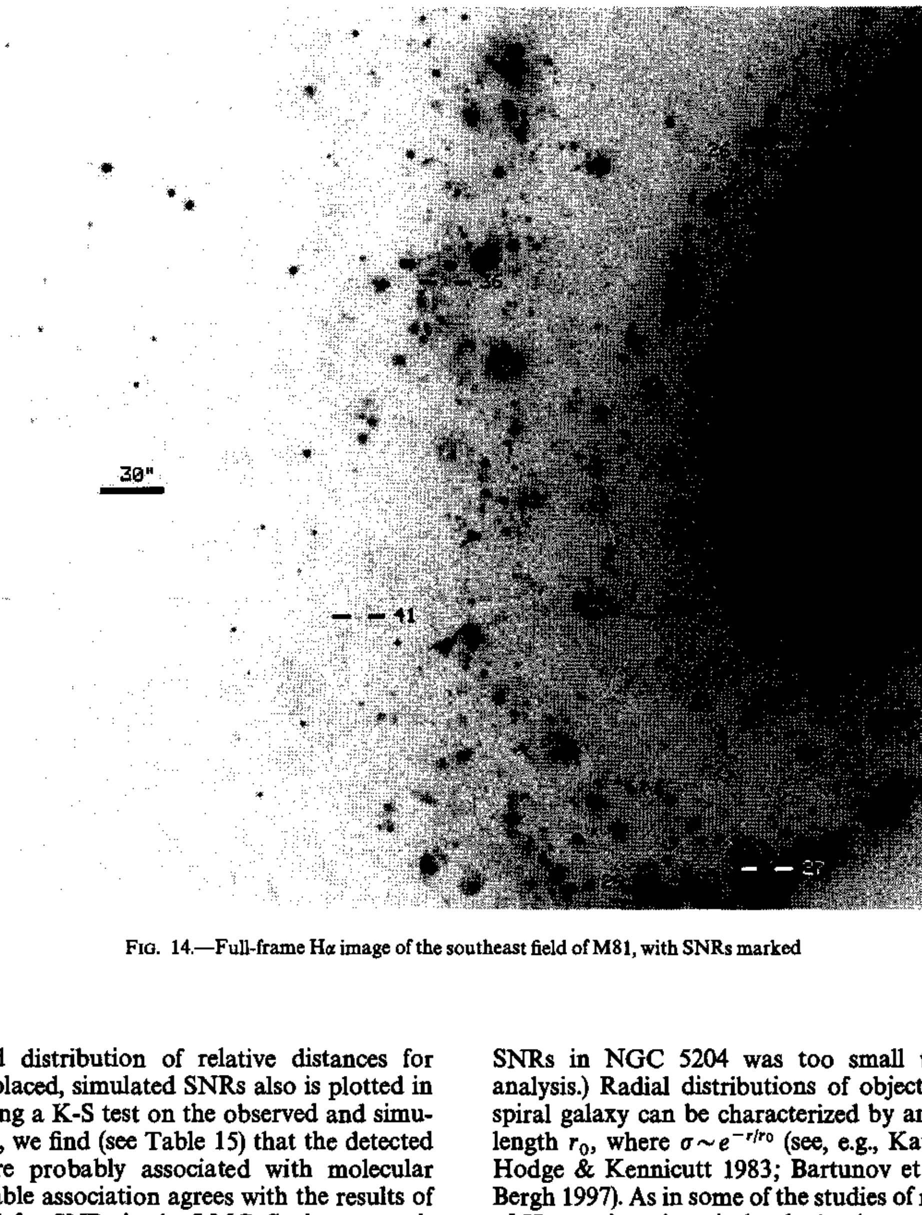

FIG. 14.—Full-frame Hα image of the southeast field of M81, with SNRs marked

The normalized distribution of relative distances for 10,000 randomly placed, simulated SNRs also is plotted in Figure 36*b*. Running a K-S test on the observed and simulated distributions, we find (see Table 15) that the detected SNRs in M81 are probably associated with molecular clouds. This probable association agrees with the results of Cohen et al. (1988) for SNRs in the LMC. Such an association may indicate that the M81 SNRs are the result of SNs with Population I progenitors exploding in or near the kinds of star-forming regions commonly associated with molecular clouds, which would probably indicate that the SNs were of Type II or Ib/c. Proper consideration of these results requires mentioning the fact that dusty giant molecular clouds may also be able to hide some SNRs.

4.2.4. *SNR Radial Distributions*

Gordon (1994) compared the radial distribution of SNRs detected in M33 with the radial distribution of intermediate-brightness H II regions and found that the surface density as a function of galactocentric distance shows a similar trend for both types of object. This similarity was thought to indicate an association between the detected SNRs and the H II regions, suggesting massive, Type II progenitors for the SNRs in M33. Radial distributions of normalized SNR surface density are shown in Figure 37 for five of our six sample galaxies. (The sample of SNRs in NGC 5204 was too small to include in this analysis.) Radial distributions of objects in the disk of a spiral galaxy can be characterized by an exponential scale length r_0, where $\sigma \sim e^{-r/r_0}$ (see, e.g., Kaufman et al. 1987; Hodge & Kennicutt 1983; Bartunov et al. 1992; van den Bergh 1997). As in some of the studies of radial distributions of H II regions in spiral galaxies (see, e.g., Hodge & Kennicutt 1983; Kaufman et al. 1987), we attempted to fit our radial distributions from only the main peak outward. Using a nonlinear least-squares fit to $\sigma \sim e^{-r/r_0}$, we obtained the exponential scale lengths and fits shown in Figure 37. A decreasing exponential fits some of the distributions better than others. Results for three of the galaxies are as follows:

NGC 6946.—This galaxy shows a noticeable gap in its SNR radial distribution at $\sim$1.5 kpc ($\sim$56″). This gap closely matches the one observed in the radial distribution of H II regions in NGC 6946 by Bonnarel et al. (1986). Likewise, the general shape of their radial distribution of H II regions resembles the one for our SNRs. This resemblance may indicate a closer relationship between SNRs and H II regions in that galaxy than was inferred from our K-S tests above. Examining Bonnarel et al.'s data, we were able to fit a decreasing exponential with $r_0 = 4.1 \pm 0.1$ kpc, which is close to our result of $r_0 = 4.4 \pm 0.1$ kpc for the radial distribution of SNRs.

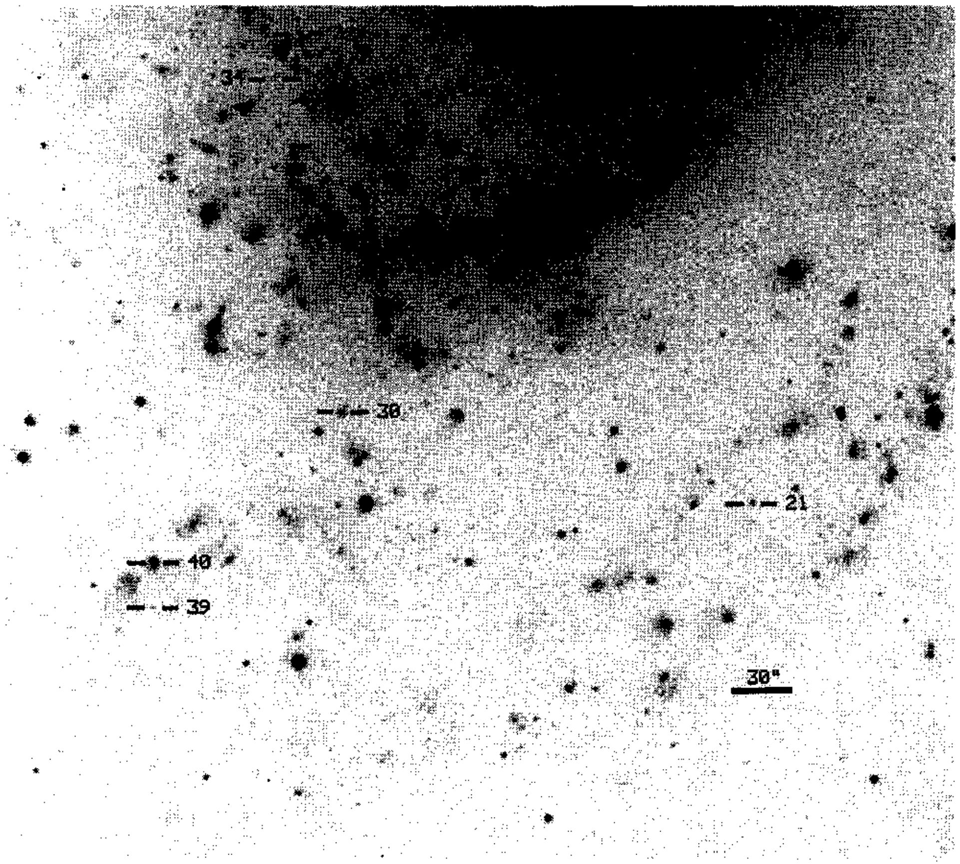

FIG. 15a

FIG. 15.—(a) Full-frame Hα image of the south field of M81 with SNRs marked. (b, c) Detailed finding charts of the SNRs detected in two sections of this field.

NGC 2403.—The steeply decreasing shape of the radial distribution of detected SNRs generally agrees with the distribution of H II regions given by Hodge & Kennicutt (1983), in agreement with our earlier conclusion that the SNRs and H II regions in this galaxy probably are associated.

M81.—The radial distribution of the SNR surface density clearly shows the central ~3 kpc region within which no SNRs (and virtually no emission nebulae) were detected. At least in overall shape, the radial distribution of SNRs in M81 bears a striking resemblance to the distribution of giant radio H II regions in M81 found by Kaufman et al. (1987). We obtained $r_0 = 2.2 \pm 0.1$ kpc for the detected SNRs, while, for the giant radio H II regions, Kaufman et al. found $r_0 = 1.6 \pm 0.4$ kpc, which differs only marginally from our SNR value. The close resemblance between our radial distribution of SNR surface density and that for giant radio H II regions provides further evidence to support our earlier conclusion that the detected SNRs in M81 are associated with that galaxy's H II regions.

In conclusion, the above analysis of spatial distributions of detected SNRs relative to spiral arms, H II regions, molecular clouds, and their radial distributions of surface density, shows that a significant fraction of the progenitors of the SNRs optically detected in NGC 2403, M81, and M101 are likely to have been Type II or Ib/c SNs.

4.3. *SNR Spectral Analysis*

We have used individual SNR spectra to calculate line ratios for ([O III] λλ4959, 5007)/Hβ, ([O I] λλ6300, 6364)/Hα, ([N II] λλ6548, 6583)/Hα, ([S II] λλ6716, 6731)/Hα, ([S II] λ6731)/Hα, and [S II] λ6716/λ6731. These line ratios are shown in Table 16, along with estimated remnant diameter and derived electron density. Some λ6716/λ6731 ratios in Table 16 had nonphysical measured values of greater than 1.46 and were set to the low-density limit; these ratios are footnoted. The electron density, N_e, in each SNR was calculated using measured λ6716/λ6731 ratios and the Space Telescope Science Data Analysis System task "nebular.temden," which is based on the five-level atom approximation of De Robertis, Dufour, & Hunt (1987). For consistency with previous work, we took the low-density limit to correspond to $N_e < 10\ \mathrm{cm}^{-3}$ (λ6716/λ6731 > 1.46).

Elemental abundance determinations using SNR spectra can be estimated with the shock-abundance models of Dopita et al. (1984). Following Smith et al. (1993), we used the ([S II] λ6731)/Hα and [N II]/Hα ratios from our spectra in M101 and interpolated across the grid of models in Figure 8 of Dopita et al. (1984) to obtain oxygen and nitrogen abundances by number. Note that Dopita et al.'s models assume a shock velocity greater than 100 km s^{-1}, while two of our 10 M101 SNR spectra with measurable

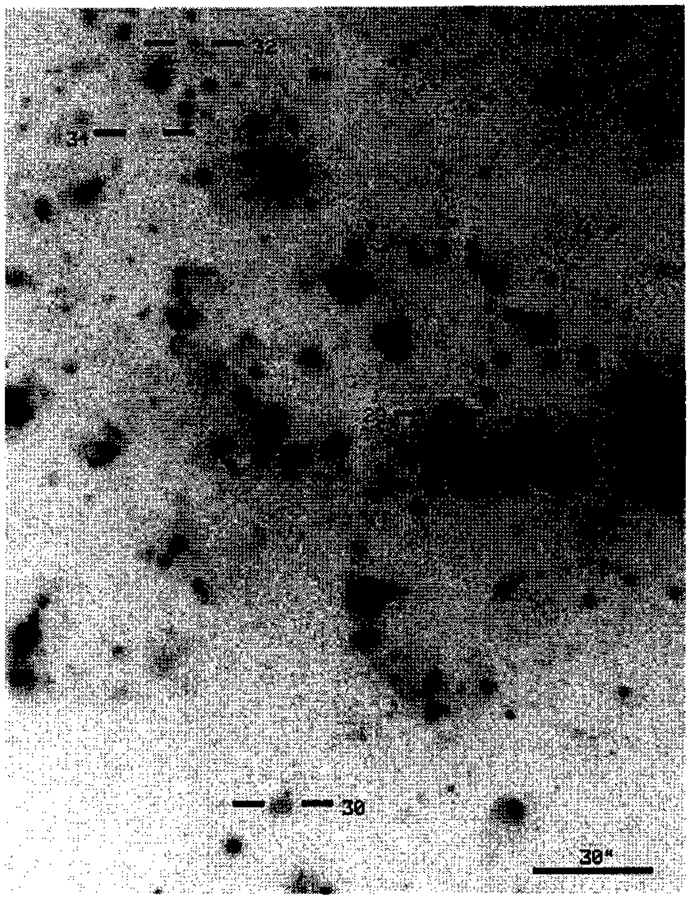

FIG. 15*b*

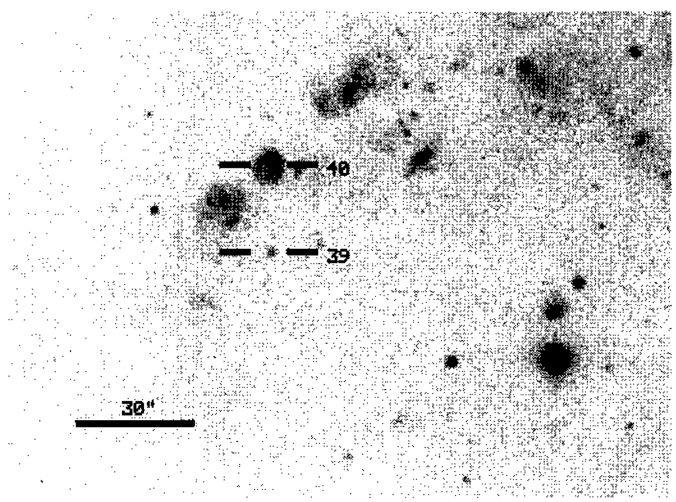

FIG. 15*c*

[N II]/Hα show [O III]/Hβ < 1, indicating shock velocity less than 100 km s^{-1}. Therefore, we removed these two spectra from the analysis. Abundance gradients were obtained by least-squares fits to the data. The oxygen abundances have a mean value of log (O/H) + 12 = 8.35 $\pm$ 0.24, a gradient of log (O/H) of -0.06 ± 0.04 kpc^{-1}, and a large scatter. Nitrogen has a mean value of log (N/H) + 12 = 7.76 $\pm$ 0.22, a gradient of log (N/H) of

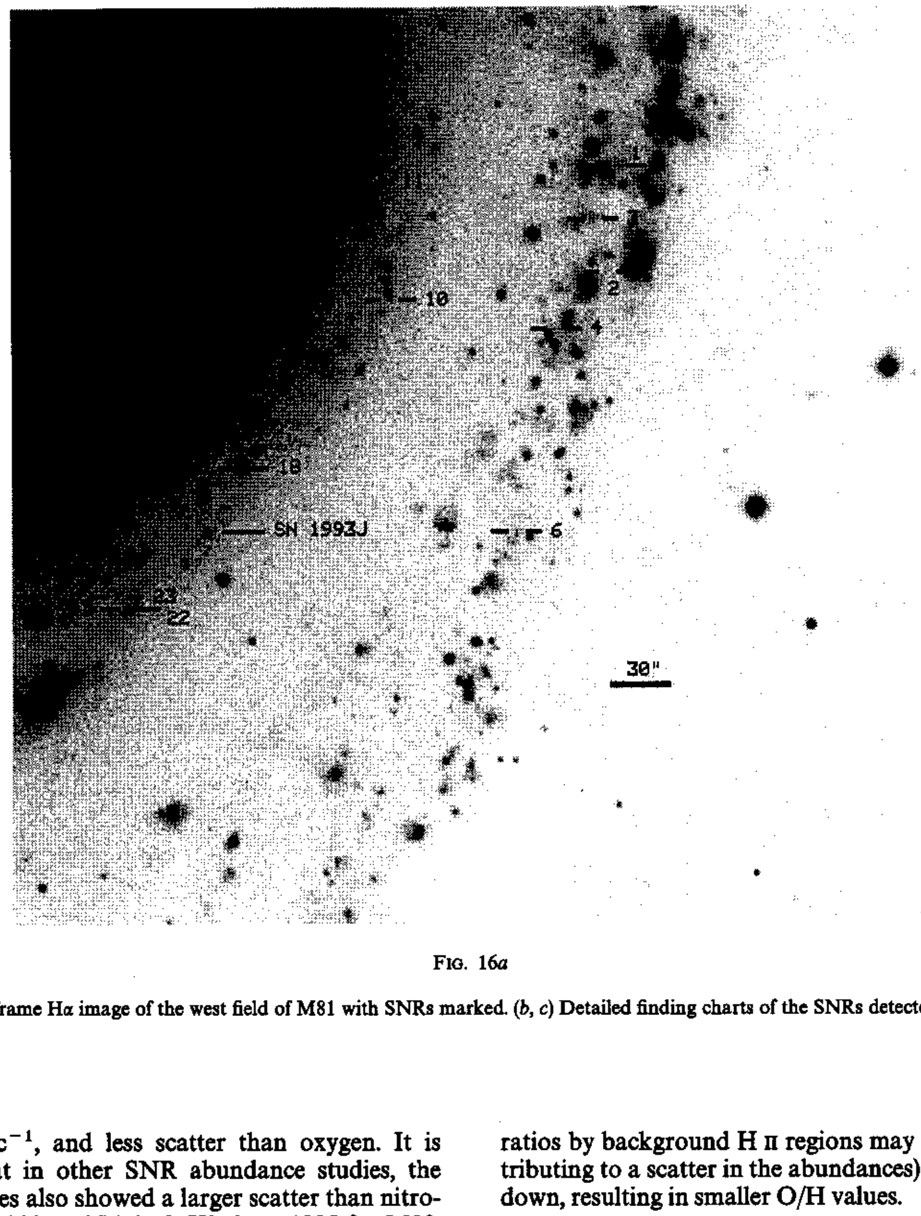

FIG. 16a

FIG. 16.—(a) Full-frame Hα image of the west field of M81 with SNRs marked. (b, c) Detailed finding charts of the SNRs detected in two sections of this field.

-0.09 ± 0.03 kpc^{-1}, and less scatter than oxygen. It is worth noting that in other SNR abundance studies, the oxygen abundances also showed a larger scatter than nitrogen (Smith et al. 1993 and Blair & Kirshner 1985 for M33, Blair & Kirshner 1985 for M31, Russell & Dopita 1990 for the LMC, and Fesen et al. 1985 for our Galaxy).

Using M101 H II region data from McCall, Rybski, & Shields (1985) and Smith (1975) and calibrating the data using the method of Zaritsky, Kennicutt, & Huchra (1994), we calculated oxygen abundances and obtained a mean value of log (O/H) + 12 = 8.64 ± 0.31 and a gradient of log (O/H) of -0.06 ± 0.01 kpc^{-1}, similar to what we found from the SNRs. It is difficult to compare abundance gradients from these SNRs and H II regions in M101 because the range of galactocentric distance covered by our SNRs is less than half that covered by the H II regions. However, the mean oxygen abundance from H II regions in M101 is greater than that from our SNRs by ≈ 0.3 dex. A similar result has been seen for M33 (Smith et al. 1993), for M31 (Blair, Kirshner, & Chevalier 1982; Blair & Kirshner 1985), for the LMC (Russell & Dopita 1990), and for our Galaxy (Shaver et al. 1983; Fesen et al. 1985). As discussed in Smith et al. (1993), it is possible that contamination of SNR line ratios by background H II regions may (in addition to contributing to a scatter in the abundances) drive the line ratios down, resulting in smaller O/H values.

4.4. *Large SNRs*

What is the largest size the remnant of a single SN can have while remaining optically bright enough to detect? This maximum size depends on the energy input of the SN, the mass of the SN ejecta, the ISM density, and the amount of energy radiated by the SNR as it expands (see Lozinskaya 1992 for a review). Starting with a canonical explosion energy of $E_0 = 10^{51}$ ergs, ejecta mass of 1 $M_\odot$, $v_0 = 10^4$ km s^{-1}, and ISM density of 1 cm^{-3} at the lowest shock velocity at which an SNR can still be optically observed ($v_s \sim 50$ km s^{-1}), models of SNR evolution show that $D_{\max} \sim 100$ pc. While $D_{\max}$ can be larger for smaller v_s and/or n_0, we will use $D_{\max} \sim 100$ pc as the upper limit in size for a SNR produced by a single SN and therefore consider any object with $D > 100$ pc as the likely result of more than one SN.

There are 31 objects in our survey with diameters ranging from 100 to 300 pc. These diameter estimates depend on the assumed distance to each galaxy, which may be uncertain

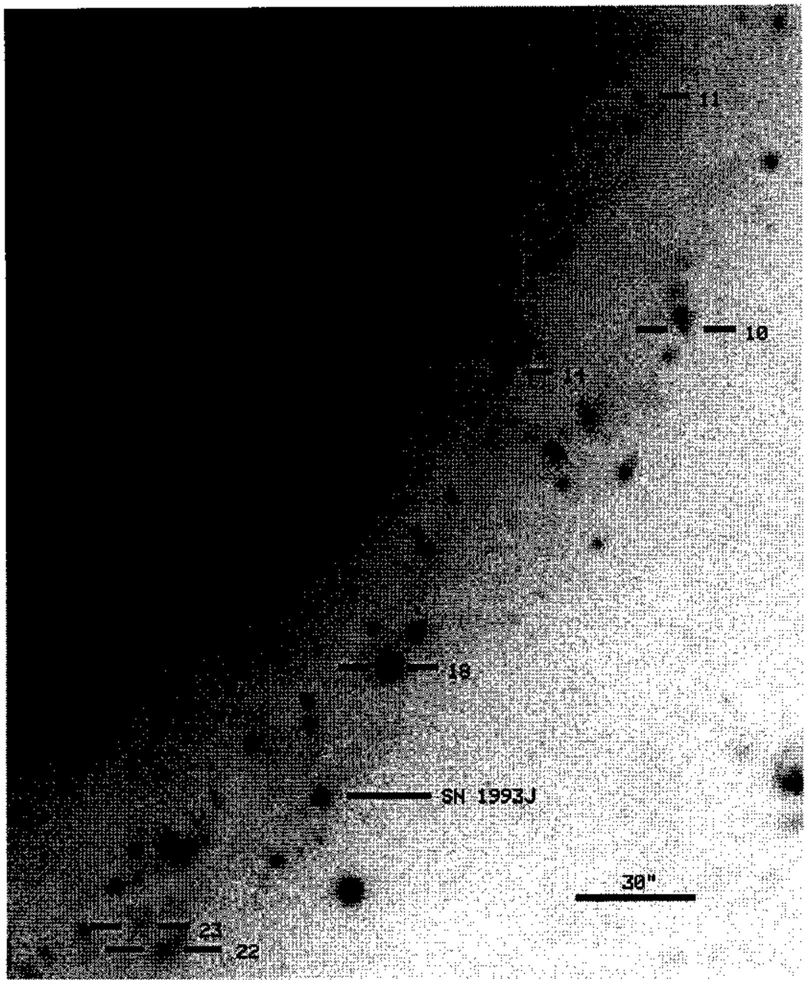

FIG. 16b

by as much as a factor of 2. Assuming that our diameter estimates are correct, however, what is the nature of these large objects? In Figure 30, we plot [S II]/Hα versus diameter for all the SNRs for which we could measure a diameter. The bottom right of that plot contains those 15 objects with $D > 100$ pc (and [S II]/Hα < 0.6) that may be stellar wind–shocked nebulae, diffuse ionized gas, or a combination of these with SNRs. Objects on the top right of Figure 30 (with $D > 100$ pc and [S II]/Hα ≥ 0.6) lie outside the normal range of parameters for stellar wind–shocked nebulae and diffuse ionized gas and therefore may be multiple SNRs (MSNRs).

MSNR shells with $D \sim 100$–300 pc have been shown to form easily as a result of SN explosions in a modest-sized OB association (McCray & Kafatos 1987; Tenorio-Tagle & Bodenheimer 1988), although with lower shock velocities ($v_s \sim 10$–30 km s^{-1}) than expected for an optically detectable SNR. Radio observations at 21 cm have detected MSNR shells in the Local Group with $D \gtrsim 200$ pc (McCray & Kafatos 1987), and Chu et al. (1993, 1995) discussed recent X-ray observations of possible MSNRs in the LMC. Optical shells are typically somewhat smaller and often contain clusters of OB stars. With the possible exception of the two objects in M101 mentioned in § 3 (in which we could detect only one or two stars), we were unable to detect stellar clusters within any of our large SNRs.

There are four objects in the data set with $D > 100$ pc for which we can estimate the shock velocity. Figure 5 of Dopita et al. (1984) shows log [([O III] λ5007)/Hβ] versus v_s for their shock models, assuming cosmic abundances. Using measured line ratios of the four objects with $D > 100$ pc for which we have spectra, we obtained the shock velocity estimates shown in Table 17. The estimated velocities are all ~ 85 km s^{-1}, well above the velocities expected for MSNRs. The kinematic ages of the four objects in Table 17 also are mostly smaller than those found for MSNRs. Although the ([O III] λ5007)/Hβ ratio is affected by differences in abundance, Figure 5 of Dopita et al. shows that the [O III] λ5007 line is extremely sensitive to the shock conditions and basically shuts off for velocities $\lesssim 80$ km s^{-1} (see also Smith et al. 1993). The fact that three of the four SNRs with $D > 100$ pc for which we also obtained spectra show fairly bright [O III] is strong evidence that they are high-velocity shock-heated nebulae (i.e., SNRs).

One of the objects in Table 17, NGC 5585 SNR No. 1, is an especially interesting object and a good example of an

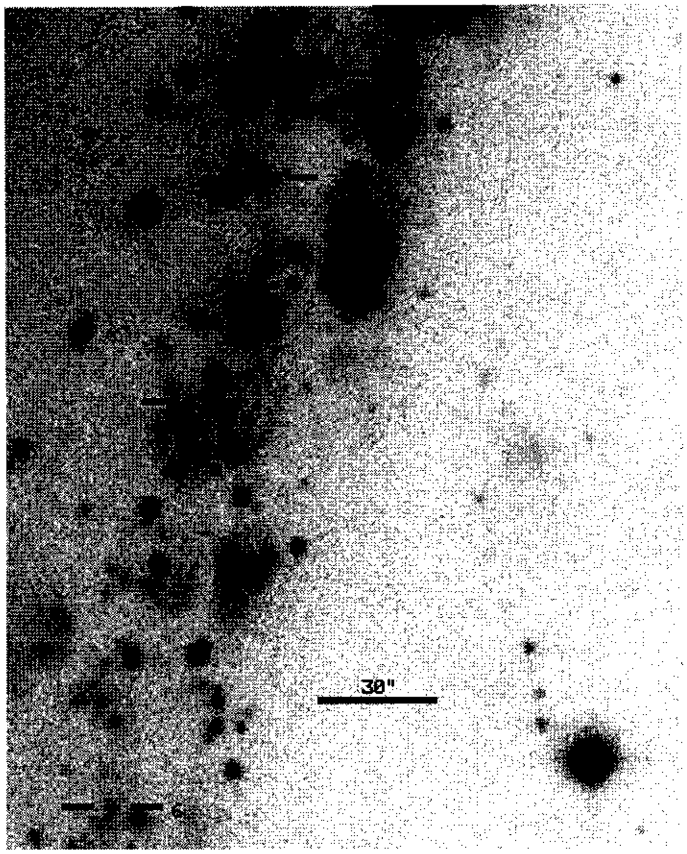

FIG. 16c

unusually large SNR. As shown in Figure 38, the remnant is elliptical, with its major axis running almost north-south and a small, bright H II region located on its northern edge. Bright in both [O I] and [O III], NGC 5585 SNR No. 1 is clearly a SNR. Because a remnant will expand to larger diameters in a less dense region, it is possible that NGC 5585 SNR No. 1's large size is a result of its being located in a region of especially low-density ISM. We measured NGC 5585 SNR No. 1's galactocentric distance to be $\sim 2\!\!'.45$, which is just past the beginning of a significant decrease in H I surface density in NGC 5585, as shown in Cote, Carignan, & Sancisi (1991). The remnant also appears slightly brighter on its eastern and northeastern limbs (Fig. 38), possibly indicating higher density at those points.

NGC 5585 SNR No. 1 is quite similar in morphology to the NGC 7793 remnants N7793-S26 and N7793-S26ext found by Blair & Long (1997), which they thought might represent a single object. Blair & Long believed that N7793-S26, S26ext may be the result of multiple SNs creating a large, shock-heated bubble, which eventually may become a superbubble. They found no interior stars in this object, however. For comparison, the estimated diameter of NGC 5585 SNR No. 1 is about half that of N7793-S26, S26ext (140 pc vs. 260 pc), while the [S II]/Hα ratio is somewhat higher for the former (0.66 vs. 0.50–0.64). Both objects are located near the outer regions of their parent galaxies. Note that, in their survey, Blair & Long found several SNRs with $D > 100$ pc (three in NGC 300, six in NGC 7793).

5. COMPARISONS BETWEEN SNR SAMPLES IN DIFFERENT GALAXIES

Combining the SNR samples from this work with other SNR samples from galaxies searched using ground-based optical observations, we have an ensemble of 12 optical SNR samples in nearby galaxies, all spiral, except for one irregular galaxy. Here we compare the major properties of these independent SNR samples and their parent galaxies and investigate selection effects and physical trends that might allow us to make predictions about optical SNR samples obtained in other galaxies.

5.1. *The Ensemble*

Several basic properties of the 12 galaxies are listed in Table 18. For consistency, the distances to the LMC and SMC and to M31, M33, NGC 300, and NGC 7793 are those used in the SNR searches that we reference. Sources of all the galactic data are also listed.

The properties of the SNR samples are listed in Tables 19 and 20. For the LMC, we did not include Balmer-dominated remnants nor any objects with [S II]/Hα < 0.4 because we would not have identified them as SNRs. In the SMC, one of the objects (number 0104−723 in Mathewson et al. 1984) may be Balmer-dominated. In the columns for diameter, Hα intensity, and [S II]/Hα, we list "mode" and maximum values for each sample. The mode is simply the most common value observed for a given parameter (i.e., the

TABLE 16

EMISSION-LINE RATIOS FOR SNRs WITH SPECTRA

SNR No.	D[a] (pc)	[O III]/Hβ	[O I]/Hα	[N II]/Hα	[S II]/Hα	λ6731/Hα	λ6716/λ6731	N_e[b] (cm^{-3})
				NGC 5204				
2	60	1.38	0.23	0.15	0.69	0.30	1.32	120
3	50	1.28	0.12	0.15	0.52	0.19	1.46[c]	<10
				NGC 5585				
1	140	1.02	0.29	0.14	0.66	0.28	1.40	40
3	20	...	...	0.17	0.64	0.23	1.46[c]	<10
4	60	3.28	...	0.23	0.47	0.19	1.46[c]	<10
5	...	0.66	0.15	0.14	0.49	0.21	1.37	75
				NGC 6946				
4	...	...	0.26	0.94	0.85	0.37	1.30	140
15	30	1.50	...	0.53	0.58	0.23	1.46[c]	<10
16[d]	20	8.80	0.37	1.15	0.85	0.38	1.22	225
18	40	...	...	0.57	0.52	0.24	1.17	290
25	60	0.46	0.07	0.49	0.58	0.24	1.36	75
27	40	0.23	0.11	0.42	0.51	0.22	1.35	90
				M81				
2	60	...	...	0.54	0.72	0.27	1.46[c]	<10
17	30	2.27	0.44	1.31	1.22	0.52	1.32	120
18	130	0.31	0.08	0.83	0.70	0.25	1.46[c]	<10
25	10	3.62	0.29	1.24	0.93	0.42	1.22	215
				M101				
17	40	1.61	0.13	0.75	0.90	0.37	1.46[c]	<10
19	140	2.15	0.28	0.84	0.93	0.39	1.46[c]	<10
21	30	7.38	0.32	0.81	0.88	0.36	1.46[c]	<10
24	30	4.39	0.50	1.02	1.06	0.50	1.10	385
33	10	2.68	...	0.96	0.70	0.30	1.40	50
38	80	...	0.18	...	0.71	0.29	1.35	90
44	...	0.37	0.09	0.14	0.53	0.22	1.43	25
50	9	2.04	0.17	1.59	0.81	0.46	0.74	1720
71	30	0.40	0.14	0.58	0.76	0.32	1.36	75
76	...	1.07	0.24	0.35	0.62	0.24	1.46[c]	<10
83	200	2.41	0.14	0.85	0.76	0.25	1.46[c]	<10

[a] Geometric mean diameter for noncircular objects. Objects for which no values are given were in confused regions or were too small and faint to estimate the diameter.

[b] Used the Space Telescope Science Data Analysis System task "nebular.temden," based on the five-level atom approximation of De Robertis et al. 1987. Assumed T = 10,000 K.

[c] Ratio was calculated to be greater than 1.46, which is unphysical. The value was therefore set to the low-density limit.

[d] Blair & Fesen 1994.

x-axis location of the peak of its histogram); the maximum is the largest value observed. Because of the small number of remnants detected in NGC 5204 and NGC 5585, we are only able to give average (as opposed to mode) values for diameter, Ha intensity, and [S II]/Hα. In calculating the D_{mode} value in M31, we did not include the "unresolved" objects from the survey of Magnier et al. (1995) because these objects were only ~1 pixel in size and were not deconvolved to give accurate diameters. For the maximum value of SNR diameter, the geometric mean is given for elliptical

TABLE 17

SNRs WITH D > 100 PC AND MEASURED [O III] λ5007

Object	D (pc)	([O III] λ5007)/Hβ	v_s[a] (km s^{-1})	$D/2v_s$[b] (yr)
NGC 5585 SNR No. 1......	140[c]	0.72	82	8×10^5
M81 SNR No. 18............	130	0.31	82	8×10^5
M101 SNR No. 19	140	1.76	85	8×10^5
M101 SNR No. 83	200	2.01	86	1×10^6

[a] Using Figure 5 of Dopita et al. 1984.

[b] Kinematic age.

[c] Geometric mean diameter.

TABLE 18

GALAXY PROPERTIES

Name	Type	i (deg)	E_{B-V} (mag)	R (Mpc)	D_{galaxy} (kpc)	L ($10^{10} L_{\odot}$)	M(H I) ($10^9 M_{\odot}$)
LMC	Sm	35	0.07	0.055	10.6	0.36	0.8
SMC	Im	61	0.04	0.063	4.7	0.07	0.9
M31	Sb	78	0.04	0.69	31.2	2.8	4.0
M33	Scd	56	0.04	0.84	12.8	0.47	1.8
NGC 300	Sd	46	0.01	2.1	11.7	0.26	2.4
NGC 2403	Scd	62	0.03	3.2	19.9	0.66	3.6
NGC 7793	Sdm	50	0.01	3.4	8.5	0.28	0.7
M81	Sab	60	0.04	3.6	21.2	2.3	3.0
NGC 5204	Sm	53	0.00	4.8	6.1	0.08	0.6
M101	Scd	0	0.00	5.4	37.4	2.4	11.3
NGC 6946	Scd	42	0.40	5.5	23.8	3.2	6.3
NGC 5585	Sd	51	0.00	7.0	10.4	0.24	1.4

NOTE—Type and inclination data from Tully 1988. E_{B-V} values from Tully 1988 and Burstein & Heiles 1978. R values for the LMC and SMC are from Mathewson et al. 1983, for M31, from Walterbos & Braun 1992, for M33, from Gordon 1994, for NGC 300 and NGC 7793, from Blair & Long 1997, and for the rest, from Table 2. For consistency, distances are those used in the SNR studies. D_{galaxy} = galaxy diameter from isophotal diameter, corrected for projection and obscuration, from Tully 1988 and using distances given here. L = intrinsic blue luminosity of galaxy, using B from Tully 1988 and distances given here. M(H I) = mass of neutral hydrogen in galaxy, using H I flux from Tully 1988 and distances given here.

TABLE 19

SNR SAMPLE PROPERTIES

GALAXY[a]	NUMBER OF SNRs[b]	D^c (pc) Mode	D^c (pc) Max	I(Hα) (ergs cm^{-2} s^{-1}) Mode	I(Hα) (ergs cm^{-2} s^{-1}) Max	[S II]/Hα Mode	[S II]/Hα Max
LMC	28	30	90	...	...	0.6	1.4
SMC	11	58	62	...	...	0.7	0.8
M31	221	32	195	4.4E−15	2.6E−12	0.52	1.20
M33	98	35	126	1.3E−14	3.4E−13	0.65	1.55
NGC 300	28	43	200	4.5E−15	1.3E−13	0.75	1.16
NGC 2403	35	70	170	2.0E−14	1.4E−13	0.58	1.11
NGC 7793	28	32	260	2.0E−14	1.5E−13	0.50	1.79
M81	41	30	130	2.0E−15	3.6E−14	0.67	1.64
NGC 5204	3	40	60	5.5E−15	1.1E−14	0.58	0.69
M101	93	30	300	3.2E−15	4.7E−14	0.55	1.59
NGC 6946	27	30	180	2.4E−15	7.1E−14	0.55	1.14
NGC 5585	5	60	130	1.4E−14	3.1E−14	0.59	0.68

[a] SNR references: LMC, Mathewson et al. 1983, 1984, 1985, Chu & Kennicutt 1988b, van den Bergh 1988, Smith et al. 1994; SMC, Mathewson & Clarke 1972, 1973b, Mathewson et al. 1983, 1984; M31, D'Odorico et al. 1980, Blair et al. 1981, Walterbos & Braun 1992, Braun & Walterbos 1993, Magnier et al. 1995; M33, Gordon 1994; NGC 300 and NGC 7793, Blair & Long 1997; the rest, this work.

[b] From optical surveys.

[c] Mode = peak of histogram.

TABLE 20

OTHER SNR SAMPLE PROPERTIES

GALAXY	$\sigma \sim e^{-r/r_0}$: σ_{peak} (kpc^{-2})	$\sigma \sim e^{-r/r_0}$: r_0 (kpc)	ASSOCIATED?[a] H II Regions	ASSOCIATED?[a] Arms	FRACTION SURVEYED
LMC	...	...	Yes	...	1.00
SMC	...	...	...	...	1.00
M31	...	...	...	Yes	0.75
M33	2.71	2.1	Yes	...	1.00
NGC 300	0.85	1.3	...	...	1.00
NGC 2403	2.23	0.7	Yes	...	0.95
NGC 7793	0.70	1.1	...	...	1.00
M81	0.39	2.2	Yes	Yes	1.00
NGC 5204	...	...	...	...	1.00
M101	0.50	3.6	Yes	Yes	0.98
NGC 6946	0.32	4.4	No	?	0.95
NGC 5585	0.21	1.3	...	...	1.00

[a] With H II regions and/or spiral arms.

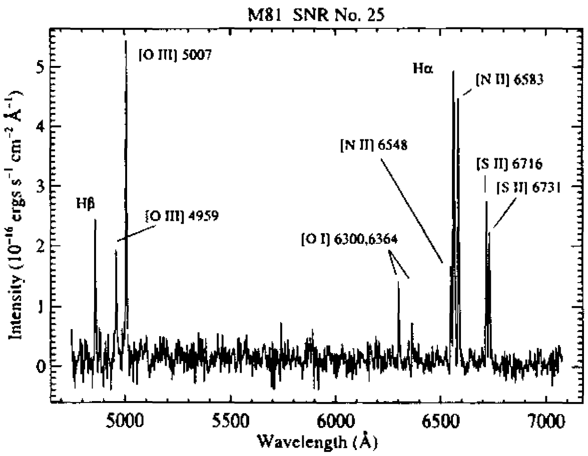

FIG. 17*a*

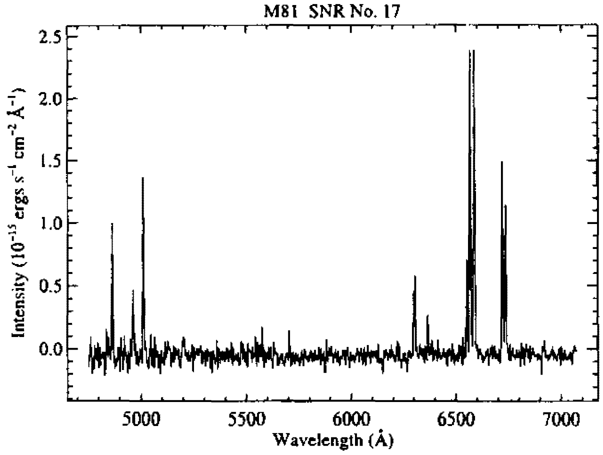

FIG. 17*b*

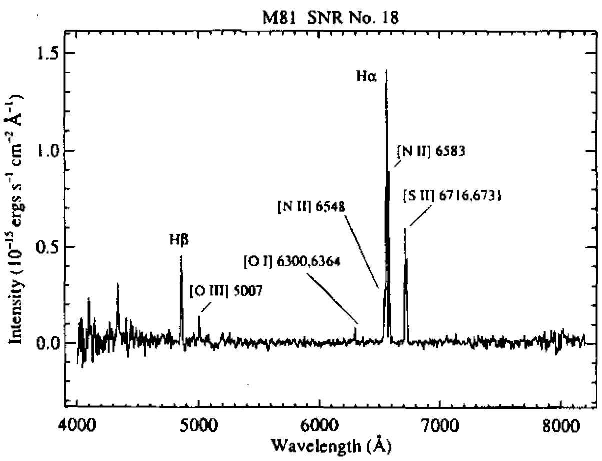

FIG. 17*c*

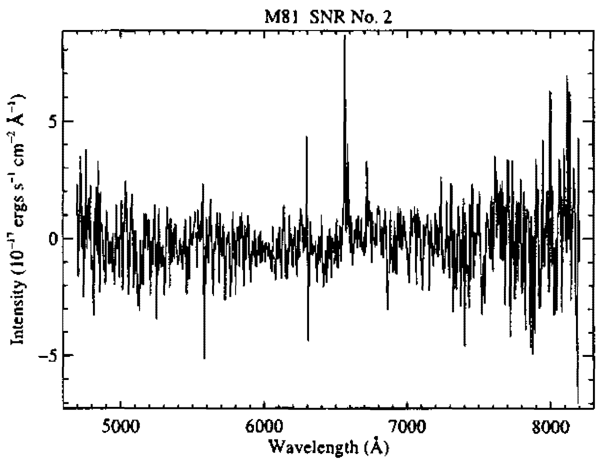

FIG. 17*d*

FIG. 17.—M81 SNR spectra

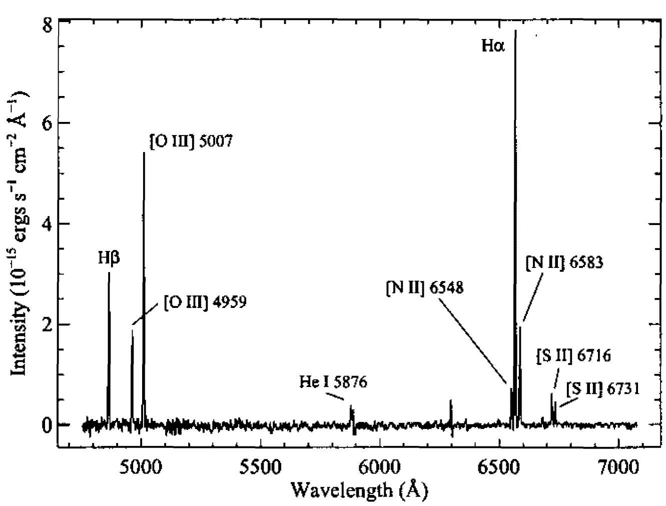

FIG. 18.—A typical M81 H II region spectrum, from the small nebula located ~20″ directly west of M81 SNR No. 19 and just northwest of a larger H II region.

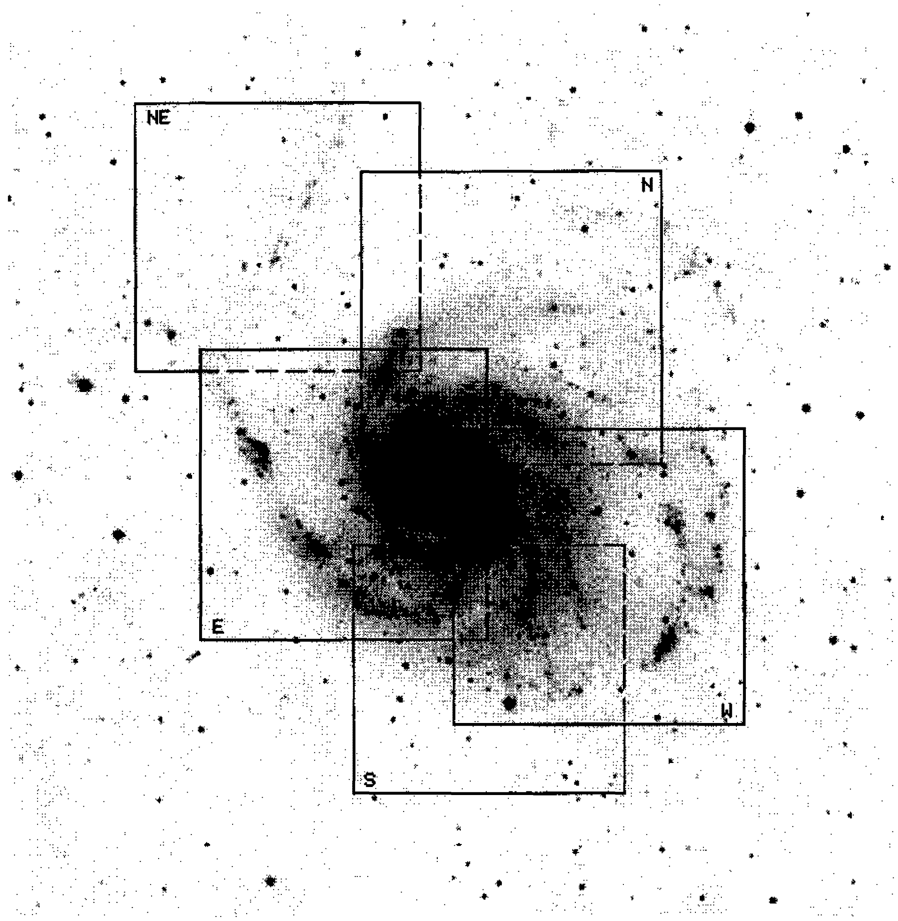

FIG. 19.—Digitized Sky Survey E image of M101 showing the fields observed

objects (for the LMC and SMC, the mean diameter is given). Hα intensity values for M31 are from the 52 SNRs in the samples of Braun & Walterbos (1993) and Walterbos & Braun (1992). In M33, NGC 300, and NGC 7793, we converted the published Hα surface brightness values to Hα intensity using the given diameters. The M33 Hα intensity values were not corrected for extinction, which was believed to be slight. [S II]/Hα ratios were available for only four SNRs in the SMC. The [S II]/Hα values in M31 are from the 52 SNRs in the sample of Braun & Walterbos (1993) and Walterbos & Braun (1992). NGC 300 and NGC 7793 [S II]/Hα values are from the spectral data in Blair & Long (1997) for 21 SNRs in NGC 300 and 27 SNRs in NGC 7793. The quantity σ is the surface density of SNRs observed in a given galaxy, normally of form $\sigma \sim e^{-r/r_0}$, with r_0 the scale length. The LMC SNRs are listed as being associated with H II regions because Chu & Kennicutt (1988b) found that at least two-thirds of the SNRs detected in the LMC are associated with Population I objects. Magnier et al. (1995) found that the distribution of SNRs they detected in M31 tended to trace the spiral arms, so we list them as associated with the spiral arms. In M33, Gordon (1994) surmised that the observed SNRs are associated with H II regions because of the similarity between the two objects' radial distributions.

5.2. *Ensemble Selection Effects*

Just as selection effects and biases are present in the individual SNR samples, we expected to see evidence of selection effects and biases when comparing SNR samples from different galaxies. One such selection effect is shown in Figure 39, where the log of the mode of the Hα luminosity versus galaxy distance is plotted. SNR Hα luminosity is calculated from the Hα intensity given in Table 19, using the galaxy distances in Table 18. Figure 39 shows larger $L(\mathrm{H}\alpha)_{\mathrm{mode}}$ for more distant galaxies, which is clearly a selection bias. If we could detect every SNR in a galaxy, and compare the SNR samples among the galaxies, we would expect about the same value of $L(\mathrm{H}\alpha)_{\mathrm{mode}}$ in each galaxy, assuming that SNRs in spiral galaxies form under roughly similar conditions. Of course, we cannot detect every SNR in a galaxy. As we move to more distant galaxies, fainter SNRs become more difficult to detect and $L(\mathrm{H}\alpha)_{\mathrm{mode}}$ shifts to higher values, just as seen in Figure 39.

In Figure 40, we plot the peak SNR surface density in each galaxy, σ_{peak}, as a function of the galaxy distance. Note that surface density data was only available for eight of the 12 sample galaxies. The general trend in the plot is toward larger σ_{peak} for nearer galaxies because it is easier to detect SNRs in closer galaxies and especially to resolve confused

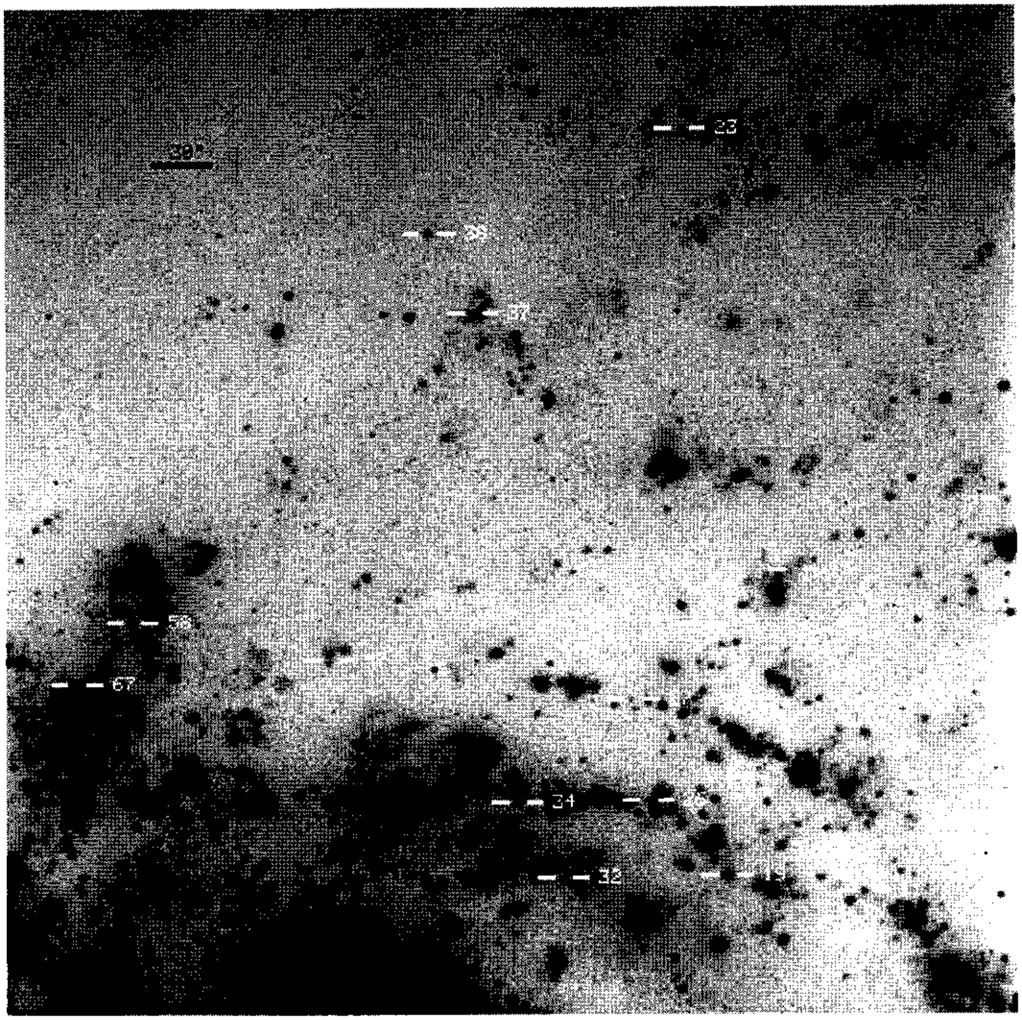

FIG. 20a

FIG. 20.—(a) Full-frame Hα image of the north field of M101, with SNRs marked. (b–d) Detailed finding charts of the SNRs detected in three sections of this field.

regions near a galaxy's center in order to detect a greater surface density of SNRs. The σ_{peak} values of M33 and NGC 2403 are much higher than those of the other galaxies, possibly because of the higher resolution image data used.

No apparent correlation was evident between the maximum SNR diameter measured in each sample, D_{max}, and galaxy distance. However, a correlation was evident between D_{max} and galaxy diameter, D_{galaxy}. To eliminate any effect of errors in the galaxy distance estimates, D_{max} and D_{galaxy} were converted to arcseconds, giving the plot shown in Figure 41. The dashed line is a least-squares fit to the data. As shown in the figure, the fit seems to indicate that for a SNR sample obtained by ground-based optical observations of any spiral galaxy, the size of the largest detectable SNR is a function of the size of its parent galaxy. Although this correlation is just a distance-size effect, it may allow one to predict the largest SNR optically detectable in a given galaxy. Using galaxies at well-known distances as calibrators, this trend suggests that a rough estimate of a galaxy's distance can be obtained by finding D_{max} in arcseconds for a sample of SNRs obtained through ground-based optical observations of the galaxy. The dispersion in D_{max} ($\sim 0\overset{''}{.}2$ in our samples) must be included in calculating the uncertainty in the distance estimate.

5.3. *Physical Trends in the Ensemble*

The 12 galaxy SNR ensemble also yielded trends that may be related to the physical state of the SNRs and their parent galaxies. For example, to investigate the number of SNRs found versus a given galaxy type, the number of SNRs detected in each galaxy was divided by that galaxy's H I mass; this quantity, times the galaxy distance, is plotted versus the galaxy type in Figure 42. The quantity (galaxy distance)(number of SNRs)/(galaxy H I mass) is used in an attempt to eliminate the effects of galaxy distance and/or mass on the number of SNRs detected. Except for NGC 7793, the plot indicates that fewer SNRs per unit galaxy H I mass (correcting for the distances) are found in later type galaxies.

The most commonly observed diameter in each SNR

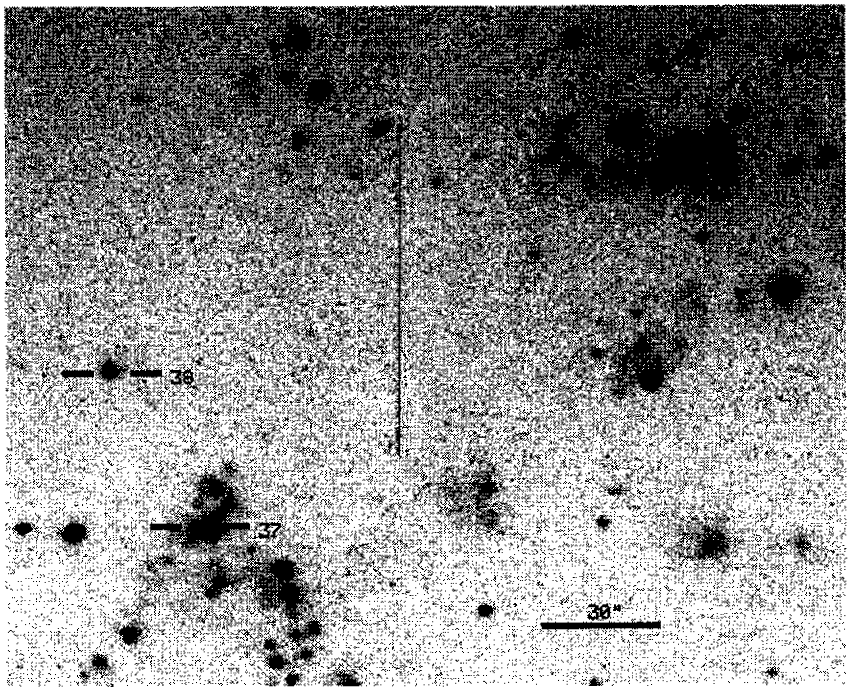

FIG. 20*b*

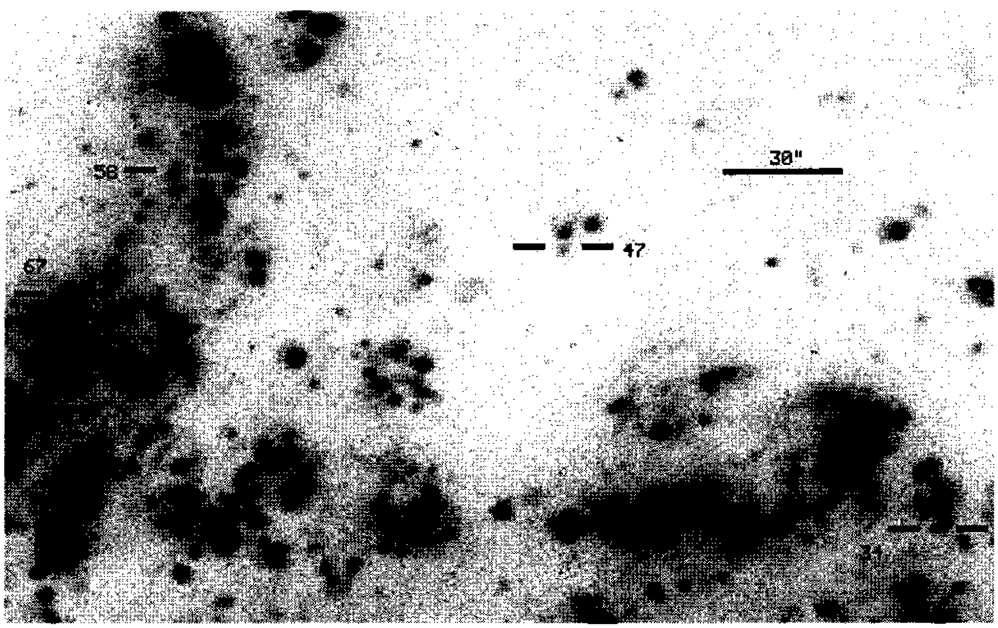

FIG. 20*c*

sample, D_{mode}, was found, in several galaxies (see Table 19), to lie at ~30–40 pc. This would seem to suggest that the most common value of SNR diameter observed in an optical SNR survey is the same in any galaxy. Recall that an SNR's apparent diameter, in terms of D_{mode}, is given by log D_{mode} (arcseconds) = $-\log R$ (Mpc) + log [$0.206265 D_{\text{mode}}$ (pc)]. If D_{mode} (pc) is constant for an ensemble of SNR samples, then a plot of log D_{mode} (arcseconds) versus log R (Mpc) should be a straight line with slope -1, whose y-intercept will give us an estimate of D_{mode} (pc). Such a plot is

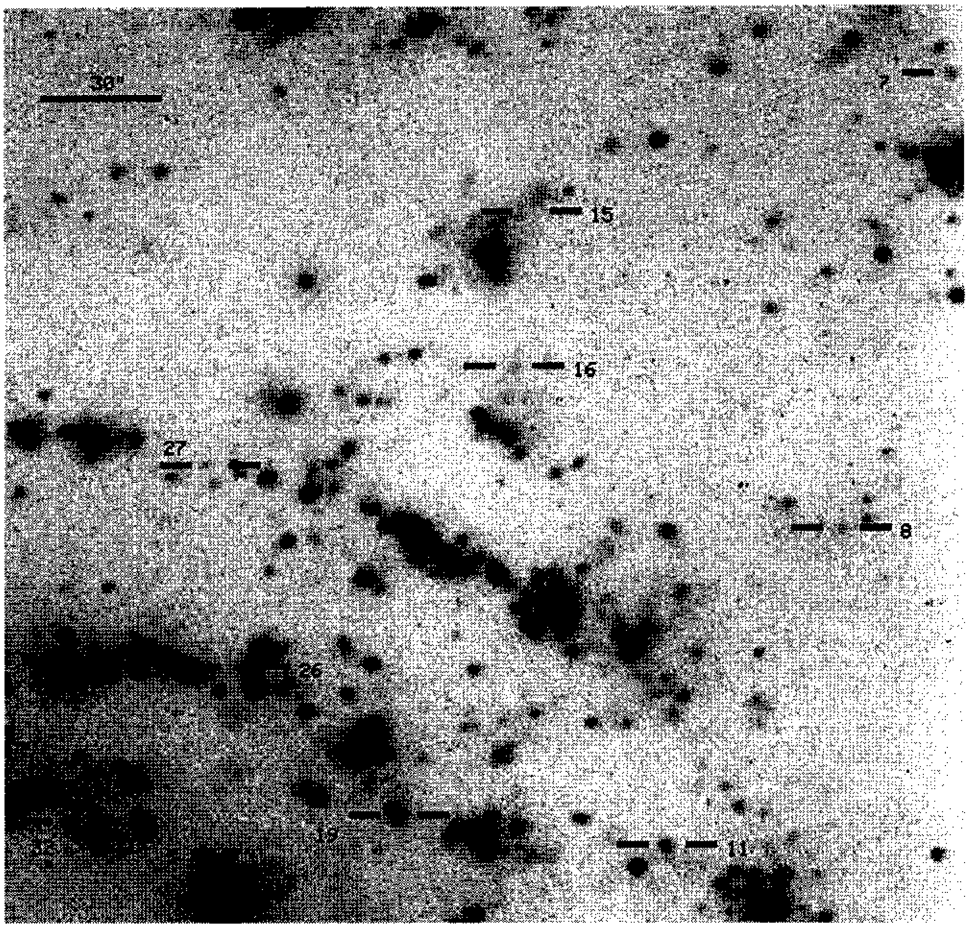

FIG. 20*d*

shown in Figure 43. The dashed line is a least-squares fit to the data and the error shown is only the error in the fit. The fit indeed has a slope of -1 and gives an estimate of $D_{\rm mode} \approx 40$ pc for a SNR sample.

Hence this analysis allows one to predict that any ground-based optical SNR survey should find $D_{\rm mode} \approx 40$ pc for a SNR sample in a spiral galaxy. The prediction assumes that the SNR sample is large enough that a reasonably accurate peak to the histogram of SNR diameters can be determined. It also is worth noting that this analysis gives a very rough prediction of a galaxy's distance. Once we have a sample of SNRs in a given galaxy, simply finding $D_{\rm mode}$ in arcseconds allows one to estimate the galaxy's distance, although this value of the distance is obviously not as accurate as one obtained by more conventional methods (e.g., Cepheids, Type Ia SNs, and so on).

Why should $D_{\rm mode}$ be constant in all the SNR samples? A constant $D_{\rm mode}$ could result from most of the detected remnants being in a similar evolutionary stage, which would tend to make their most common sizes similar. It is interesting to compare our constant $D_{\rm mode}$ value with the size of the Cygnus Loop, which is the Galactic remnant probably the most similar to the SNRs we have detected. From distance estimates based on proper motions of bright filaments, the currently accepted size of the Cygnus Loop is $D \approx 40$ pc (Lozinskaya 1992), identical to our constant $D_{\rm mode}$.

In Figure 44, $D_{\rm mode}$, in parsecs, is plotted for each of the SNR samples as a function of galaxy type. Error bars for the $D_{\rm mode}$ values were obtained by examining the SNR diameter histograms from which they were obtained (except for NGC 5204 and NGC 5585, for which the errors are the uncertainties in the mean diameters). The constant value $D_{\rm mode} \approx 40$ pc found above is marked. This plot shows that $D_{\rm mode}$ appears independent of galaxy type and, within the errors shown, has a value of about 30–40 pc.

$D_{\rm max}$ and the mass of neutral hydrogen in a galaxy, M(H I), also seem to be correlated. In Figure 45 we show a log-log plot of these quantities, with $D_{\rm max}$ in parsecs and M(H I) in units of $10^9\ M_\odot$. With the exception of NGC 7793, the data show a correlation of $D_{\rm max}$ with M(H I). If the H I mass is correlated with the relative ISM density in a galaxy, the observed trend may occur because galaxies with a denser ISM provide an environment in which larger SNRs can be detected. The reason for the lack of correlation for NGC 7793 is unclear, although recall that this galaxy was also discrepant in Figure 42. Note also that the observed trend could be influenced by size of sample effects, in that a

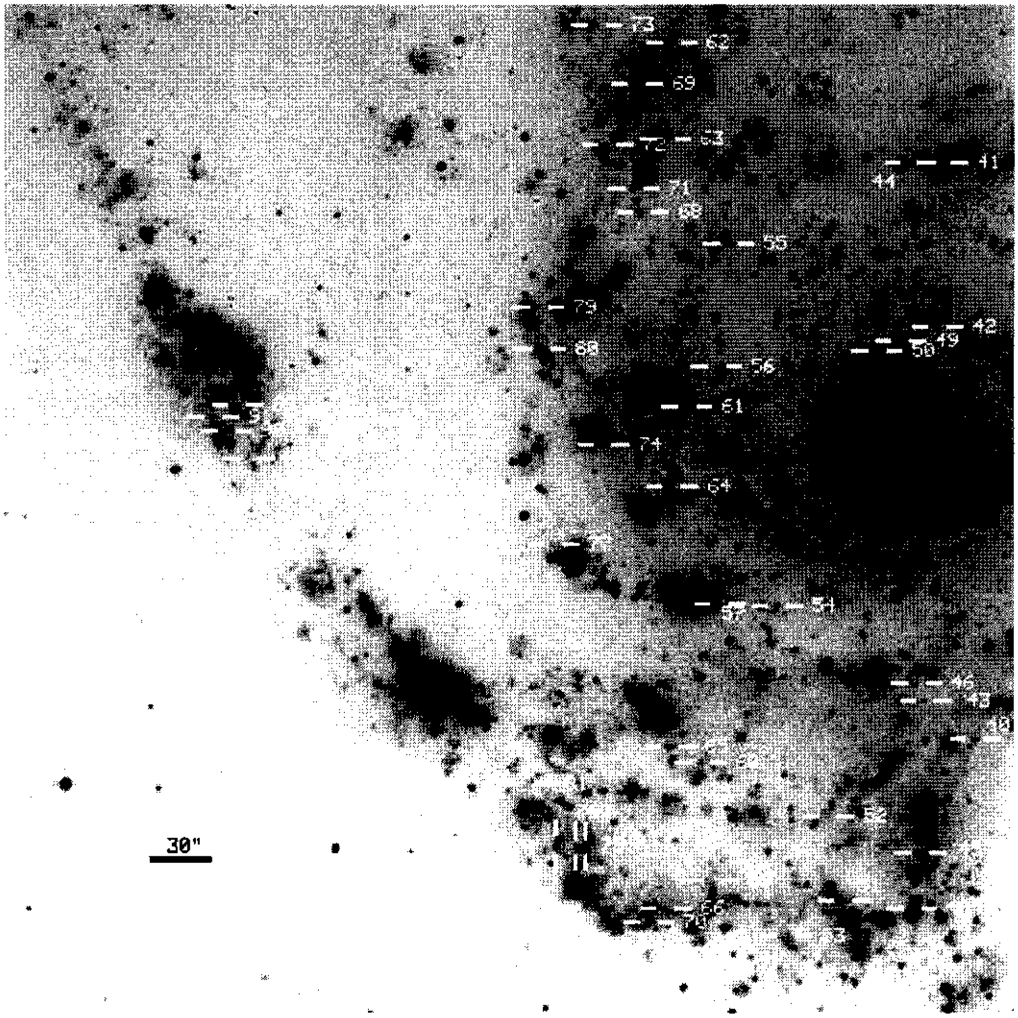

FIG. 21*a*

FIG. 21.—(*a*) Full-frame Hα image of the east field of M101, with SNRs marked. (*b*) Hα image finding chart of the SNRs detected in a section of this field. (*c*) Same as (*b*), but in [S II]. (*d*) Hα image finding chart of the SNRs detected in another section of this field. (*e*) Same as (*d*), but in [S II]. (*f*) Hα image finding chart of the SNRs detected in another section of this field.

more gas-rich galaxy will produce more SNRs and thus a larger SNR sample with, possibly, a larger D_{max}. Although D_{max} was not found to be strongly correlated with the number of SNRs detected in each sample, we did find a slight trend indicating that more SNRs were detected in the more massive galaxies, thus supporting the possibility of a size of sample effect in Figure 45.

We found no correlation between the SNR surface-density scale length, r_0, and galaxy diameter, meaning that the largest galaxies did not necessarily also have the largest SNR surface-density scale lengths. However, plotting r_0 as a function of galaxy luminosity (Fig. 46) does show a weak correlation indicating a larger SNR surface-density scale length for intrinsically brighter galaxies, which could result because the SNRs correlate with a larger population of bright, blue stars in the more luminous galaxies. If this explanation is correct, the correlation in Figure 46 provides evidence that most of the SNRs detected had bright, blue stars as progenitors that exploded as Type II or Ib/c SNs.

Finally, we investigated the possible relationship between galaxy type and association of SNRs with H II regions and spiral arms. Of the four Scd galaxies in the ensemble (M33, NGC 2403, M101, and NGC 6946), three have SNRs that appear to be associated with their galaxy's H II regions. NGC 6946 is the exception to this apparent trend among the Scd galaxies. Also, the SNRs in the Sab–Sb galaxies (M31 and M81) appear to be associated with their galaxies' spiral arms. This very limited analysis therefore suggests that, in most Scd galaxies, SNRs tend to be associated with H II regions and that, in Sab–Sb galaxies, SNRs tend to be associated with the spiral arms. It will be interesting to see if future SNR surveys in similar type galaxies find such correlations between SNRs and these other galactic objects.

6. CONCLUSIONS

We have conducted an optical search for supernova remnants in five nearby spiral galaxies. Our technique consisted

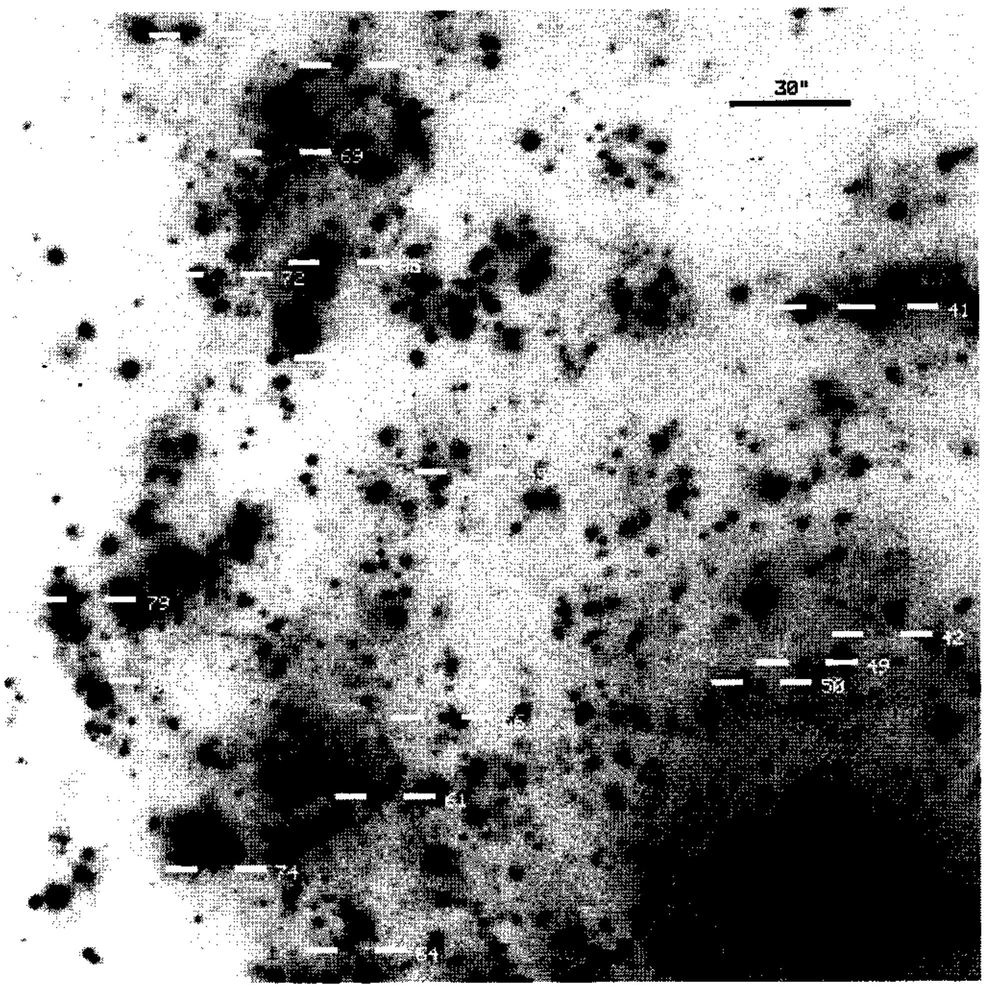

FIG. 21*b*

of imaging these galaxies using narrow Hα and [S II] λλ6716, 6731 filters, subtracting starlight with continuum-filter images, and identifying [S II]–bright emission nebulae as SNR candidates. Spectra were obtained for a few of these candidates in each galaxy and were used to correct the [S II]/Hα ratios obtained from image photometry. Emission nebulae with [S II]/Hα ≥ 0.45 were identified as probable SNRs. The results of this survey are:

1. We have identified three SNRs in NGC 5204, five in NGC 5585, 27 in NGC 6946 (including an SNR previously identified by Blair & Fesen 1994), 41 in M81, and 93 in M101. Including the LMC and SMC, M31, M33, NGC 300, NGC 7793, and NGC 2403, there are now 12 galaxies that have been well searched in the optical for SNRs, and this survey (including the NGC 2403 SNR sample of Matonick et al. 1997) has increased the number of currently detected extragalactic SNRs by about 50%.

2. An analysis of selection effects, biases, and completeness of our SNR samples shows that (1) the [S II]/Hα detection method can be seriously affected by confusion with H II regions and that (2) the samples appear biased against detecting large, faint SNRs. We estimate that there are roughly 4 times more SNRs in each of our target galaxies than we detected. Assuming a SNR lifetime of 20,000 yr, this result gives crude SN rate estimates of 1 SN per 130 yr for M81 and 1 SN per 50 yr for M101, both similar to their historical SN rates.

3. Using the distributions of detected SNRs relative to other objects (spiral arms, H II regions, molecular clouds), we find that a significant fraction of the SNRs detected in NGC 2403, M81, and M101 probably had high-mass progenitors (SNs II or Ib/c).

4. Abundances were obtained from eight SNR spectra in M101, and moderate abundance gradients in both oxygen and nitrogen were found. The SNR oxygen abundance gradient was found to be roughly similar to that obtained from H II regions. As in SNR abundance studies in other galaxies, our SNR oxygen abundance showed a larger scatter than the nitrogen abundance and was lower than the oxygen abundance obtained from H II regions.

5. We found 31 objects with diameters larger than 100 pc, larger than is physically possible for a single SNR in an ISM of typical density. Further detailed study is warranted

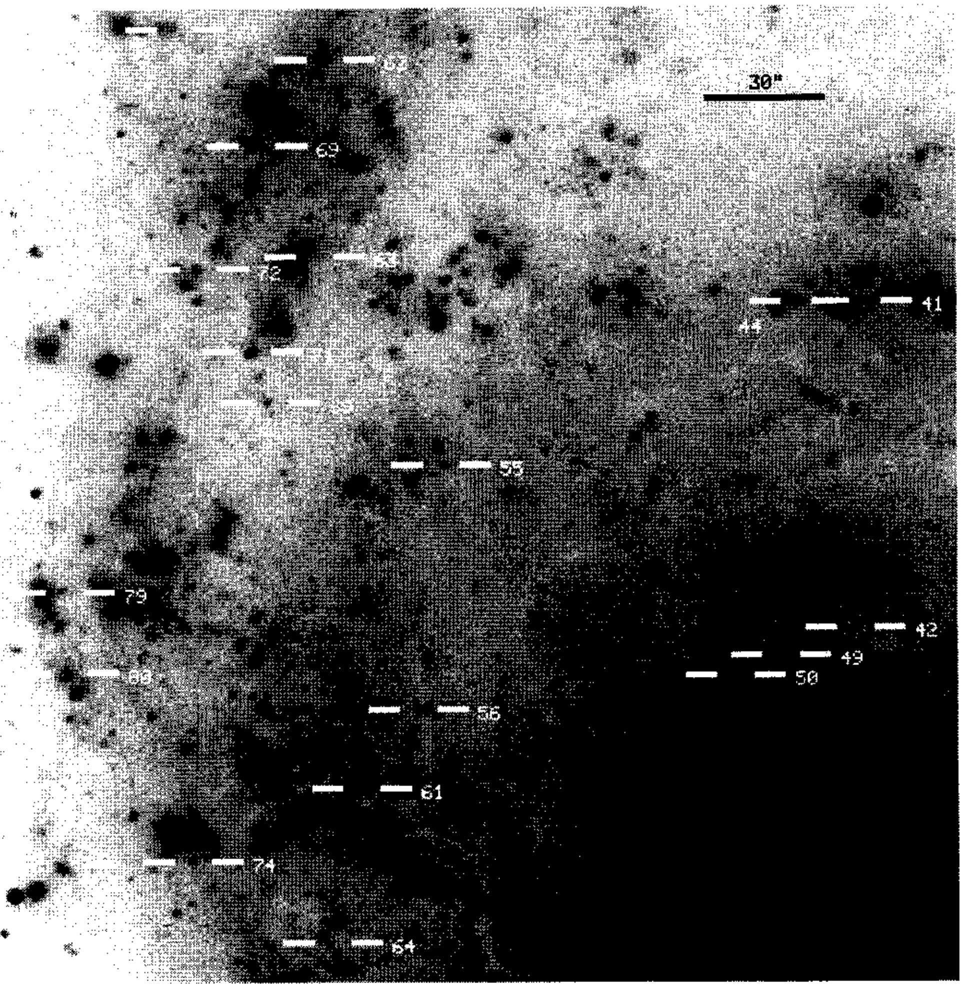

FIG. 21*c*

for these unusual objects, particularly high-resolution observations to determine the objects' shock velocities and gas densities.

6. Combining the SNR samples from this work with the optical SNR samples in the LMC and SMC and in M31, M33, NGC 300, NGC 7793, and NGC 2403 revealed the following: (1) An apparent trend of higher $L(\mathrm{H}\alpha)_{\mathrm{mode}}$ with increasing galaxy distance, probably as a result of intrinsically fainter SNRs becoming more difficult to detect in more distant galaxies, thereby causing $L(\mathrm{H}\alpha)_{\mathrm{mode}}$ to shift to a higher value. (2) A value of $D_{\mathrm{mode}} \approx 40$ pc for each SNR sample in the ensemble, which may indicate that most of the detected SNRs are in a similar evolutionary stage.

A worthwhile follow-up study would be to broaden the search for SNRs to include a wider range of galaxy types. Although one may not find many SNRs in elliptical galaxies because of the absence of significant interstellar gas, it might be interesting to examine Sa and progressively earlier type galaxies to see at what galaxy type one is no longer able to detect SNRs. It might also be worth conducting a distribution analysis, similar to that done in our program galaxies, on the SNR samples in M31, M33, NGC 300, and NGC 7793 using precise positions of spiral arms, H II regions, and molecular clouds. Such an analysis would allow one to determine whether the SNRs are closely associated with these objects and therefore give a better indication of the likely SNR progenitors in these galaxies. Finally, the nature of the very large SNRs we have found (such as NGC 5585 SNR No. 1) needs to be investigated further. High-resolution imaging to search for early-type stars with strong stellar winds interior to these objects, as well as additional observations at other wavelengths, should lead to a better understanding of the properties of these enormous remnants.

It is a pleasure to thank the staff of MDM Observatory for their assistance with the instrument setup in the observation portion of this project. We also wish to thank J. Raymond for kindly loaning us the interference filters used in the imaging portion of this project, W. Blair for many helpful comments and suggestions, and S. van den Bergh for reviewing an earlier draft of this paper and providing much useful advice. This research was funded in part by NSF grant 95-29232 and a Burke Research Grant from Dartmouth College.

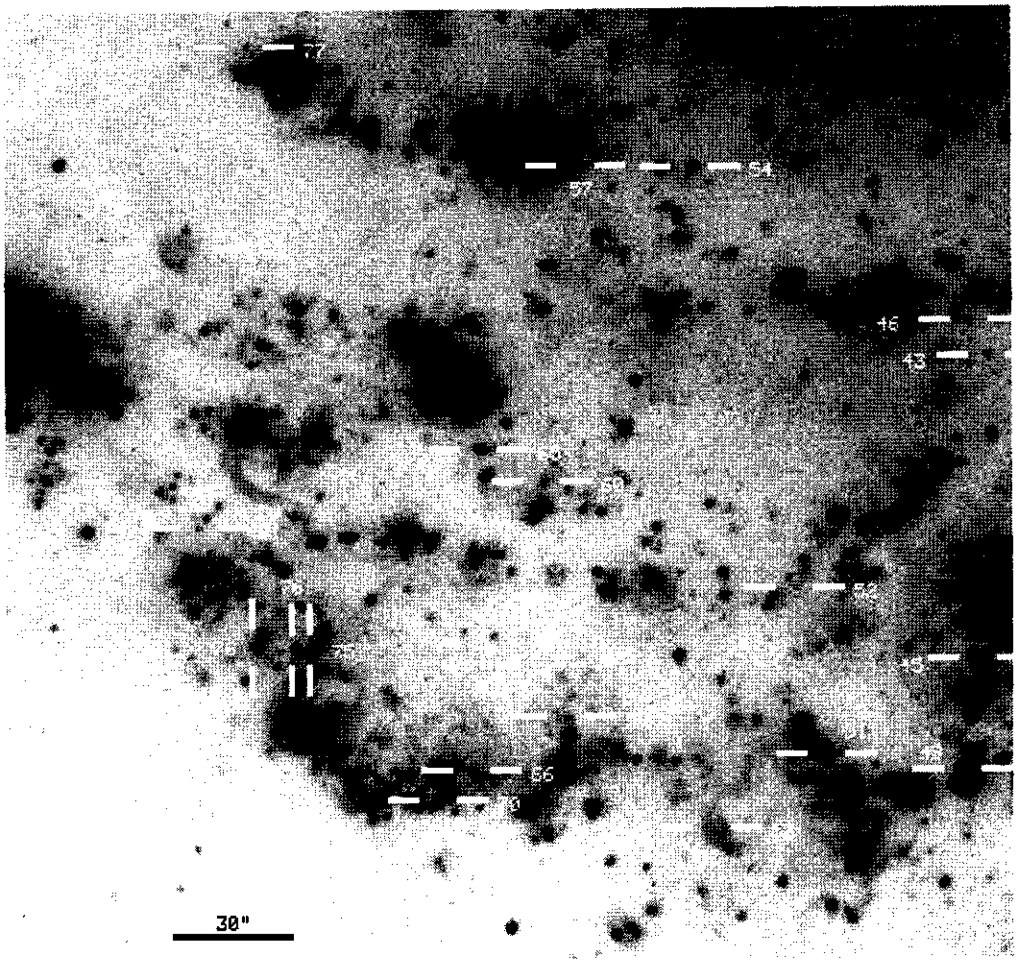

FIG. 21*d*

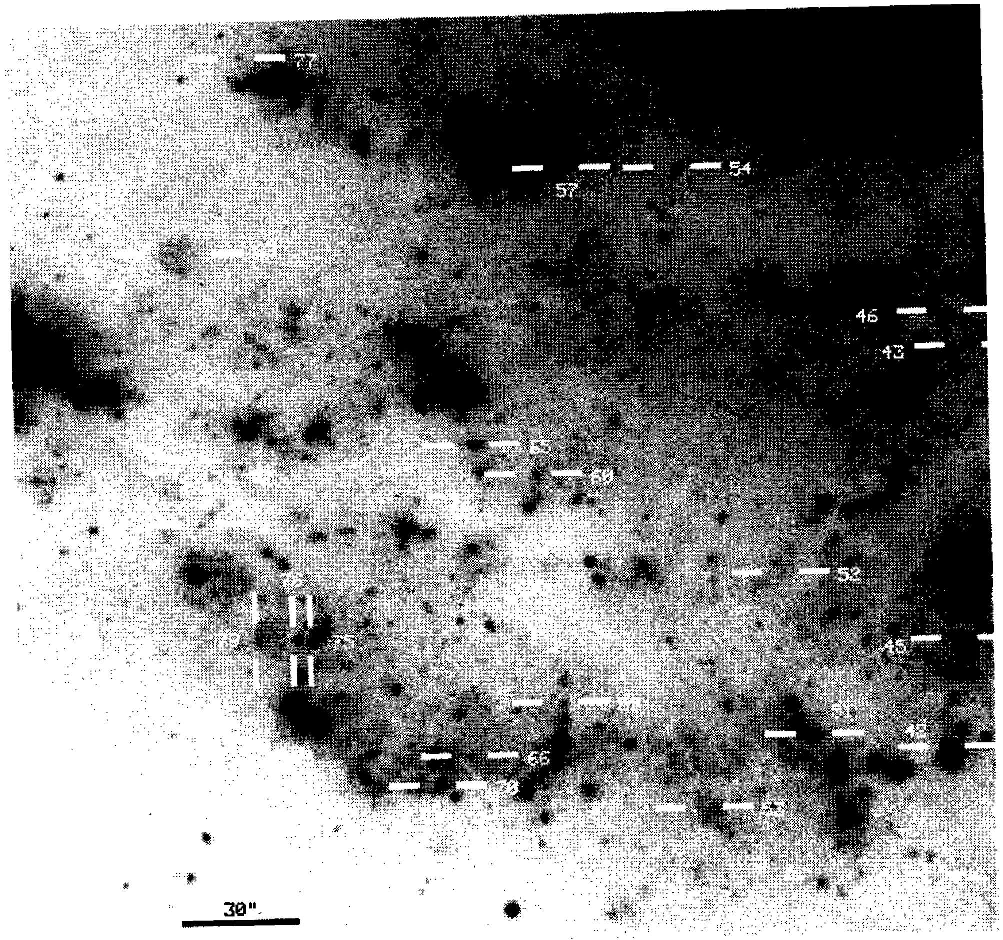

FIG. 21*e*

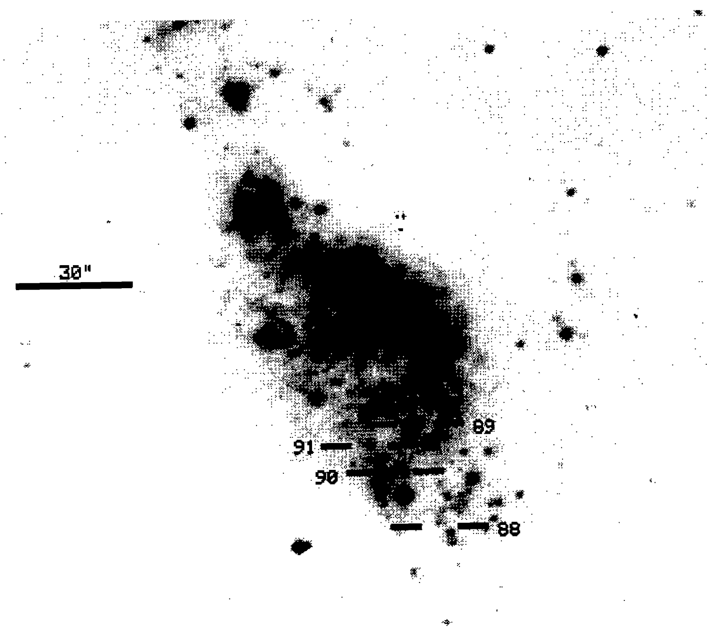

FIG. 21*f*

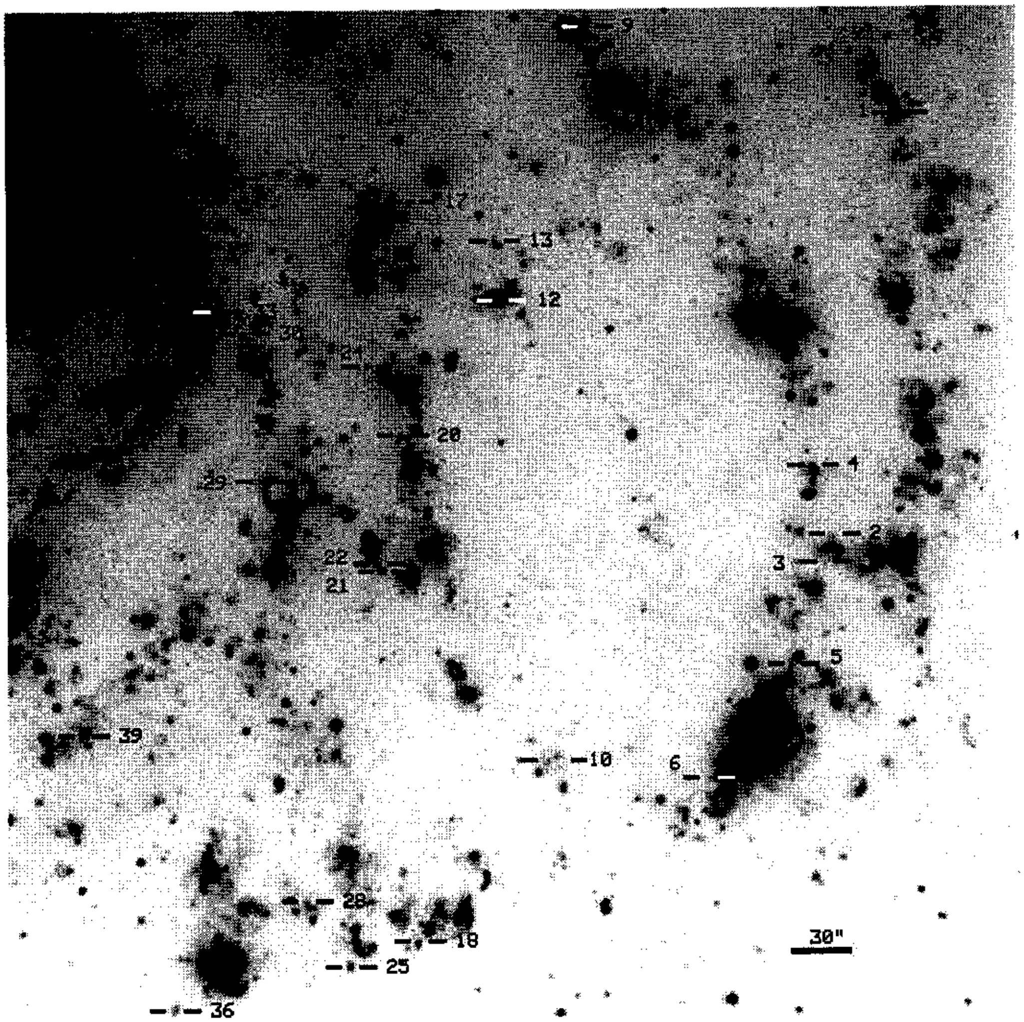

FIG. 22*a*

FIG. 22.—(*a*) Full-frame Hα image of the west field of M101 with SNRs marked. (*b*–*d*) Detailed finding charts of the SNRs detected in three sections of this field.

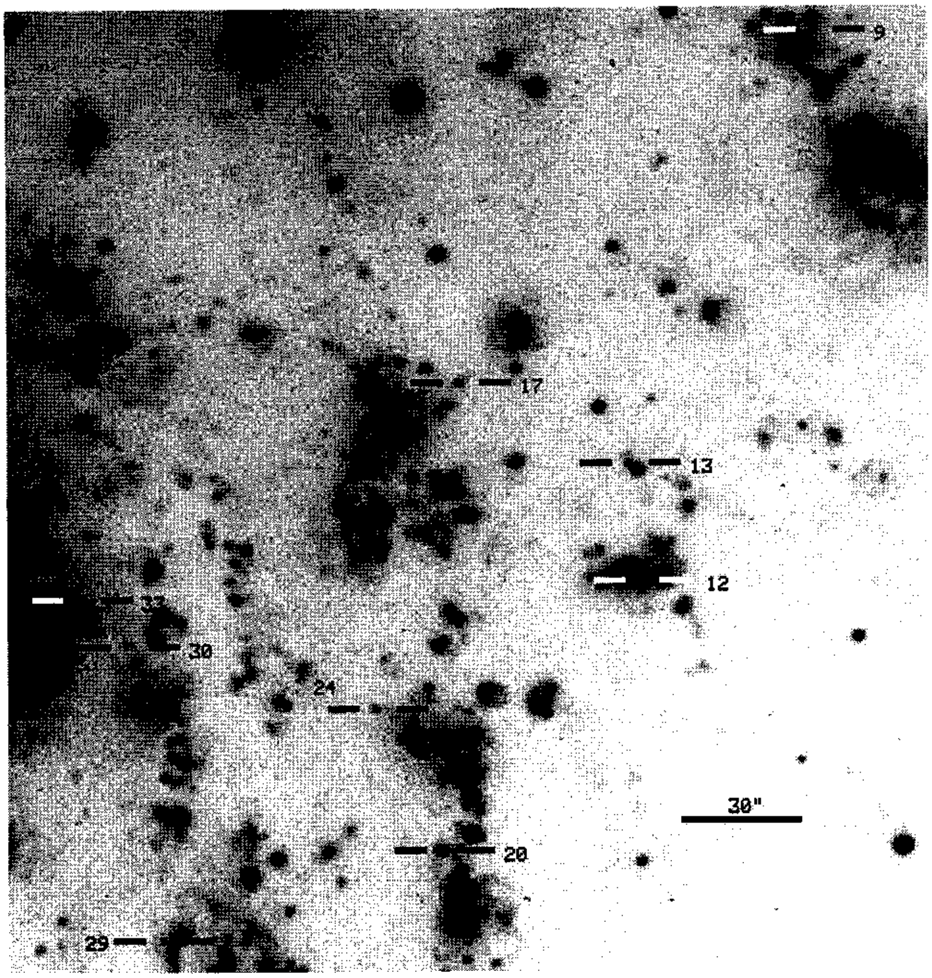

FIG. 22b

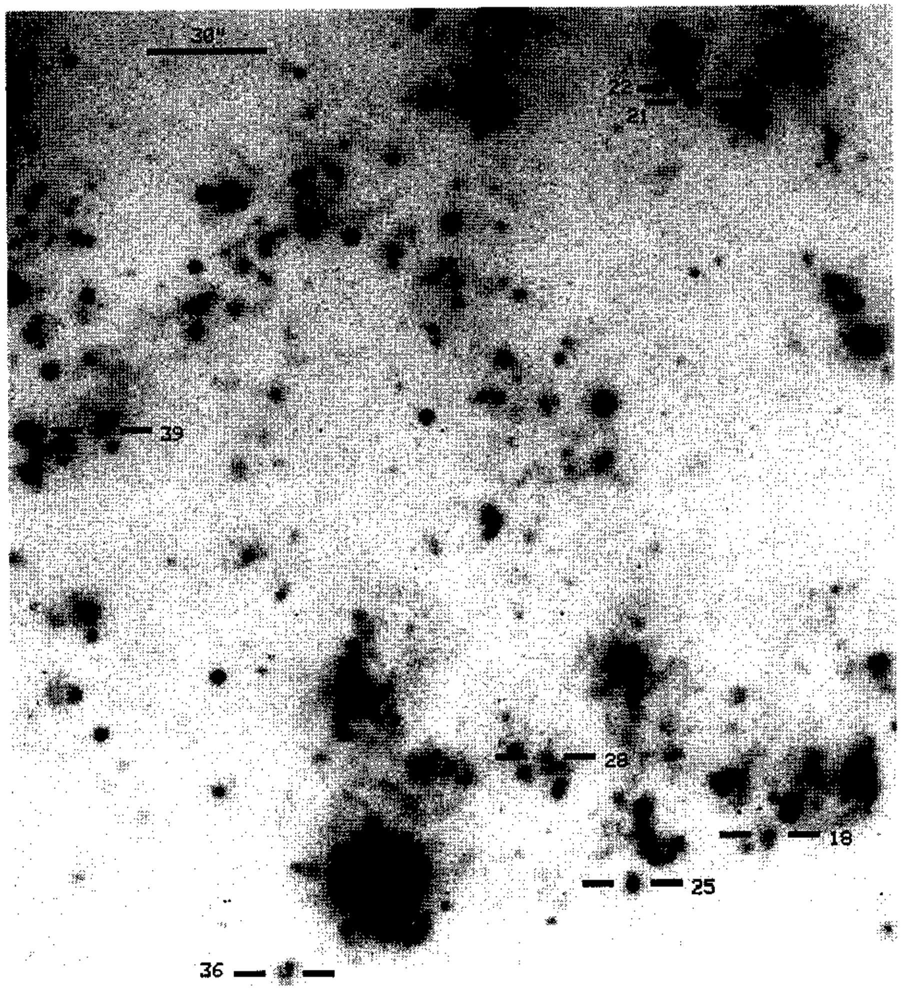

FIG. 22*c*

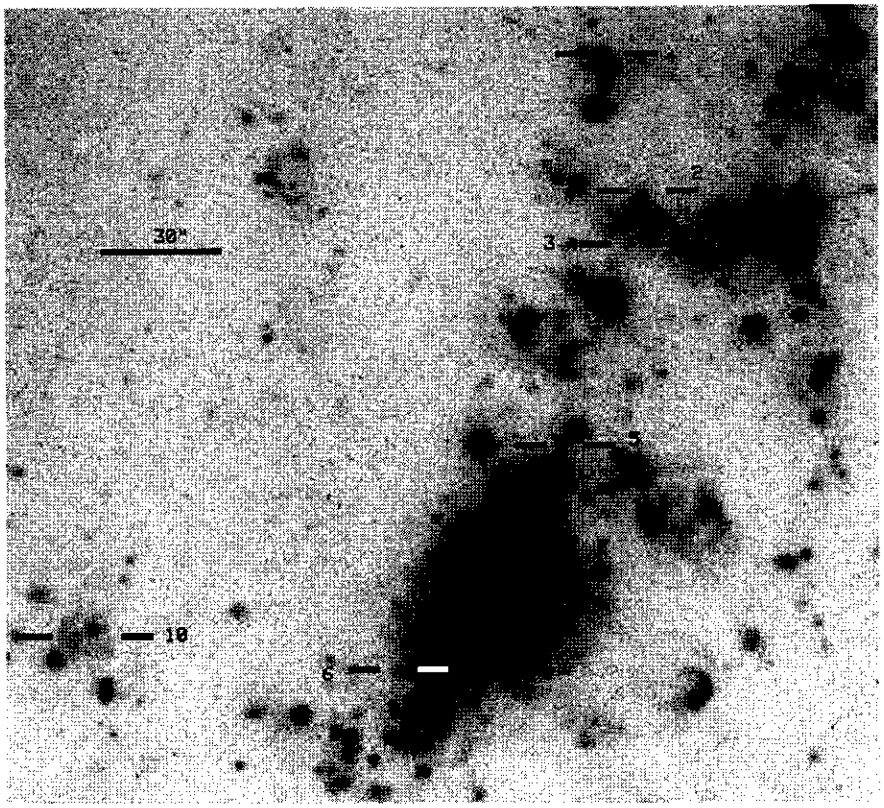

FIG. 22*d*

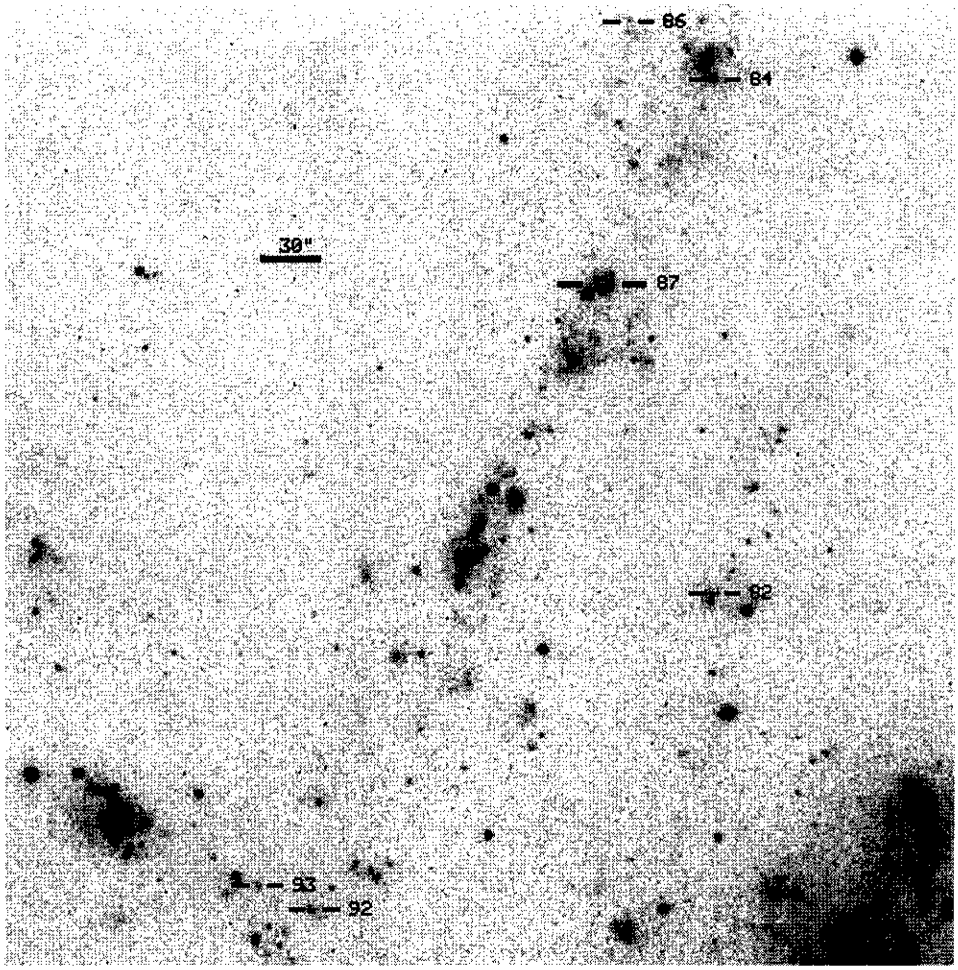

FIG. 23.—Full-frame Hα image of the northeast field of M101, with SNRs marked

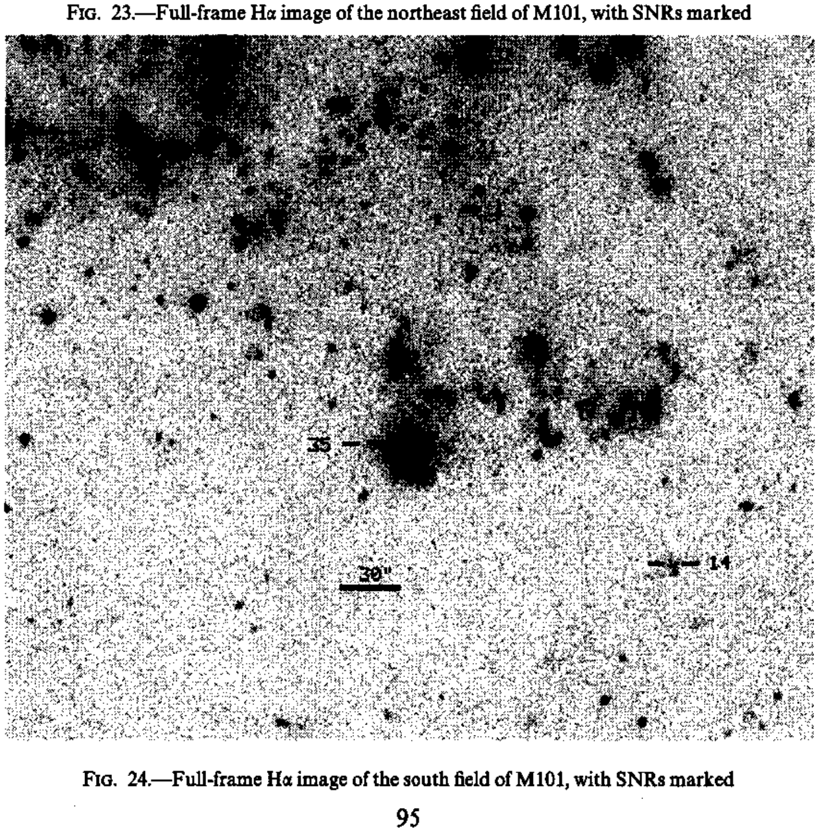

FIG. 24.—Full-frame Hα image of the south field of M101, with SNRs marked

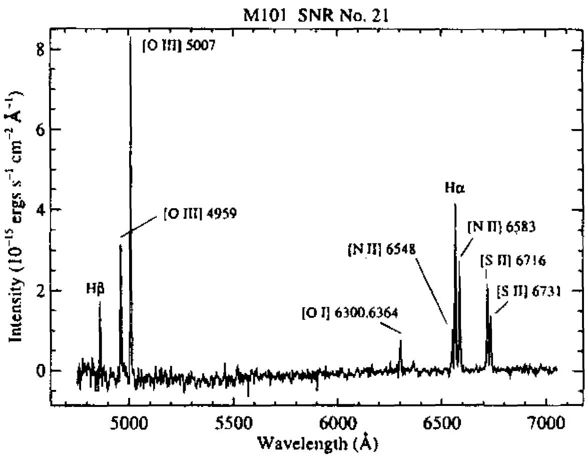

FIG. 25*a*

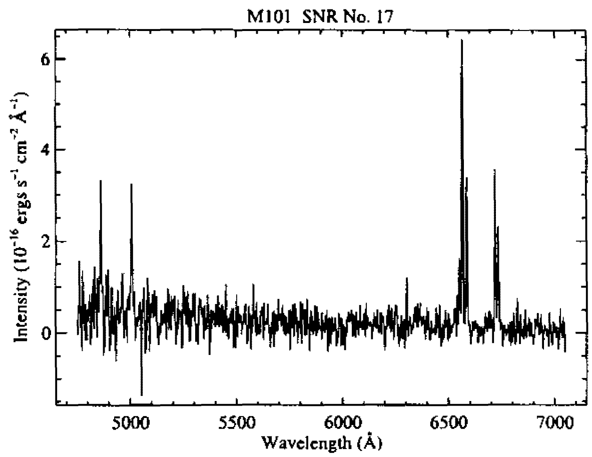

FIG. 25*b*

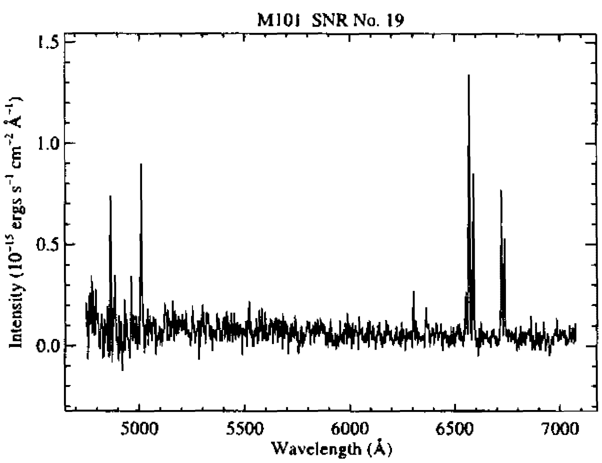

FIG. 25*c*

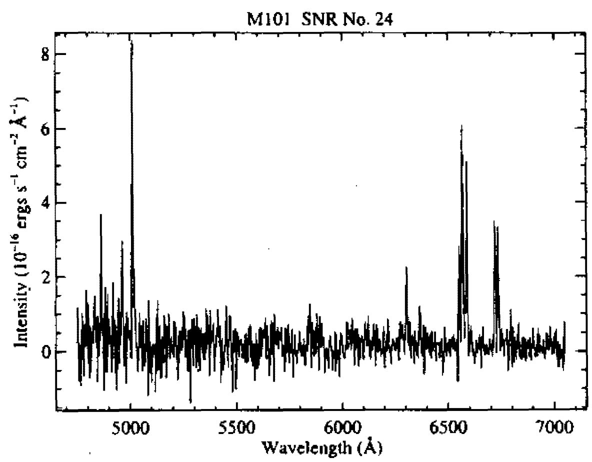

FIG. 25*d*

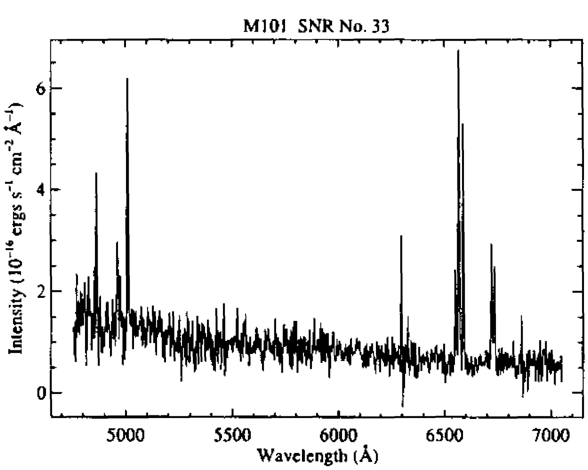

FIG. 25*e*

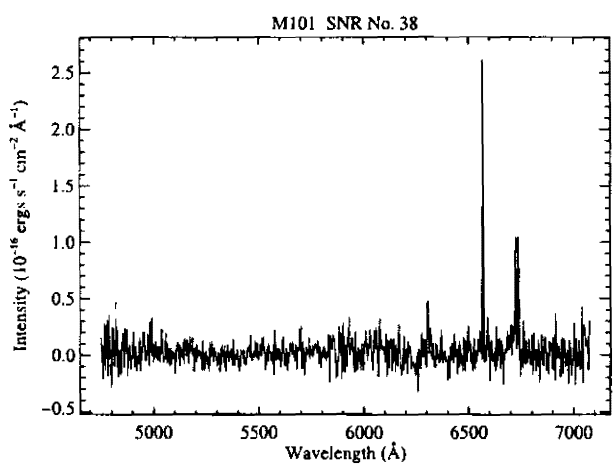

FIG. 25*f*

FIG. 25.—M101 SNR spectra

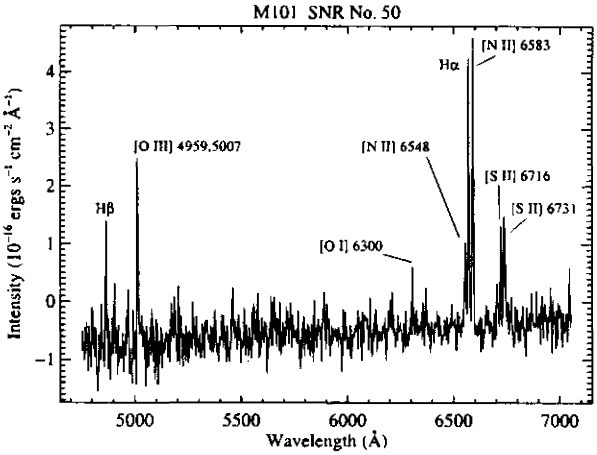

FIG. 25*g*

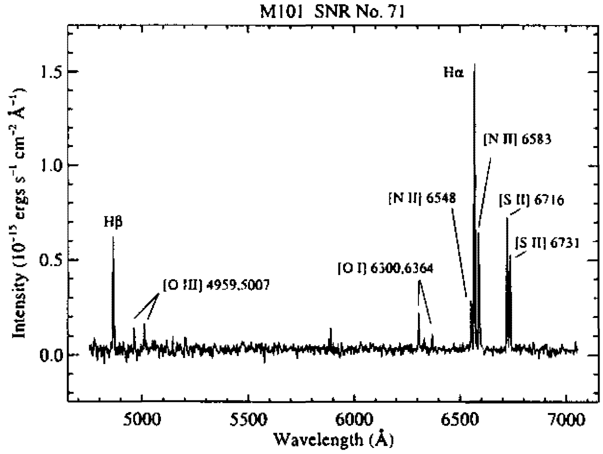

FIG. 25*h*

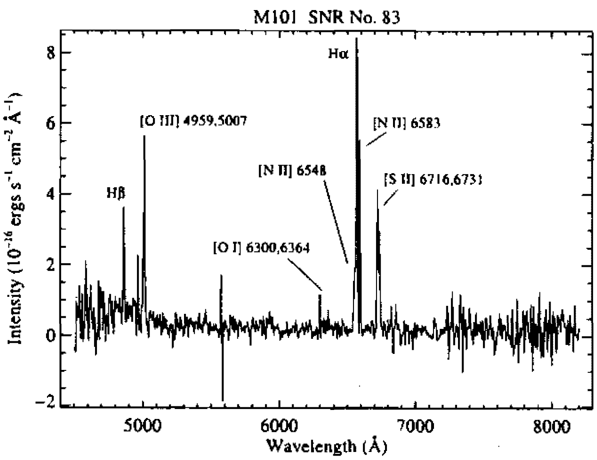

FIG. 25*i*

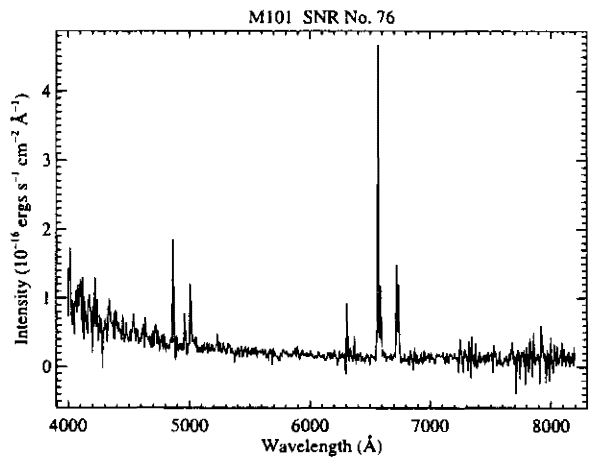

FIG. 25*j*

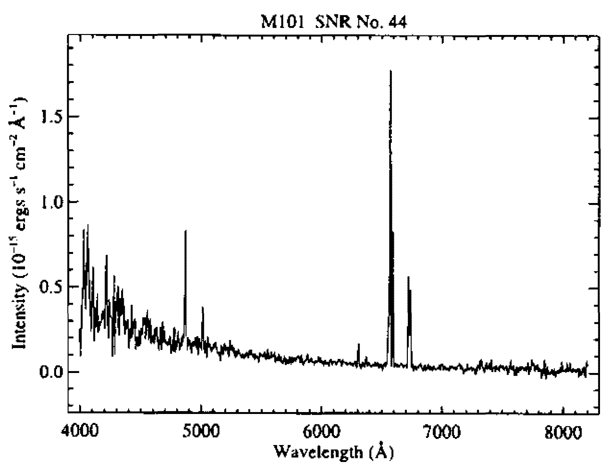

FIG. 25*k*

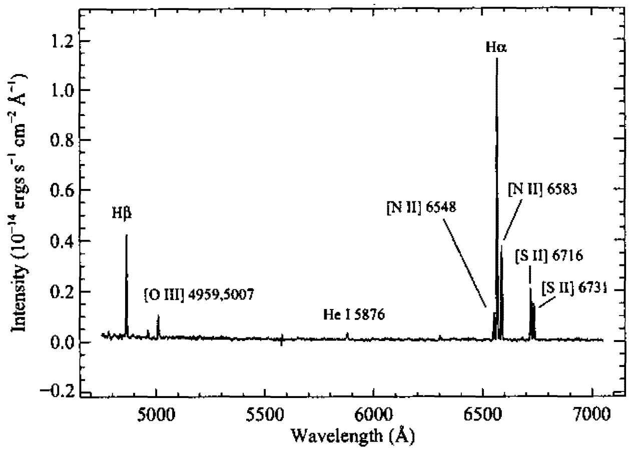

FIG. 26.—A typical M101 H II region spectrum, from the third bright H II region about 40″ northeast of M101 SNR No. 39

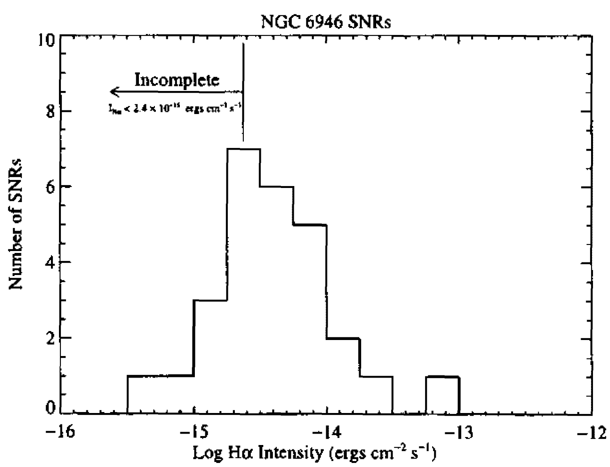

FIG. 27*a*

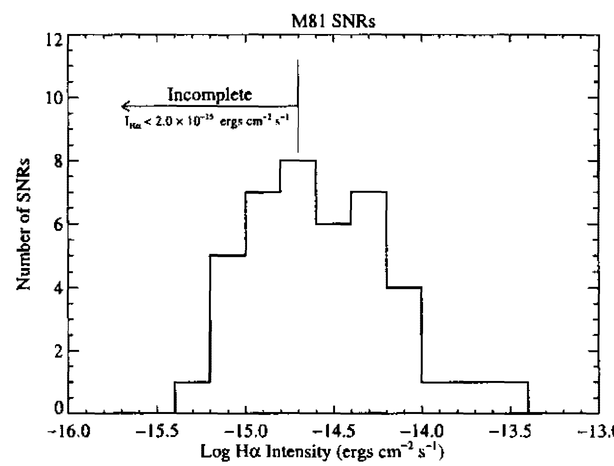

FIG. 27*b*

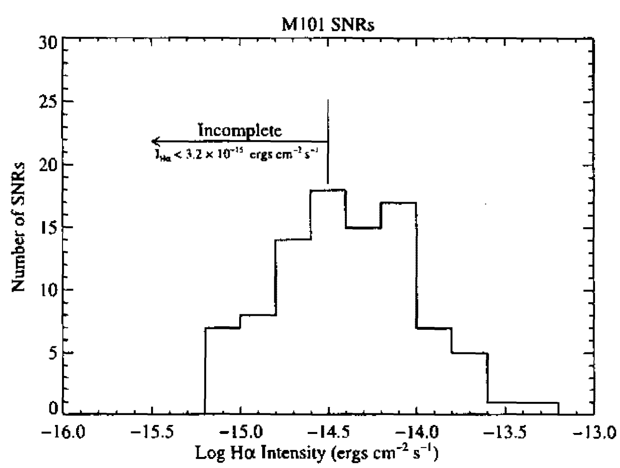

FIG. 27*c*

FIG. 27.—Histograms of SNR Hα intensity for three of the sample galaxies

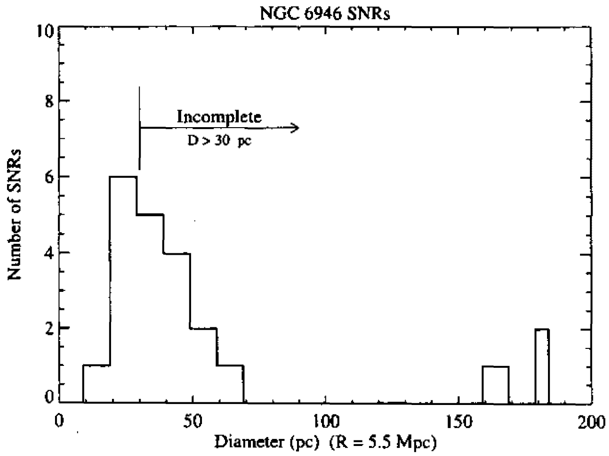

FIG. 28*a*

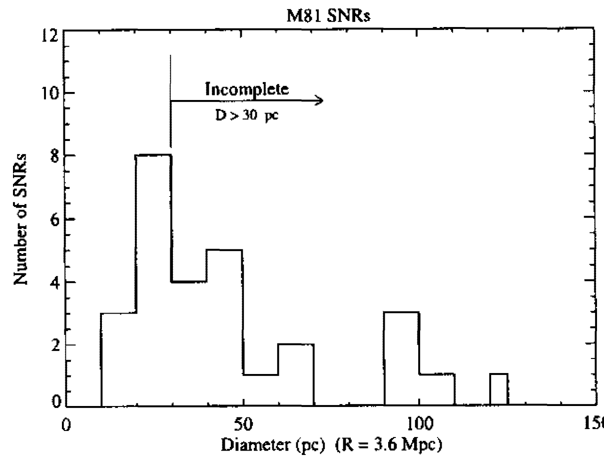

FIG. 28*b*

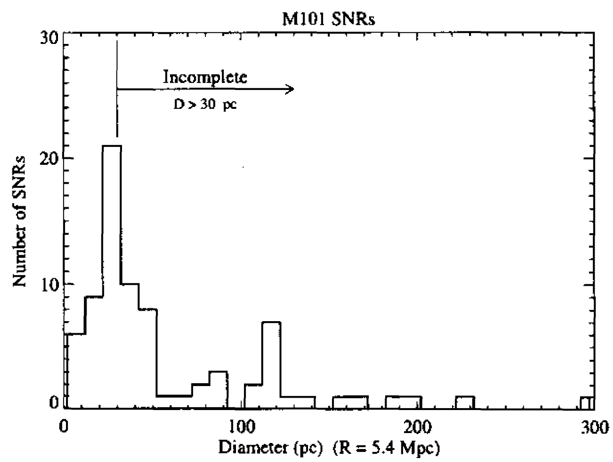

FIG. 28*c*

FIG. 28.—Histograms of SNR diameter

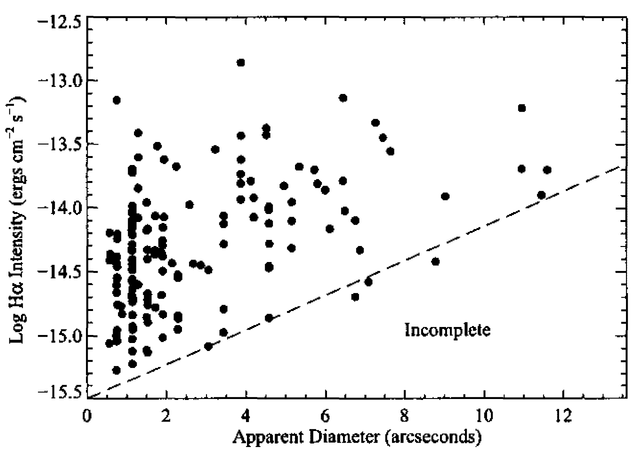

FIG. 29.—Plot of log I(Hα) vs. diameter (in arcseconds) for detected SNRs from all six galaxies combined. Approximate region of incompleteness is marked. Sample appears biased against detecting large, faint SNRs.

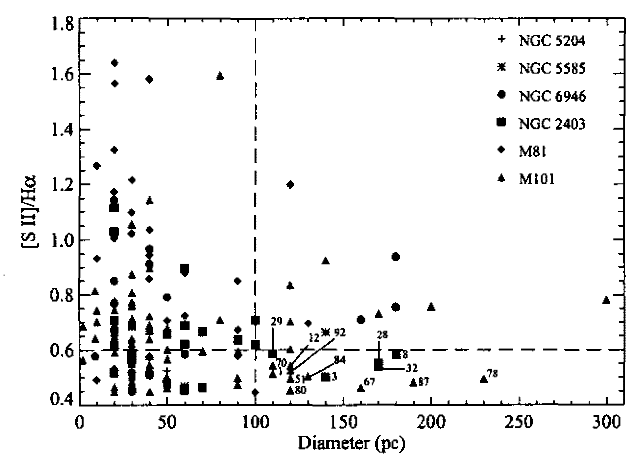

FIG. 30.—Ratio of [S II]/Hα vs. diameter for detected SNRs from all six galaxies combined. Objects with values also typical of stellar wind-shocked nebulae and diffuse ionized gas are shown marked by their SNR number on the bottom right.

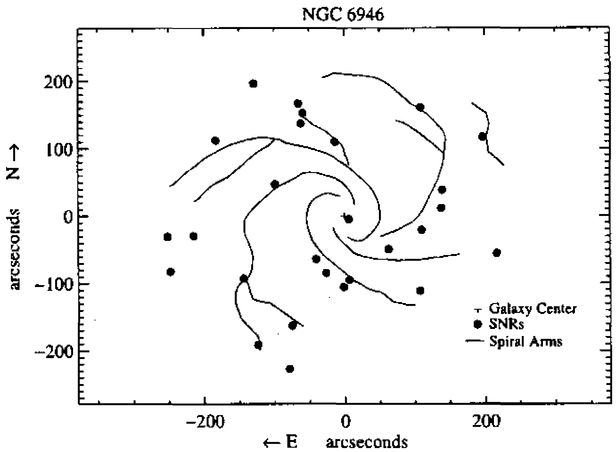

FIG. 31*a*

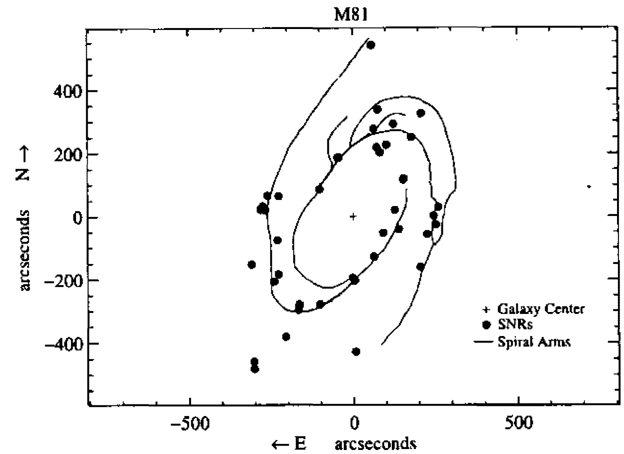

FIG. 31*b*

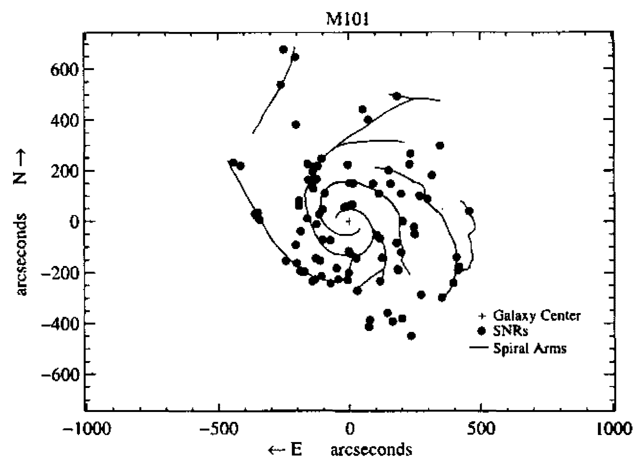

FIG. 31*c*

FIG. 31.—Observed spiral arm patterns and detected SNRs as they appear on the sky in three of our sample galaxies

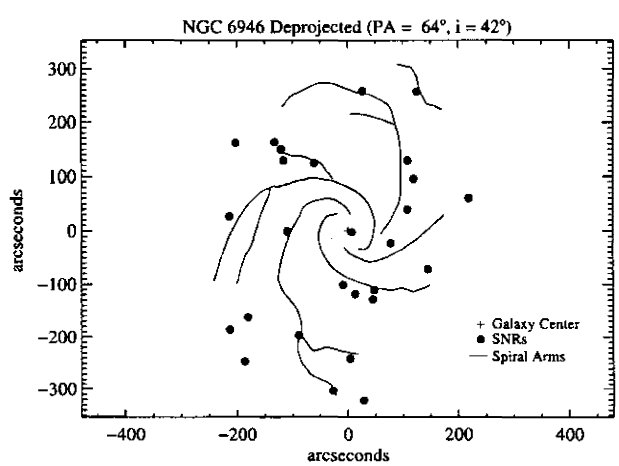

FIG. 32*a*

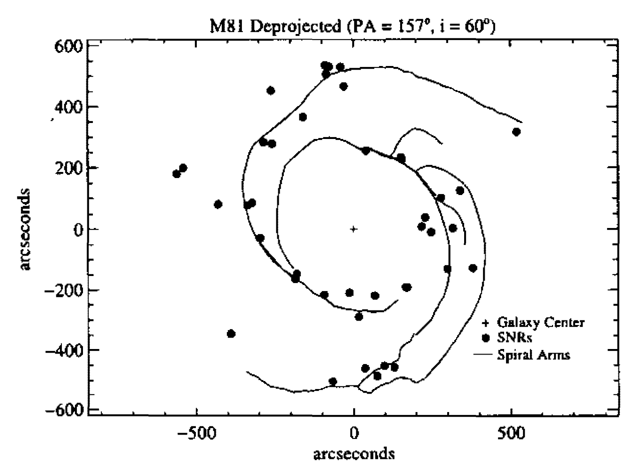

FIG. 32*b*

FIG. 32.—Observed spiral arm patterns and detected SNRs in (*a*) NGC 6946 and (*b*) M81 (from Fig. 31) deprojected to face-on

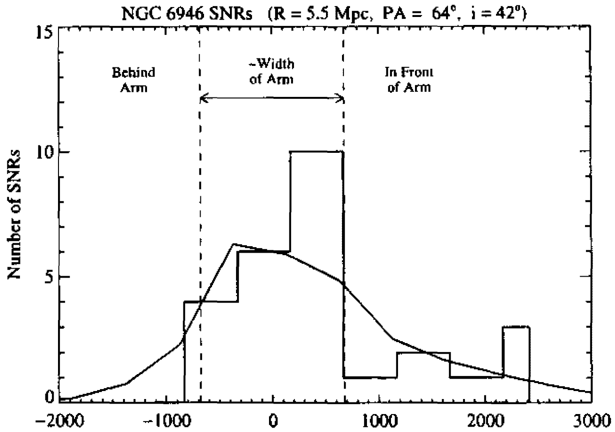

FIG. 33*a*

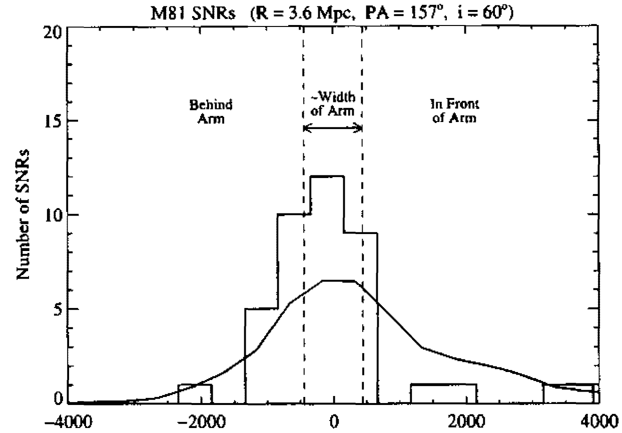

FIG. 33*b*

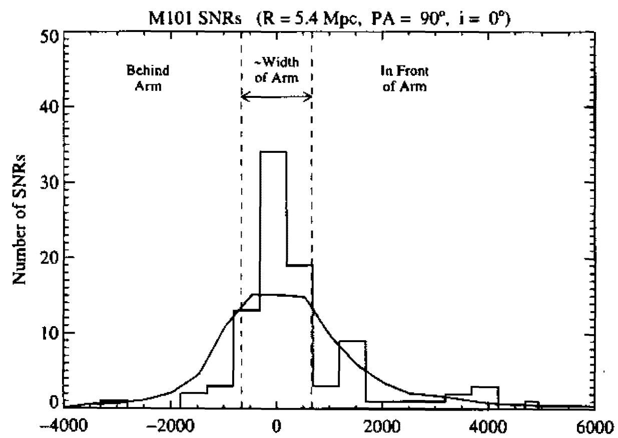

FIG. 33*c*

FIG. 33.—Distributions of detected SNRs relative to the spiral arms shown in Fig. 32. The spiral arm width is an average value for each galaxy. A SNR "behind" a spiral arm is located between the arm and the galaxy's center. The solid lines overplotting the histograms of the observed distributions are random distributions of 10,000 simulated SNRs, normalized to the total number of SNRs detected in each galaxy.

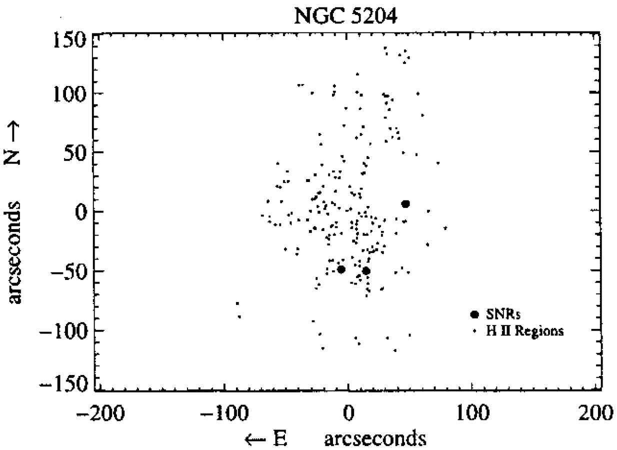

FIG. 34*a*

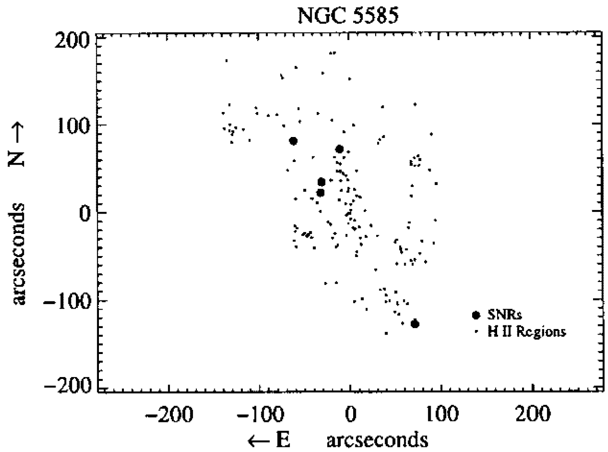

FIG. 34*b*

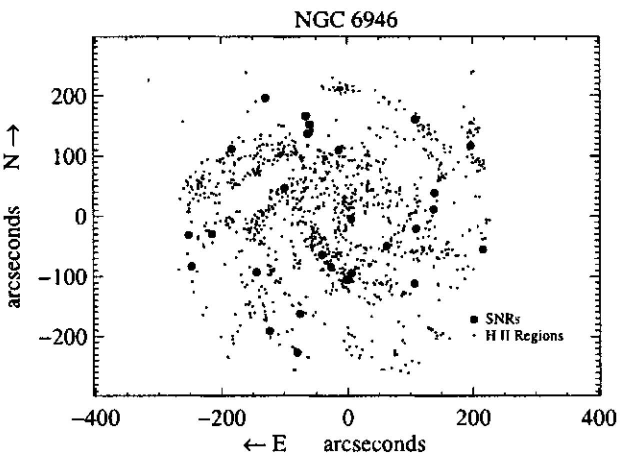

FIG. 34*c*

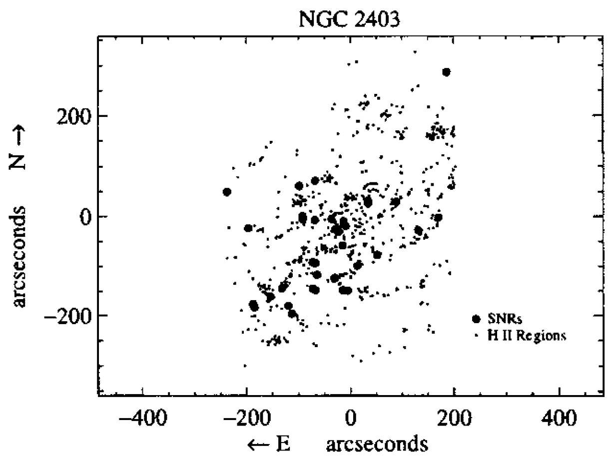

FIG. 34*d*

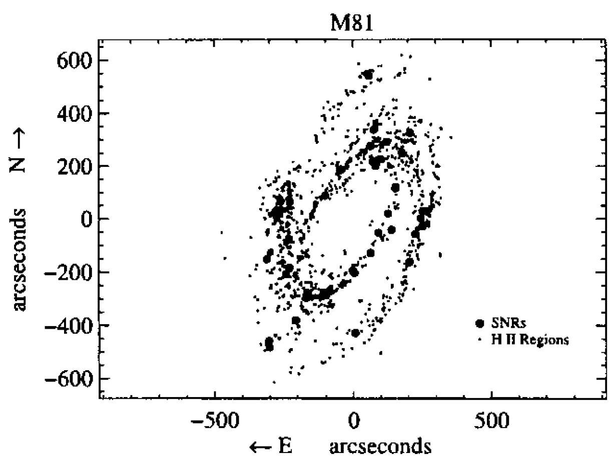

FIG. 34*e*

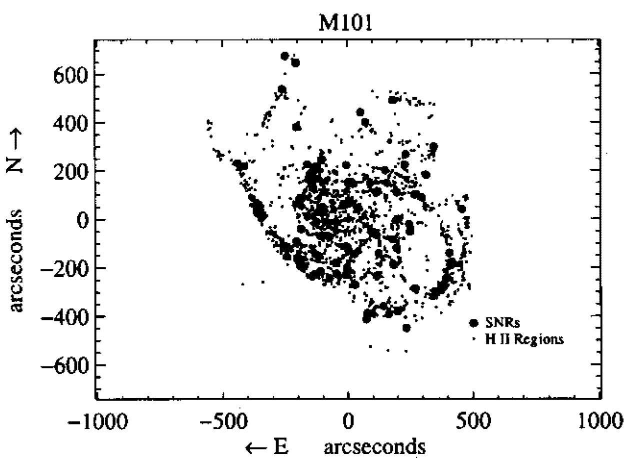

FIG. 34*f*

FIG. 34.—Plots of the six sample galaxies with detected SNRs and H II regions as they appear on the sky. An H II region is represented by one or more small circles.

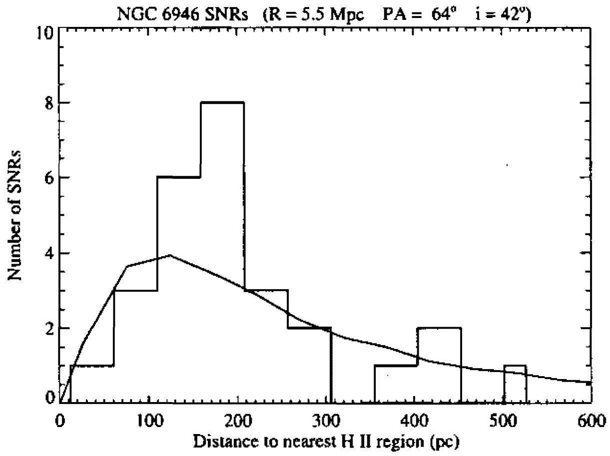

FIG. 35*a*

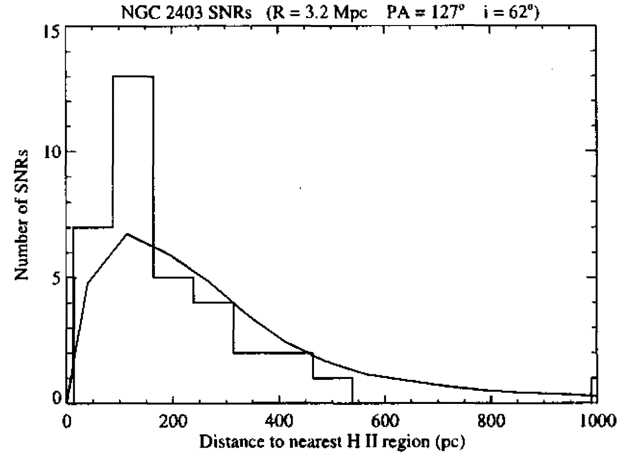

FIG. 35*b*

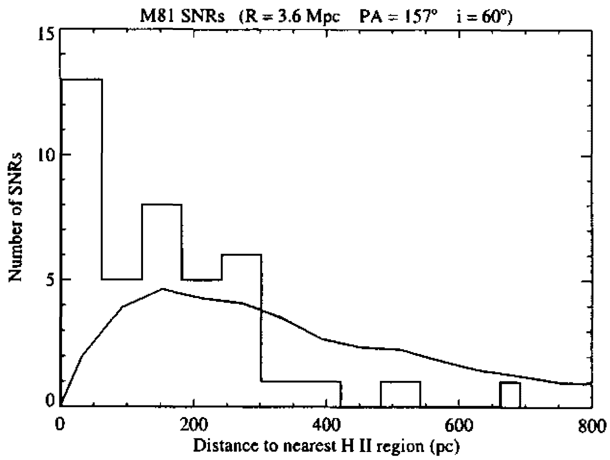

FIG. 35*c*

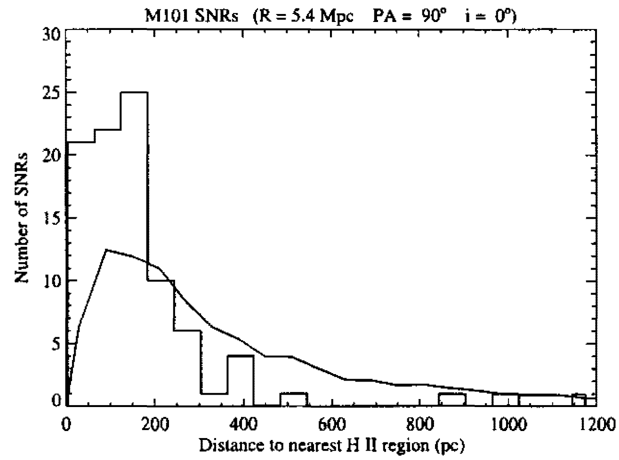

FIG. 35*d*

FIG. 35.—Distributions of detected SNRs relative to the H II regions shown in Fig. 34. The solid lines overplotting the histograms of the observed distributions are random distributions of 10,000 simulated SNRs, normalized to the total number of SNRs detected in each galaxy.

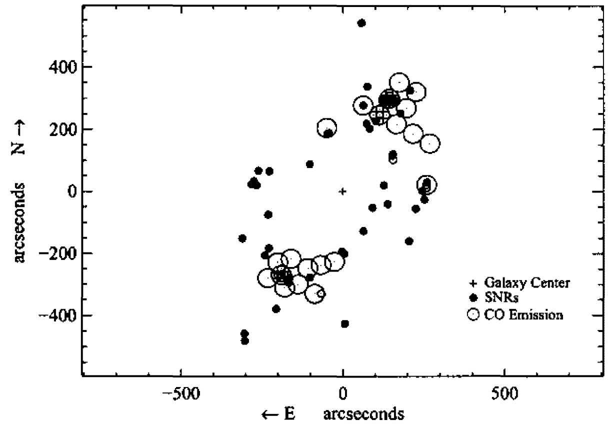

FIG. 36*a*

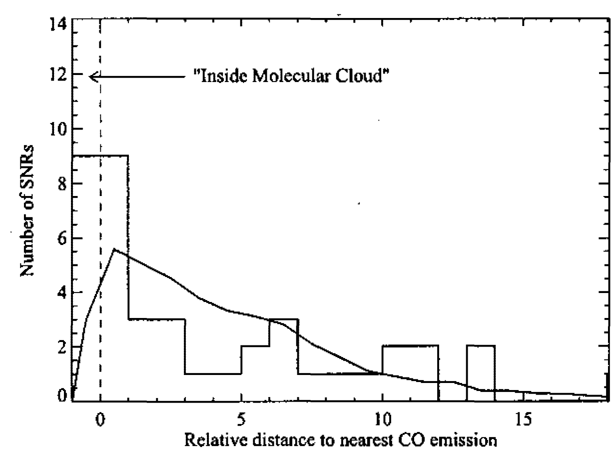

FIG. 36*b*

FIG. 36.—(*a*) Regions of CO detection in M81 from Brouillet et al. 1991, along with our detected SNRs as they appear on the sky. The diameter of each circle denoting a CO emission region is equal to the HPBW of the observation. (*b*) Distribution of detected SNRs relative to the molecular clouds (CO emission regions). Relative distance to nearest CO emission = (deprojected distance to nearest edge of CO emission region)/($\frac{1}{2}$ HPBW). The solid line overplotting the histogram of the observed distribution is a random distribution of 10,000 simulated SNRs, normalized to the total number of SNRs detected in M81.

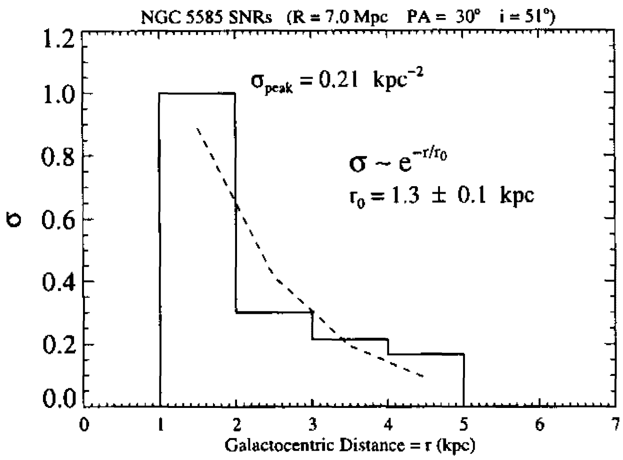

FIG. 37*a*

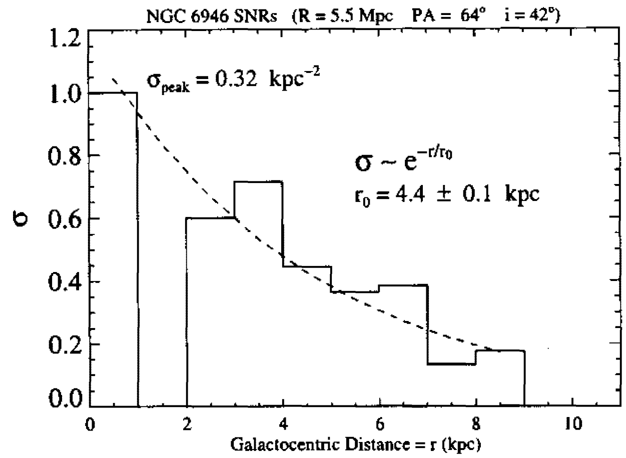

FIG. 37*b*

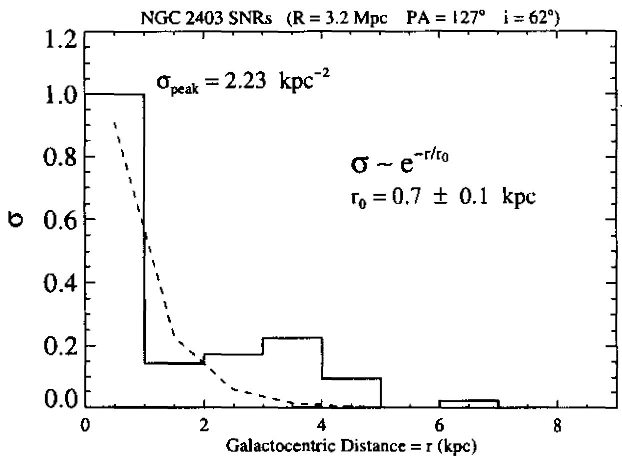

FIG. 37*c*

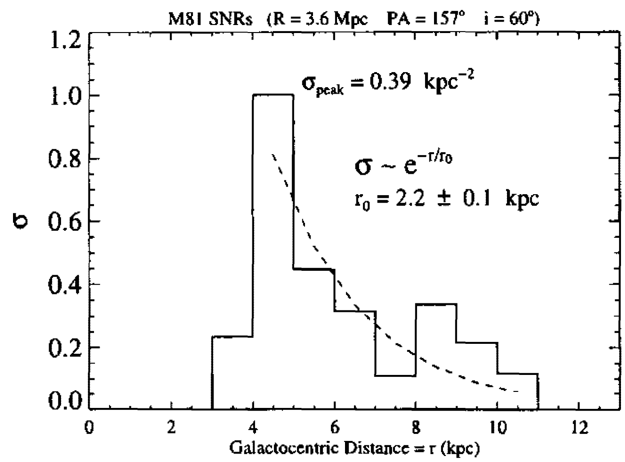

FIG. 37*d*

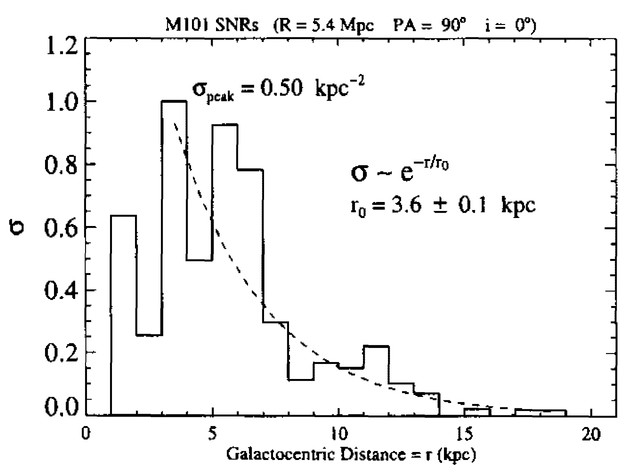

FIG. 37*e*

FIG. 37.—Radial distributions of normalized surface density of detected SNRs in five of our sample galaxies. The peak value of surface density in kiloparsecs^{-2} is indicated on each plot. The dashed curve overplotting each distribution is a nonlinear least-squares fit to $\sigma \sim e^{-r/r_0}$, where r_0 is the exponential scale length in kiloparsecs, whose solution also is marked on each plot. The fit is only from the main peak outward.

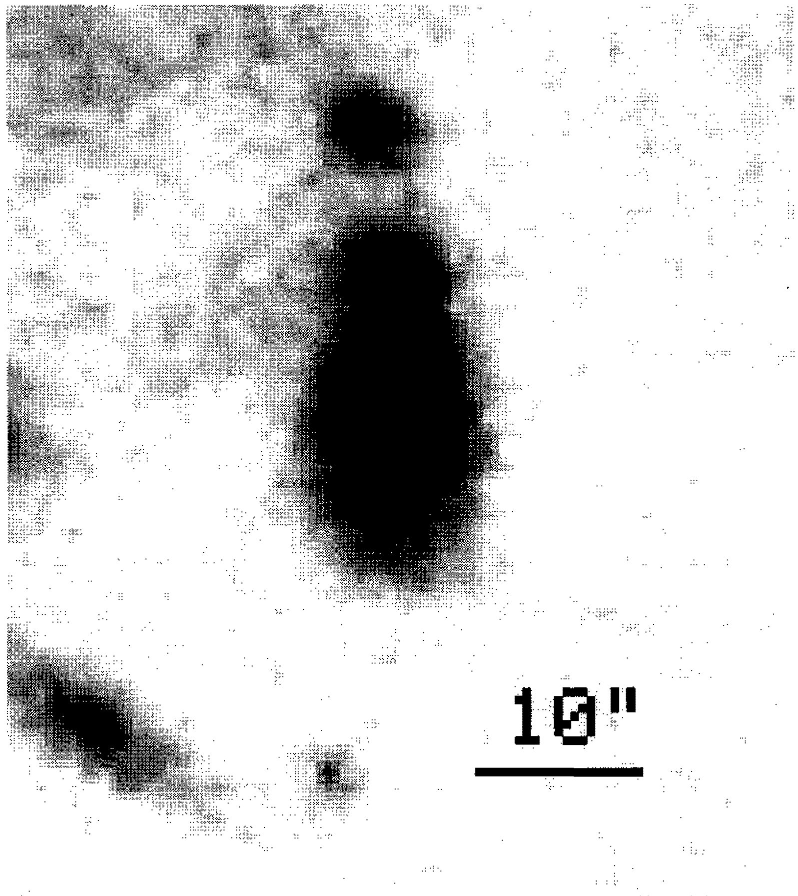

FIG. 38.—Detail of the Hα image of NGC 5585 from Fig. 6, showing NGC 5585 SNR No. 1. North is up, east to the left. The bright, compact object on the very northern edge of SNR No. 1 is an H II region. Because a SNR will expand more rapidly into a less dense region, the unusual size of this remnant may be a result of its expanding into a region of lower ISM density: SNR No. 1 is located at a galactocentric distance just past the beginning of a significant decrease in H I surface density in NGC 5585 (Fig. 6 of Cote et al. 1991). Note that the remnant appears slightly brighter on its eastern and northeastern limbs, possibly indicating that it encounters regions of higher density at those points.

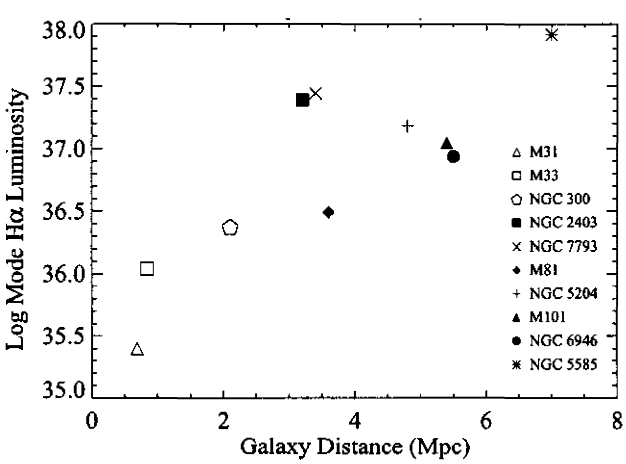

FIG. 39.—Plot of log $L(H\alpha)_{mode}$ for each SNR sample vs. galaxy distance. Units of $L(H\alpha)_{mode}$ are ergs s^{-1}. The apparent trend of higher $L(H\alpha)_{mode}$ with greater distance is a selection effect: fainter SNRs are more difficult to detect in more distant galaxies, and therefore $L(H\alpha)_{mode}$ shifts to higher values for the more distant SNR samples.

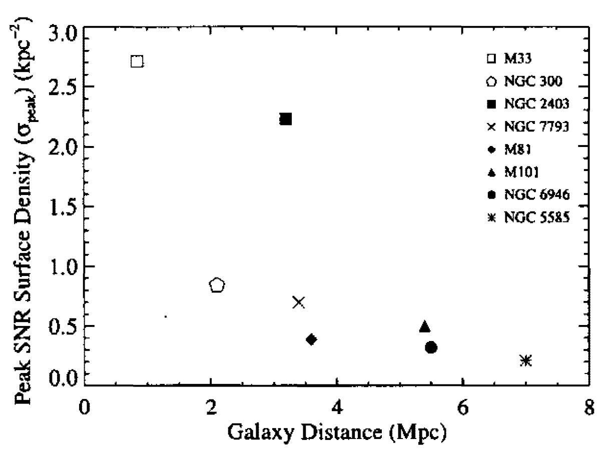

FIG. 40.—Peak SNR surface density in each galaxy (σ_{peak}) vs. galaxy distance. The general trend of larger σ_{peak} for nearer galaxies is a selection effect: in a nearer galaxy, we are likely to detect and resolve more SNRs in confused regions near the galaxy's center, giving a higher σ_{peak}.

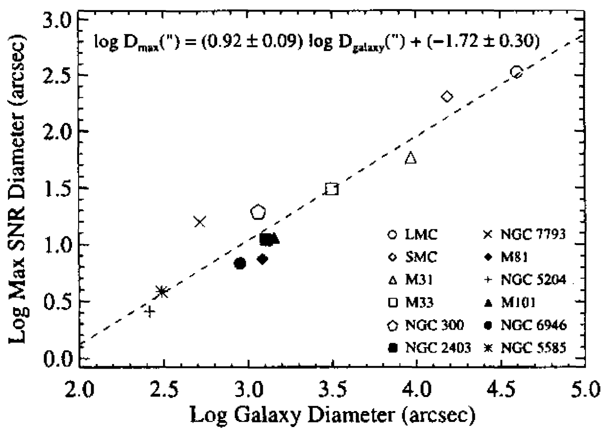

FIG. 41.—Plot of log D_{max} (arcseconds) vs. log D_{galaxy} (arcseconds) for the SNR samples. The dashed line is a least-squares fit to the data; the errors shown are only those in the fit. The correlation seems to indicate that, in ground-based optical observations, the maximum observable SNR diameter is determined by the diameter of the galaxy.

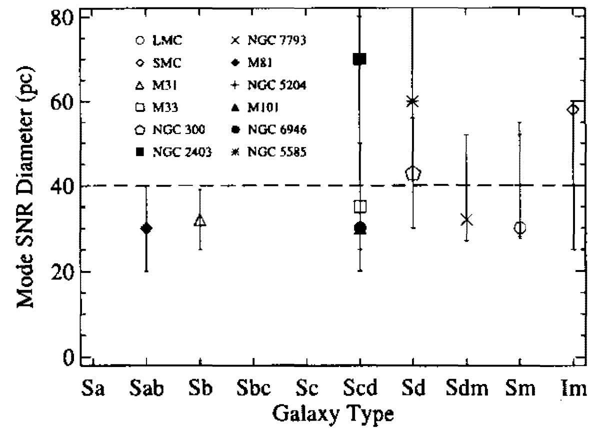

FIG. 44.—Plot of D_{mode} (pc) vs. galaxy type for the SNR samples. The dashed line is at the value of $D_{mode} \approx 40$ pc found in Fig. 43. Error bars were obtained by examination of the SNR diameter histograms for each galaxy sample.

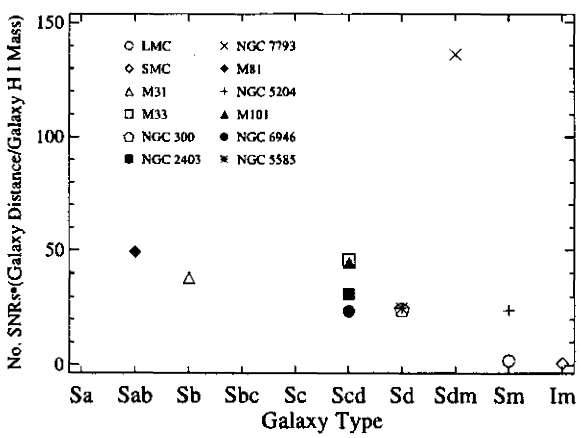

FIG. 42.—Number of SNRs detected in each galaxy per galaxy H I mass (multiplied by galaxy distance), as a function of galaxy type. Except for NGC 7793, the plot seems to indicate that fewer SNRs per unit galaxy H I mass (times galaxy distance) are detected in later type galaxies.

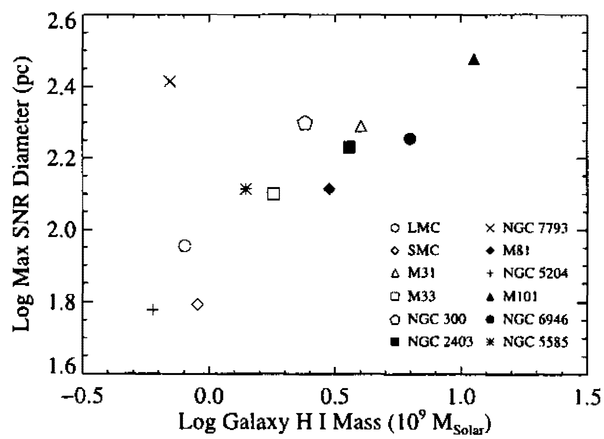

FIG. 45.—Plot of log D_{max} (pc) vs. log M(H I) ($10^9\ M_\odot$) for the SNR samples. With, again, the exception of NGC 7793, the data seem to show a correlation of D_{max} with M(H I). Such a trend may occur because galaxies with a denser ISM (as traced by the H I mass) provide an environment in which larger detectable SNRs can evolve.

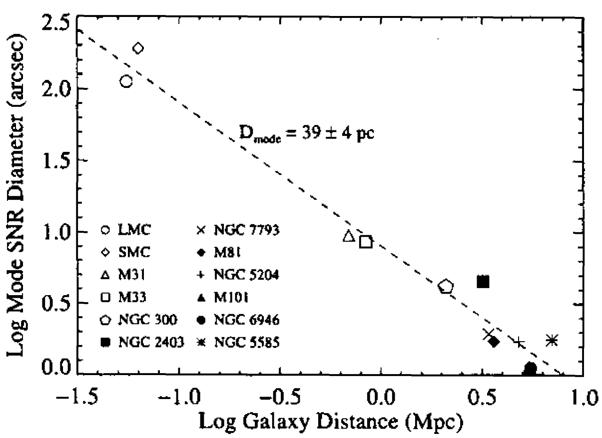

FIG. 43.—Plot of log D_{mode} (arcseconds) vs. log R (Mpc) for the SNR samples. The data point for M101 nearly overlaps that for NGC 6946. The dashed line is a least-squares fit to the data and has a slope of −1 and a y-intercept that gives $D_{mode} \approx 40$ pc for a SNR sample in a spiral galaxy.

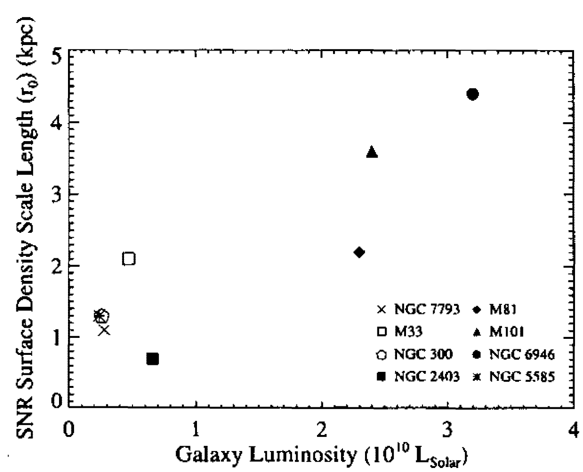

FIG. 46.—SNR surface density scale length r_0 (kpc) of the SNR samples as a function of galaxy luminosity ($10^{10}\ L_\odot$). There seems to be a weak trend indicating larger r_0 at higher galaxy luminosity.

REFERENCES

Balick, B., & Heckman, T. 1978, ApJ, 226, L7
Barbon, R., Cappellaro, E., & Turatto, M. 1989, A&AS, 81, 421
Bartunov, O. S., Makarova, I. N., & Tsvetkov, D. Yu. 1992, A&A, 264, 428
Bartunov, O. S., Tsvetkov, D. Yu., & Filimonova, I. V. 1994, PASP, 106, 1276
Bash, F. N., & Kaufman, M. 1986, ApJ, 310, 621
Blair, W. P., & Davidsen, A. F. 1993, PASP, 105, 494
Blair, W. P., & Fesen, R. A. 1994, ApJ, 424, L103
Blair, W. P., & Kirshner, R. P. 1985, ApJ, 289, 582
Blair, W. P., Kirshner, R. P., & Chevalier, R. A. 1981, ApJ, 247, 879
———. 1982, ApJ, 254, 50
Blair, W. P., Kirshner, R. P., & Winkler, P. F. 1983, ApJ, 272, 84
Blair, W. P., & Long, K. S. 1997, ApJS, 108, 261
Blair, W. P., Raymond, J. C., Fesen, R. A., & Gull, T. R. 1984, ApJ, 279, 708
Bonnarel, F., Boulesteix, J., & Marcelin, M. 1986, A&AS, 66, 149
Braun, R., Goss, W. M., & Lyne, A. G. 1989, ApJ, 340, 355
Braun, R., & Walterbos, R. A. M. 1993, A&AS, 98, 327
Brouillet, N., Baudry, A., Combes, F., Kaufman, M., & Bash, F. 1991, A&A, 242, 35
Burstein, D., & Heiles, C. 1978, ApJ, 225, 40
Chu, Y.-H., Chang, H.-W., Su, Y.-L., & Mac Low, M.-M. 1995, ApJ, 450, 157
Chu, Y.-H., & Kennicutt, R. C. 1986, ApJ, 311, 85
———. 1988a, AJ, 95, 1111
———. 1988b, AJ, 96, 1874
Chu, Y.-H., Mac Low, M.-M., Garcia-Segura, G., Wakker, B., & Kennicutt, R. C. 1993, ApJ, 414, 213
Cohen, R. S., Dame, T. M., Garay, G., Montani, J., Rubio, M., & Thaddeus, P. 1988, ApJ, 331, L95
Cote, S., Carignan, C., & Sancisi, R. 1991, AJ, 102, 904
De Robertis, M. M., Dufour, R., & Hunt, R. 1987, JRASC, 81, 195
de Vaucouleurs, G., de Vaucouleurs, A., Corwin, H. G., Jr., Buta, R. J., Paturel, G., & Fouqué, P. 1991, Third Reference Catalog of Bright Galaxies (New York: Springer)
D'Odorico, S., Dopita, M. A., & Benvenuti, P. 1980, A&AS, 40, 67
Dopita, M. A., Binette, L., D'Odorico, S., & Benvenuti, P. 1984, ApJ, 276, 653
Fabbiano, G. 1988, ApJ, 325, 544
Fabbiano, G., Kim, D. W., & Trinchieri, G. 1992, ApJS, 80, 531
Fesen, R. A. 1993, ApJ, 413, L109
Fesen, R. A., Blair, W. P., & Kirshner, R. P. 1985, ApJ, 292, 29
Finn, R. A., Fesen, R. A., Darling, G. W., Thorstensen, J. T., & Worthey, G. S. 1995, AJ, 110, 300
Forest, T. A., Spenny, D. L., & Johnson, R. W. 1988, PASP, 100, 683
Freedman, W. L., et al. 1994, ApJ, 427, 628
Freedman, W. L., & Madore, B. F. 1988, ApJ, 332, L63
Garcia-Gomez, C., & Athanassoula, E. 1991, A&AS, 89, 159
Gordon, S. M. 1994, Ph.D. thesis, Univ. New Mexico
Gordon, S. M., Kirshner, R. P., Duric, N., & Long, K. S. 1993, ApJ, 418, 743
Green, D. A. 1991, PASP, 103, 209
Hodge, P. W., & Kennicutt, R. C. 1983, ApJ, 267, 563
Huang, Y.-L. 1987, PASP, 99, 461
Hunter, D. A. 1994, AJ, 107, 565
Kaufman, M., Bash, F. N., Hine, B., Rots, A. H., Elmegreen, D. M., & Hodge, P. W. 1989, ApJ, 345, 674
Kaufman, M., Bash, F. N., Kennicutt, R. C., & Hodge, P. W. 1987, ApJ, 319, 61
Kirshner, R. P., & Blair, W. P. 1980, ApJ, 236, 135
Kumar, C. K. 1976, PASP, 88, 323
Long, K. S. 1985, Space Sci. Rev., 40, 531
Long, K. S., Blair, W. P., Kirshner, R. P., & Winkler, P. F. 1990, ApJS, 72, 61
Lozinskaya, T. A. 1992, Supernovae and Stellar Wind in the Interstellar Medium (New York: AIP)
Magnier, E. A., Prins, S., van Paradijs, J., Lewin, W. H. G., Supper, R., Hasinger, G., Pietsch, W., & Trümper, J. 1995, A&AS, 114, 215
Massey, P., Strobel, K., Barnes, J. V., & Anderson, E. 1988, ApJ, 328, 315
Mathewson, D. S., & Clarke, J. N. 1972, ApJ, 178, L105
———. 1973a, ApJ, 180, 725
———. 1973b, ApJ, 182, 697
Mathewson, D. S., Ford, V. L., Dopita, M. A., Tuohy, I. R., Long, K. S., & Helfand, D. J. 1983, ApJS, 51, 345
Mathewson, D. S., Ford, V. L., Dopita, M. A., Tuohy, I. R., Mills, B. Y., & Turtle, A. J. 1984, ApJS, 55, 189
Mathewson, D. S., Ford, V. L., Tuohy, I. R., Mills, B. Y., Turtle, A. J., & Helfand, D. J. 1985, ApJS, 58, 197
Matonick, D. M. 1997, Ph.D. thesis, Dartmouth College
Matonick, D. M., Fesen, R. A., Blair, W. P., & Long, K. S. 1997, ApJS, 113, in press
Maza, J., & van den Bergh, S. 1976, ApJ, 204, 519
McCall, M. L., Rybski, P. M., & Shields, G. A. 1985, ApJS, 57, 1
McCray, R., & Kafatos, M. 1987, ApJ, 317, 190
Oke, J. B. 1974, ApJS, 27, 21
Osterbrock, D. E. 1989, The Astrophysics of Gaseous Nebulae and Active Galactic Nuclei (Mill Valley: Univ. Sci. Books)
Petit, H., Sivan, J. P., & Karachentsev, I. D. 1988, A&AS, 74, 475
Press, W. H., Flannery, B. P., Teukolsky, S. A., & Vetterling, W. T. 1989, Numerical Recipes (Cambridge: Cambridge Univ. Press)
Raymond, J. C. 1979, ApJS, 39, 1
Rubin, V. C., Kumar, C. K., & Ford, W. K. 1972, ApJ, 177, 31
Russell, S. C., & Dopita, M. A. 1990, ApJS, 64, 93
Sabbadin, F., & Bianchini, A. 1979, PASP, 91, 62
Schlegel, E. M. 1994a, ApJ, 424, L99
———. 1994b, ApJ, 434, 523
Shaver, P. A., McGee, R. X., Newton, L. M., Danks, A. C., & Pottasch, S. R. 1983, MNRAS, 204, 53
Skillman, E. D. 1985, ApJ, 290, 449
Smith, H. E. 1975, ApJ, 199, 591
Smith, R. C. 1991, Ph.D. thesis, Harvard Univ.
Smith, R. C., Chu, Y.-H., MacLow, M.-M., Oey, M. S., & Klein, U. 1994, AJ, 108, 1266
Smith, R. C., Kirshner, R. P., Blair, W. P., Long, K. S., & Winkler, P. F. 1993, ApJ, 407, 564
Stone, R. P. S. 1977, ApJ, 218, 767
Tenorio-Tagle, G., & Bodenheimer, P. 1988, AR&A, 26, 145
Tully, R. B. 1988, Nearby Galaxies Catalog (Cambridge: Cambridge Univ. Press)
van den Bergh, S. 1988, PASP, 100, 1486
———. 1997, AJ, 113, 197
Van Dyk, S. D. 1992, AJ, 103, 1788
Van Dyk, S. D., Sramek, R. A., Weiler, K. W., Hyman, S. D., & Virden, R. E. 1994, ApJ, 425, L77
Walterbos, R. A. M., & Braun, R. 1992, A&AS, 92, 625
———. 1994, ApJ, 431, 156
Westerlund, B. E., & Mathewson, D. S. 1966, MNRAS, 131, 371
Williams, R. M., & Chu, Y.-H. 1995, ApJ, 439, 132
Yang, H., Skillman, E. D., & Sramek, R. A. 1994, AJ, 107, 651
Zaritsky, D., Kennicutt, R. C., & Huchra, J. P. 1994, ApJ, 420, 87

```
Title SNR21 in M101
c luminosity 39.2
hden 1.821606
radius 15 linear parsecs
blackbody temp = 184442
filling factor = .1
ionization parameter = -2.843287
c
abundances he=-20.0 li=-10.268 be=-20.00 b=-10.051
continue c=-3.5229 n=-4.515 o=-3.586 f=-20.00 ne=-4.6200
continue na=-6.5229 mg=-5.5229 al=-6.699 si=-5.3979 p=-6.7959
continue s=-5.09 cl=-7.00 ar=-6.130 k=-7.9586 ca=-7.699
continue sc=-20.00 ti=-9.2366 v=-10.00 cr=-8.00 mn=-7.00
continue fe=-5.0229 co=-6.00 ni=-7.00 cu=-8.8239 zn=-7.699
c
c
c optimize lines
c O  3 5007 intensity=532 error=1.0
c O  3 4959 intensity=185 error=1.0
c O  1 6300 intensity=76 error=1.0
c S II 6731 intensity=107 error=0.5
c S II 6716 intensity=163 error=0.5
c N  2 6584 intensity=186 error=0.5
c N  2 6548 intensity=57 error=0.5
c end of lines
c TOTL 3727 intensity=218 error=2.0
c TOTL 4363 intensity=2.3 error=0.5
c S  3 9069 intensity=25.0 error=1.0
c S  3 9532 intensity=65.0 error=1.0
c Ar 3 7135 intensity=9.2 error=1.0
c Ne 3 3869 intensity=24.6 error=2.0
c
print faint 0.01
normalize 4861 factor=100
constant density
sphere
stop temp=100k
stop column density 23
iterations=2
print last
```

Element	Ion	Wavelength	Flux	Intensity
O	II	3729	-2.243	415.8607
O	II	3726	-2.387	298.7157
O	3	4959	-2.595	185.0623
O	3	5007	-2.134	534.2747
S	II	6716	-2.667	156.6774
S	II	6731	-2.809	112.9257
S	3	9069	-3.032	67.6167
S	3	9532	-2.637	167.6894
N	3	1750	-4.109	5.6646
N	2	6548	-3.078	60.8329
N	2	6584	-2.608	179.5177
Ne	3	3869	-3.085	59.7912
Ne	3	3968	-3.606	18.0202
Ar	3	7135	-3.787	11.8943
Ar	4	4740	-5.371	0.3094
C	2	4267	-5.555	0.2029
O	1	6300	-2.983	75.5865

```
Title SNR24 in M101
c luminosity 39.2
hden 2.941606
radius 15 linear parsecs
  ackbody temp = 304442
filling factor = .1
ionization parameter = -2.923287
c
abundances he=-20.0 li=-10.268 be=-20.00 b=-10.051
continue c=-3.5229 n=-4.451 o=-3.685 f=-20.00 ne=-4.6200
continue na=-6.5229 mg=-5.5229 al=-6.699 si=-5.3979 p=-6.7959
continue s=-4.828 cl=-7.00 ar=-6.130 k=-7.9586 ca=-7.699
continue sc=-20.00 ti=-9.2366 v=-10.00 cr=-8.00 mn=-7.00
continue fe=-5.0229 co=-6.00 ni=-7.00 cu=-8.8239 zn=-7.699
c
c
c optimize lines
c O  3 5007 intensity=276 error=2.0
c O  3 4959 intensity=103 error=2.0
c O  1 6300 intensity=100 error=2.0
c S II 6731 intensity=151 error=1.0
c S II 6716 intensity=167 error=1.0
c N  2 6584 intensity=208 error=1.0
c N  2 6548 intensity=99 error=1.0
c end of lines
c TOTL 3727 intensity=218 error=2.0
c TOTL 4363 intensity=2.3 error=0.5
c S  3 9069 intensity=25.0 error=1.0
c S  3 9532 intensity=65.0 error=1.0
  Ar 3 7135 intensity=9.2 error=1.0
c Ne 3 3869 intensity=24.6 error=2.0
c
print faint 0.01
normalize 4861 factor=100
constant density
sphere
stop temp=100k
stop column density 23
iterations=2
print last
```

Element	Ion	Wavelength	Flux	Intensity
O	II	3729	-1.294	283.4593
O	II	3726	-1.236	323.7414
O	3	4959	-1.750	99.0585
O	3	5007	-1.290	285.9818
S	II	6716	-1.523	167.1544
S	II	6731	-1.566	151.4764
S	3	9069	-1.482	183.8818
S	3	9532	-1.087	456.0270
N	3	1750	-3.011	5.4325
N	2	6548	-1.773	93.9709
N	2	6584	-1.303	277.3082
Ne	3	3869	-1.928	65.7783
Ne	3	3968	-2.449	19.8247
Ar	3	7135	-2.615	13.5404
Ar	4	4740	-4.407	0.2184
C	2	4267	-4.455	0.1957
C	3	1549	-5.542	0.0160
O	1	6300	-1.747	99.8095

```
Title SNR33 in M101
c luminosity 39.2
hden 1.821606
radius 15 linear parsecs
 ackbody temp = 284442
filling factor = .1
ionization parameter = -2.143287
c
abundances he=-20.0 li=-10.268 be=-20.00 b=-10.051
continue c=-3.5229 n=-4.448 o=-3.866 f=-20.00 ne=-4.6200
continue na=-6.5229 mg=-5.5229 al=-6.699 si=-5.3979 p=-6.7959
continue s=-4.967 cl=-7.00 ar=-6.130 k=-7.9586 ca=-7.699
continue sc=-20.00 ti=-9.2366 v=-10.00 cr=-8.00 mn=-7.00
continue fe=-5.0229 co=-6.00 ni=-7.00 cu=-8.8239 zn=-7.699
c
c
c optimize lines
c O  3 5007 intensity=194 error=1.0
c O  3 4959 intensity=69 error=1.0
c S II 6731 intensity=89 error=1.0
c S II 6716 intensity=124 error=1.0
c N  2 6584 intensity=215 error=1.0
c N  2 6548 intensity=72 error=1.0
c end of lines
c TOTL 3727 intensity=218 error=2.0
c TOTL 4363 intensity=2.3 error=0.5
c S  3 9069 intensity=25.0 error=1.0
c S  3 9532 intensity=65.0 error=1.0
c Ar 3 7135 intensity=9.2 error=1.0
  Ne 3 3869 intensity=24.6 error=2.0

print faint 0.01
normalize 4861 factor=100
constant density
sphere
stop temp=100k
stop column density 23
iterations=2
print last
```

Element	Ion	Wavelength	Flux	Intensity
O	II	3729	-1.797	199.6046
O	II	3726	-1.944	142.4363
O	3	4959	-2.265	68.0716
O	3	5007	-1.804	196.5228
S	II	6716	-2.003	124.3381
S	II	6731	-2.148	89.0951
S	3	9069	-2.058	109.5418
S	3	9532	-1.664	271.6634
N	3	1750	-3.118	9.5415
N	2	6548	-2.235	72.8332
N	2	6584	-1.765	214.9307
Ne	3	3869	-2.349	56.0444
Ne	3	3968	-2.870	16.8910
Ar	3	7135	-3.038	11.4759
Ar	4	4740	-4.202	0.7856
C	2	4267	-4.874	0.1673

```
Title SNR76 in M101
c luminosity 39.2
hden 1.021606
radius 15 linear parsecs
  ackbody temp = 204440
rilling factor = .1
ionization parameter = -3.15287
c
abundances he=-10.0 li=-10.268 be=-20.00 b=-10.051
continue c=-3.5229 n=-5.015 o=-4.035 f=-20.00 ne=-4.6200
continue na=-6.5229 mg=-5.5229 al=-6.699 si=-5.3979 p=-6.7959
continue s=-5.55 cl=-7.00 ar=-6.130 k=-7.9586 ca=-7.699
continue sc=-20.00 ti=-9.2366 v=-10.00 cr=-8.00 mn=-7.00
continue fe=-5.0229 co=-6.00 ni=-7.00 cu=-8.8239 zn=-7.699
c
c
c optimize lines
c O  3 5007 intensity=75 error=1.0
c O  3 4959 intensity=32 error=1.0
c O  1 6300 intensity=52 error=1.0
c S II 6731 intensity=72 error=1.0
c S II 6716 intensity=113 error=1.0
c N  2 6584 intensity=78 error=1.0
c N  2 6548 intensity=26 error=1.0
c end of lines
c TOTL 3727 intensity=218 error=2.0
c TOTL 4363 intensity=2.3 error=0.5
c S  3 9069 intensity=25.0 error=1.0
c S  3 9532 intensity=65.0 error=1.0
  Ar 3 7135 intensity=9.2 error=1.0
  Ne 3 3869 intensity=24.6 error=2.0
c
print faint 0.01
normalize 4861 factor=100
constant density
sphere
stop temp=100k
stop column density 23
iterations=2
print last
```

Element	Ion	Wavelength	Flux	Intensity
O	II	3729	-3.673	184.9999
O	II	3726	-3.842	125.3413
O	3	4959	-4.454	30.6479
O	3	5007	-3.994	88.4804
S	II	6716	-3.926	103.2704
S	II	6731	-4.081	72.3060
S	3	9069	-4.647	19.6656
S	3	9532	-4.252	48.7706
N	3	1750	-6.004	0.8636
N	2	6548	-4.520	26.3549
N	2	6584	-4.050	77.7733
Ne	3	3869	-4.144	62.5693
Ne	3	3968	-4.665	18.8575
Ar	3	7135	-4.907	10.8090
Ar	4	4740	-7.150	0.0618
C	2	4267	-6.709	0.1704
Fe	3	4658	-5.121	6.6010
O	1	6300	-4.220	52.4724

No. 937 811E
Engineer's Computation Pad
STAEDTLER®

OI

30pc

15pc = R

~~I He~~
~~I He+~~

[He I]
[He II]
[O II]
[O III]
[N II]
[S II]

T 15,000

Mg
Fe
Ni
Co

Supernova

He −1.1300
O −4.2254
N −5.0310
S −5.9725

Really important

un: bruce
pw: cloudy 2

"ls" to start new session - brings up list of files

c - inactive command
pwd -> where are we?
cd MARK
to actually run cloudy "runcloudy &"

beeps signifies completion

oxygen - typically dependent on temp

S - influenced by density & temp...

save ~~[illegible]~~ twice

play with abundances first
then temp (black body) set then grid (profile)
scroll on down and can adjust intensities

Supernova stuff in hazy?

enzo?

photoionization code?

optimization technique?

radial dependence of dens?

ejected gas mass?

plasma simulation code?

"gas" in index?

Fil [illegible]

Temp opt - 294442K

opt Ion param - -2.212

O ratios sul [redacted] abun lo

N ratio -> too high for 6583 abun too high

S ratio -> too high for 6716 abund 6716 high 6731 slightly lo

upped O by .2 : 0630 : 8634

other O's slightly high

N ratio -> [redacted] bad [redacted]

S - same as before

drop O by .2!

[illegible]

[illegible] high [illegible] 6716 [illegible]

[illegible] 6731 39% low

[illegible]

N 6548 / N 6584 change [illegible]

[illegible] -3.7 [illegible]

[illegible] improved

March 2005

$$10^x + Y = 10^{x+c}$$

Y = how much up or down (add or subtract)
X = intensity (on screen)
c = amount changed [illegible] (abundances)

	SNR 21	Cloudy	SNR 76	CLOUDY
04959	185	184.98	32	29
05007	532	534.04	75	83
06300	76	75.66	52	52
N6548	57	59.29	26	26
N6583	186	174.95	78	78
S6716	163	162.[illegible]	113	102
S6731	107	116.87	72	73

.3.89

April 200[illegible]

Necessary Graciousness

- Dr. Joe-The expert on BIRTH…
- Dr. Welsh-UNIX code
- Hubble Space Telescope for all the pretty pictures
- Dr. Ferland-CLOUDY is great!
- Students and Staff of Physics and Honors Departments for their support